

3D Printing of Concrete: Some Practical Challenges and Recommendations

By

Guanzhong Xu

A Thesis

*Submitted in Fulfilment of the Requirement of the Degree of Master
of Engineering Science (Research)*



Department of Civil Engineering,

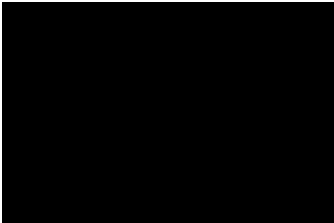
Monash University,

Melbourne, Australia

September, 2018

Under the Copyright Act 1968, this thesis must be used only under the normal conditions of scholarly fair dealing. In particular no results or conclusions should be extracted from it, nor should it be copied or closely paraphrased in whole or in part without the written consent of the author. Proper written acknowledgement should be made for any assistance obtained from this thesis.

I certify that I have made all reasonable efforts to secure copyright permissions for third-party content included in this thesis and have not knowingly added copyright content to my work without the owner's permission.



Guanzhong Xu

September 2018

Abstract

Due to certain problems the modern concrete construction industry is faced with, 3D printing technology has become one of the feasible alternatives, providing high automation, cost-effectiveness, time-efficiency, low labour-intensiveness, and environmental friendliness. However, there are several practical issues and challenges for applying the technology to concrete construction.

The study reported in this research master's thesis aims to modify the current 3D printing technology in concrete by specifying the issues and challenges and finding likely approaches. Aspects of the 3D printing process as well as durability are investigated. First, since most existing 3D printing methods for concrete are based on the material extrusion process and layer by layer application, the interlayer bond between the layers is weak. Hence, investigation of ways to improve such bonding strength is undertaken. Secondly, when a new type of material has been introduced into 3D printed layered mortar, differential movement between the materials become a serious problem, in the long term leading to cracks development. The associated dimensional changes can be caused by many factors. Alkali-silica reaction (ASR) is a factor of concern, arising due to the high presence of ASR reactive aggregates in 3D printed mortar. Thirdly, strain measurement between 3D printed mortar layers is currently difficult. Traditional strain gauges are made of three-dimensional materials, which have their own drawbacks and are difficult to apply to 3D printed mortar. However, two-dimensional materials, transition metal dichalcogenides (TMDs) such as MoS_2 and WS_2 , have the potential for sensing such parameters due to their superior mechanical and optoelectronic properties. In this study, MoS_2 and WS_2 are fabricated, transferred, and investigated for their mechanical properties.

This thesis reports on three main tasks: (1) to specify the key bottleneck in current applications of 3D printing technology on concrete construction and to find alternatives for it; (2) to investigate ASR arising due to the high presence of reactive aggregate in 3D printed mortar and to try to reduce it; and (3) to investigate the use of TMDs for sensing purposes in order to measure the dimensional change between 3D printed layers.

Bonding agents like polymer adhesives, such as epoxy, is shown to be an effective option. From the results, over 80% strength increases at 28 days are observed in comparison to control specimens. Moreover, in the next stage, polyvinyl alcohol (PVA) fibres are incorporated into the previous system and it proves to be effective, obtaining further enhancements (an additional 21% increase) of the interlayer bonding strength. Meanwhile, by controlling process parameters, an optimised approach to improving bonding is proposed. Apart from the experimental program, molecular dynamics (MD) simulations are also utilised to assess chemical bonding between epoxy adhesive and calcium silica hydrates (CSH). Another polymer type, carbon-sulphur (BCS) is investigated using the same method, and is shown also to be effective in improve 3D printed mortar interlayer bonding. Moreover, in this study, the effectiveness of graphene oxide (GO) in reducing ASR is investigated and is shown to assist the control of expansion. Furthermore for sensing purposes, the chemical vapour deposition (CVD) method is found to be effective for fabricating high-quality ultra-smooth surface MoS_2 and WS_2 . The wet-chemical transfer method can be applied to transfer MoS_2 and WS_2 flakes from fabrication substrates to other substrates. Strain relaxation is determined by mechanical testing.

Abbreviations

2D	Two-dimensional
3D	Three-dimensional
3DP	3D printing
3DCP	3D concrete printing
Å	Angstrom
AAR	Alkali-aggregate reaction
AFM	Atomic force microscopy
Al ₂ O ₃	Aluminium oxide
AM	Additive manufacturing
ASR	Alkali-silica reaction
Ca	Calcium
Cu	Copper
CASTEP	Cambridge serial total energy package
CC	Contour crafting
CSH	Calcium silica hydrates
COMPASS	Condensed-phase optimized molecular potentials for atomistic simulation studies
CVD	Chemical vapour deposition
°C	Degrees Centigrade
DEF	Delayed ettringite formation

DFT	Density functional theory
DI water	Distilled water
EBM	Electron beam melting
ECC-PVA	Engineered cementitious composites with polyvinyl alcohol fibres
eV	Electron volt
FDM	Fused deposition modelling
FE	Finite element
GO	Graphene oxide
GP	General purpose
GPa	Gigapascal
h	Hour
K	Kelvin
kN	Kilonewton
KOH	Potassium hydroxide
I	Second moment of area about the neutral axis
ITZ	Interfacial transition zone
L_n	Length measurement at n days
L_o	Initial length
LENS	Laminated engineered net shaping
LOM	Laminated object manufacturing
mm	Millimetre

mm/min	Millimetres per minute
min	Minute
M	Moment about the neutral axis
MD	Molecular dynamics
MeV	Mega electron volt
MIT	Massachusetts Institute of Technology
Mo	Molybdenum
MoO ₃	Molybdenum trioxide
MoS ₂	Molybdenum disulphide
MPa	Megapascal
nm	Nanometer
N ₂	Nitrogen
N/m	Newtons per metre
NaOH	Sodium hydroxide
O	Oxygen
O ₂ -Si-O ₂	Silica tetrahedral
OH ⁻	Hydroxyl
PDMS	Polydimethylsiloxane
PL	Photoluminescence
PMMA	Polymethyl methacrylate
Ps	Picosecond

PVA	Polyvinyl alcohol
r/min	Rad per minute
RDF	Radial distribution function
sccm	Standard cubic centimetres per minute
Se	Selenium
Si	Silica
SiO ₂	Silica dioxide
Si-O-Si	Siloxane bond
Si-OH	Silanol group
S	Sulphur
SEM	Scanning electron microscopy
SL	Stereolithography
SLS	Selective laser sintering
T	Temperature
TMDs	Transition metal dichalcogenides
V	Volt
W	Tungsten
WO ₃	Tungsten trioxide
WS ₂	Tungsten disulphide
WSe ₂	Tungsten diselenide
X-	Trion

X0	Exciton
y	Perpendicular distance to the neutral axis
σ	Bending stress
μm	Micrometer

Declaration

This thesis describes my research carried out in the Department of Civil Engineering at Monash University in Australia during the candidature period from March 2016 to September 2018. The thesis is submitted to Monash University in total fulfilment of the requirements for the degree of Master of Engineering Science (Research).

As this is a thesis with publications, several publications are referred to in this thesis. I have received the approval of all the authors to include corresponding contribution in this thesis.

For published papers:

1. Xu, G., Chen, S. J., Korayem, A. H., Duan, W. H., Sanjayan, J. G., & Wang, C. M. (2016). *3D printing technology of concrete – an emerging construction method for industry. Concrete in Australia*, 43, 32-41.
2. Zhang, Q., Chang, Z., Xu, G., Wang, Z., Zhang, Y., Xu, Z. Q., et al.. (2016). *Strain relaxation of monolayer WS₂ on plastic substrate. Advanced Functional Materials*, 26(47), 8707-8714.

In Chapter 5, introduction, the experimental program and results are partially referenced from this publication. The author contributed to the experimental sessions, especially significantly to the CVD fabrication and wet-chemical transfer.

For other unpublished materials:

3. *Submitted journal paper (Composite Part B): Carbon-sulphur polymer enhancing the interlayer cohesion of 3D printing concrete.*

In Chapter 3, MD simulation results are referenced. The author contributed to the background writing and some experimental sessions in that paper.

4. *Submitted conference paper (1st International Conference on 3D Construction Printing): Effect of epoxy adhesive on interaction and effective strength of the interlayer zone in 3D printing concrete: Computational Approach.*

In Chapter 3, MD simulation results are referenced. The author contributed all the experimental work to that paper for comparison purposes.

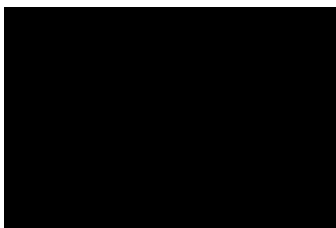
5. *Zhou, C. Thesis for bachelor's degree: The study of the effectiveness of graphene oxide (GO) to reduce alkali-silica reaction (ASR) and to enhance mechanical properties of concrete.*

In Chapter 4, the experimental program and results are referenced. The author contributed significantly to the experimental work.

6. *Zhang, Q. PhD thesis: Emerging Two-Dimensional Transition Metal Dichalcogenides for Novel Strain Sensing Application: Fabrication, Characterization and Implementation.*

In Chapter 2, some literature reviews with regard to TMDs are referenced. In Chapter 5, CVD and transfer experiments are referenced. The author contributed to the experimental work, especially significantly the CVD fabrication and wet-chemical transfer.

7. *Xu, G. Final year project report: Fabrication and Characterization of Optoelectronic Behavior of Monolayer MoS₂ and WS₂ under Large Tensile Strain.*



Guanzhong Xu

September 2018

Acknowledgements

First of all, I must state my appreciation to God for offering me the opportunity to complete my studies at Monash University, including both my undergraduate and research master studies. I had the amazing fortune to join the 2+2 program in 2011 at Central South University in China, which provided me with the funds for my study in Australia. I worked very hard when I was an undergraduate student, and in return I had the opportunity to continue study as a postgraduate student. During the study involved in my research, I can summarise my life into three places and one straight line: office, laboratory, bed, and the way between them. Through my research, I have acquired knowledge for which I had never previously had the opportunity. Also, my study has taught me lessons that do not appear in textbooks. I am grateful that God has kept me healthy and energetic for this research so that I can fulfil the requirements of the degree of Master of Engineering Science (Research).

My parents are next for me to thank. Without their support, I would not have had the opportunity to study overseas at Monash University, in Australia. They covered my tuition fees and living allowance during my undergraduate studies. Moreover, they give me love and care even they are far away. I also acknowledge the financial assistance from Australian Research Council and the use of facilities in the Monash Centre for Electron Microscopy (MCEM).

Further, I acknowledge the Monash Centre for Atomically Thin Materials for providing me the MCATM scholarship which has covered part of my living expenses. I also acknowledge Monash University for offering me the best study environment and the Faculty of Engineering for supporting an Engineering International Postgraduate Research Scholarship (FEIPRS) to cover my tuition fees during the postgraduate period.

Moreover, I need to express my appreciation of the kind guidance from my supervisor, Professor Wenhui Duan. He has given me this amazing study topic and offered support and

guidance all the time. Even when I was in darkness without direction, he guided me to the bright way.

Furthermore, I appreciate the assistance and guidance offered by collaborators, Dr Asghar Habibnejad Korayem, Dr Ezzatollah Shamsaei, Dr Shujian Chen, and Dr Kwesi Sagoe-Crentsil. They offered me detailed guidance and even worked together with me.

After that, I would like to take the opportunity to express my sincere gratitude to the hard-working Monash laboratory staff for their assistance and efforts in my experiments, especially to Mr Long Kim Goh, Mr Michael Leach at the Civil Engineering Laboratory, and Dr Xiya Fang and Dr Flame Burgmann at the MCEM.

Next, I express my appreciation of the assistance and collaboration from my colleagues, Dr Qianhui Zhang, Dr Zhenyue Chang, Mr Wei Wang, Miss Yuxi Zhang, Mr Yanming Liu, Mr Xupei Yao, Mr Chengke Ruan, Mr Eshan Hosseini, Mr Chen Zhou, Mr Dong Guo, and my final year project students Miss Vinshaka, Miss Shiniva, Mr Roy, and Mr Oliver. Also, I need to acknowledge the contribution from proof reading for this thesis, made by JR.

Finally, I would like to thank my girlfriend, Erin, for accompanying and caring about me when I was writing this thesis. She is the closest person to me every day, sharing happiness and sorrow with me, and supporting me unconditionally. I love you.

List of publications

Published:

1. Xu, G., Chen, S. J., Korayem, A. H., Duan, W. H., Sanjayan, J. G., & Wang, C. M. (2016). *3D printing technology of concrete – an emerging construction method for industry. Concrete in Australia*, 43, 32-41.
2. Zhang, Q., Chang, Z., Xu, G., Wang, Z., Zhang, Y., Xu, Z. Q, et al.. (2016). *Strain relaxation of monolayer WS₂ on plastic substrate. Advanced Functional Materials*, 26(47), 8707-8714.

Submitted:

3. Hosseini, E., Zakertabrizi, M, Korayem, A. H, Xu, G. *Carbon-Sulphur polymer enhancing the interlayer cohesion of 3D printing concrete. Composite B*.
4. Hosseini, E., Korayem, A. H, Xu, G. *Effect of epoxy adhesive on interaction and effective strength of the interlayer zone in 3D printing concrete: Computational Approach. 1st International Conference on 3D Construction Printing*.

Table of Contents

Abstract.....	II
Abbreviations.....	IV
Declaration.....	IX
Acknowledgements.....	XII
List of publications	XIV
List of figures.....	XIX
List of tables.....	XXIII
Chapter 1. Introduction.....	1
1.1 Background	1
1.2 Research objectives.....	5
1.3 Thesis structure	6
Chapter 2. Literature review	9
2.1 3D printing technology and its potential for construction.....	9
2.2 Existing 3D printing technology in concrete construction.....	12
2.2.1 D-shape	13
2.2.2 Contour crafting	15
2.2.3 3DCP technique	16
2.2.4 Composite method	17
2.2.5 Print-in-place construction.....	18
2.3 Challenges of existing methods.....	19

2.3.1	Mechanical properties	19
2.3.2	Reinforcements	20
2.3.3	Curing	21
2.3.4	Hardening time, pumpability and extrudability	21
2.3.5	Durability	22
2.3.6	Applicability	23
2.3.7	Interlayer bonding	23
2.4	Techniques for improving performance of 3D printing layered concrete.....	25
2.4.1	Epoxy	25
2.4.2	Polyvinyl alcohol (PVA) fibre	25
2.4.3	Graphene oxide (GO).....	26
2.4.4	Transition metal dichalcogenides (TMDs) (MoS ₂ and WS ₂)	26
Chapter 3.	Investigation of interlayer bonding between 3D printed mortar layers using epoxy adhesive	32
3.1	Introduction	32
3.2	Experimental program.....	34
3.2.1	Materials	34
3.2.2	Experimental methods	35
3.2.3	SEM characterisation	38
3.3	Molecular dynamics simulation	38
3.4	Results and discussion.....	40

3.4.1	Effectiveness of epoxy adhesive to improve mortar interlayer bonding	40
3.4.2	Enhancement of mortar-epoxy system by PVA fibres	47
3.4.3	The influence of oven curing temperature on epoxy-mortar and epoxy-fibre-mortar system	49
3.4.4	The influence of printing interval time on epoxy-mortar and epoxy-fibre-mortar system	53
3.5	Conclusions	57
Chapter 4. Study of the effectiveness of GO in reducing alkali-silica reaction (ASR) in 3D printed mortar.....		59
4.1	Introduction	59
4.2	Experimental program.....	60
4.2.1	Expansion testing of ASR mortar	60
4.2.2	Mechanical testing of ASR mortar	62
4.2.3	SEM characterisation	62
4.3	Results and discussion.....	63
4.3.1	Expansion test	63
4.3.2	Mechanical test	66
4.3.3	SEM characterisation	67
4.4	Conclusions	68
Chapter 5. Research on MoS ₂ and WS ₂ : potential sensing material for 3D printing technology in concrete construction		70
5.1	Introduction	70

5.2	Experimental program.....	71
5.2.1	CVD technique for fabrication of monolayer MoS ₂ and WS ₂	72
5.2.2	Wet-chemical transfer technique	73
5.2.3	Optical and AFM measurements	74
5.2.4	FE simulation.....	74
5.3	Results and discussion.....	75
5.3.1	Chemical vapour deposition (CVD) fabrication	75
5.3.2	Wet-chemical transfer technique	77
5.3.3	Strain relaxation of WS ₂ on PDMS substrate by Raman and PL and FE simulation	80
5.4	Conclusions	81
Chapter 6.	Conclusions and recommendations.....	83
6.1	Key research findings.....	83
6.2	Recommended approaches and parameters.....	85
References	89

List of figures

Figure 2-1 Schematics of seven categories of AM in ASTM (Loughborough University 2016): (a) Binder jetting; (b) Directed energy deposition; (c).Material extrusion; (d) Material jetting; (e) Powder bed fusion; (f) Sheet lamination; (g) Vat photopolymerisation.	10
Figure 2-2 Five novel 3D printing-based construction methods (Xu, Chen et al. 2016).....	13
Figure 2-3 Schematic of D-Shape printing process: (a) before printing, (b) during printing, and (c) after printing (Feng, Meng et al. 2015).	14
Figure 2-4 The 'Bloom' pavilion (Williams 2015) printed by D-Shape method.	15
Figure 2-5 Schematic of contour crafting method (Khoshnevis 2004).....	15
Figure 2-6 The highest building worldwide by 3D printing (Havencab 2016).	16
Figure 2-7 Concrete printing process (Alec 2014).	17
Figure 2-8 The composite method (Jimenez Garcia 2016).....	17
Figure 2-9 Additive fabrication tests using polyurethane spray foam (left) produced test isolative formwork samples with consistent and tunable layer heights (right) (Keating 2014).	18
Figure 2-10 Combining additive and subtractive processes in the Print-in-Place construction method.....	19
Figure 2-11 Layered crystal structure of MoS ₂ and WS ₂ (Radisavljevic, Radenovic et al. 2011)	27
Figure 2-12 a) Typical CVD principle for fabricating thin MoS ₂ samples; b) and c) Optical image of MoS ₂ flakes grown by van der Zande et al. (2013).....	29
Figure 2-13 Schematic of PMMA-assisted transfer process (Lu, Lu et al. 2014).	30

Figure 3-1 Schematic of the specimens: a) the procedure to cast cubic specimens; b) the final specimen used for strength test by cutting.....	36
Figure 3-2 load path for 3-point bending test	37
Figure 3-3. Fracture surface by three-point bending test for SEM scanning.....	38
Figure 3-4 Three-point bending test results showing effectiveness of epoxy in improving interlayer bonding	42
Figure 3-5 SEM for group E40-30: a) on epoxy side with CSH and interlocking phenomenon; b) on mortar side without epoxy features; c) on epoxy side with CSH and interlocking; and d) on mortar side with a few epoxy features	44
Figure 3-6 (a) Model of the CSH-epoxy resin composite; (b) direction of imposed strain on the model; (c) Stress-strain diagram of pristine CSH and CSH-epoxy resin composite	45
Figure 3-7 a) Stress-strain behaviour of printed mortar, BCS polymer enhanced printed mortar; b) Modelled interaction zone under tensile strain c) Interfacial shear strength for pristine printed mortar, BCS-enhanced printed mortar and seamless mortar specimen d) Modelled interaction zone under shear force	46
Figure 3-8 Three-point bending test results showing the effectiveness of PVA fibres in improving the previous approach.....	48
Figure 3-9 SEM for group F40-30: a) hole left by fibre pull-out; b) fibre broken in mortar; c) pull-out phenomenon; and d) fibre pull-out and broken.	49
Figure 3-10 7 days three-point bending test results to determine the influence of oven curing temperature	51
Figure 3-11 14 days three-point bending test results to determine the influence of oven curing temperature	51

Figure 3-12 28 days three-point bending test results to determine the influence of oven curing temperature	52
Figure 3-13 7 days three-point bending test results to determine the influence of printing interval time.	55
Figure 3-14 14 days three-point bending test results to determine the influence of printing interval time.	55
Figure 3-15 28 days three-point bending test results to determine the influence of printing interval time	56
Figure 4-1 Mortar bar test results of expansion rates for three groups.	65
Figure 4-2 Flexural test results.	67
Figure 4-3 SEM showing cracks and GO-like features.	68
Figure 5-1 Schematic representation of the experimental instrument and reactants: a) MoS ₂ and b) WS ₂ (Zhang, Chang et al. 2016).	72
Figure 5-2 Eight steps for wet-chemical transfer technique.	74
Figure 5-3 (a) Optical image of a WS ₂ crystal grown on sapphire. (b) AFM height image of the WS ₂ crystal on sapphire. (c) Height image of the square region shown in (b). (d-f) Integrated Raman intensity, integrated PL intensity and PL peak position mapping of the WS ₂ crystal on sapphire. (g) PL spectrum of WS ₂ on sapphire. Black circles are experimental data; blue line is a fit to the sum of two Lorentzians (red and green lines). (h) Raman spectrum of WS ₂ on sapphire. Scale bar: 5 μ m in (a,b) and (d-f); 2 μ m in (c) (Zhang, Chang et al. 2016).	76
Figure 5-4 Schematic illustration of WS ₂ crystals transferred by a PMMA-assisted wet-chemical method on PDMS substrate (Zhang, Chang et al. 2016).	78

Figure 5-5 a) Optical image of a WS₂ crystal transferred on PDMS substrate. b) AFM height image of the WS₂ crystal on PDMS. c) Height image of the square region shown in (b). d–f) Integrated Raman intensity, integrated PL intensity and PL peak position mapping of the WS₂ crystal on PDMS. g) PL spectrum of WS₂ on PDMS without strain. Black circles are experimental data; blue line is a fit to the sum of two Lorentzians (red and green lines). h) Raman spectrum of WS₂ on PDMS without strain. i) Schematic of tensile stress loading frame. Scale bar: 5 μm in (a) and (b) and (d)–(f); 1 μm in (c) (Zhang, Chang et al. 2016).79

Figure 5-6 Finite element (FE) simulation of WS₂ under tensile strain. a,b) FE model of WS₂/PDMS sample under tensile strain corresponding to the case in Figure 4a. c,d) Snapshots of FE simulation results of WS₂ under the substrate strain at 0.1 and 0.5. e,f) FE model of WS₂/PDMS sample under tensile strain corresponding to the case in Figure 4b,c. g,h) Snapshots of FE simulation results of WS₂ under substrate strain at 0.1 and 0.5 (Zhang, Chang et al. 2016)..81

List of tables

Table 2-1 AM categories details (ASTM 2015, Huang, Leu et al. 2015).....	11
Table 2-2 Elastic properties of monolayer MoS ₂	28
Table 3-1 Mix design for mortar-epoxy system (weight: grams)	35
Table 3-2 Experimental schedule.....	37
Table 3-3 Details of specimens' parameters for investigating the effectiveness of epoxy to improve interlayer bonding.....	41
Table 3-4 Parameters of specimens used to investigate the effectiveness of PVA fibre to improve interlayer bonding.....	47
Table 3-5 Details of specimens' parameters for investigating the influence of epoxy curing temperature on interlayer bonding in mortar-epoxy and mortar-epoxy-PVA systems.....	50
Table 3-6 Details of specimens' parameters for investigating the influence of printing interval time on interlayer bonding of mortar-epoxy and mortar-epoxy-PVA systems	54
Table 4-1 Mix design of expansion test of ASR mortar	61
Table 6-1 Parameters of the approach using epoxy adhesive to enhance interlayer bonding of 3D printed mortar.....	86
Table 6-2 Parameters of the approach using epoxy and PVA fibres to enhance interlayer bonding of 3D printed mortar	86

Chapter 1. Introduction

1.1 Background

The modern construction industry faces several problems. One of them is the high cost. According to Australia's Budget 2014-2015 (Australian Government 2015), by 2019-2020, the Infrastructure Growth Package will cost the Government's infrastructure investment \$50 billion. Generally, 35-60% of the overall costs of concrete structures are taken up by formwork (Hurd 2005, Robert 2007), which is not cost-effective.

Another problem of the construction industry is the long lead time which is difficult to control. Lead time is a measure of the amount of time that elapses from initiating a process to completing that process (Designing Buildings Wiki 2016). The construction process involves many steps from material fabrication to transportation and to in-situ formwork construction, and each step is time-consuming. Lead time can also be influenced by other factors. For instance, according to a government Green Paper (Australian Government 2014), the inadequate progressing of construction under adverse weather conditions is one of the main factors that significantly influence lead time.

The conventional construction industry is also labour-intensive (Pathirage et al. 2007) and unsafe. According to the statistics from the United States Bureau of Labor, 1 out of 20 full-time American workers were injured or suffered from a work-related illness in 2010, with 802 fatalities reported. This death figure ranked the highest in any sector, making construction one of the most dangerous industries (Keating 2014). Construction practices need to be improved to meet the more and more stringent work safety requirements in Australia as well (Safe Work Australia 2016).

Last but not least, current construction methods are not environmentally friendly. They consist of off-site manufacturing, transportation of materials, installation and assembly, and on-site construction. The entire process consumes considerable energy and emits huge quantities of greenhouse gases (Yan, Shen et al. 2010). After construction, formwork and other waste materials are not easily reused (Lu and Yuan 2010).

In sum, the current construction industry needs to overcome the aforementioned problems. The industry has the task of reducing costs and lead time, to solve the problem of labour-intensiveness, to provide a safer working environment and to reduce the damage to the natural environment. The problems provide the impetus for the construction industry to develop solutions to these problems.

One existing work-around is prefabrication, which has brought standardisation and mechanisation to the traditional construction industry, with many advantages. Prefabrication solves some of the aforementioned problems. It is more cost-effective, consumes less labour, shortens construction time, and is becoming independent of the influence of weather conditions (Wong, Hao et al. 2003). Also, it has been shown to be more environmentally friendly than conventional construction methods and to have lower carbon emission (Wong and Tang 2012, Lehmann 2013, Mao, Shen et al. 2013) and less waste disposal (Tam, Tam et al. 2005, Jaillon, Poon et al. 2009, Begum, Satari et al. 2010). However, prefabrication has not changed the inherent construction principles of moulding and casting. Also, prefabrication only fits the construction of massively repeated products. When it comes to fabricating components in a limited quantity, prefabrication loses many of its advantages. Therefore, structures for prefabrication favour the use of identical structural components and limit the use of optimal structural and architectural designs. Better solutions are waiting to be introduced to provide more versatile construction capabilities. The emerging additive manufacturing (AM) or so-

called “3D printing” technology is therefore a promising candidate to revolutionise concrete construction.

Often synonymous with “3D printing”, AM is cost-effective and time-efficient for producing 3D objects with complex and customised geometries, advanced material properties and functionality (Huang, Leu et al. 2015). In 2015, the ASTM International Committee F42 on AM technologies defined AM as “a process of joining materials to make objects from 3D model data, usually layer upon layer, as opposed to subtractive manufacturing methodologies” (ASTM 2015, Huang, Leu et al. 2015). In 3D printing, a digital 3D model is divided into 2D sections, and layers of exclusively designed material are used to build the structure from the aforementioned slices, i.e. layer upon layer (Ma and Wang 2017). However, some obstacles facing the 3D printing concrete method include mechanical properties, reinforcements, curing conditions, durability, interlayer bonding, the relationships among hardening time, pumpability and extrudability, and applicability (Xu, Chen et al. 2016). Among these, low shear strength in the interlayer region, where two concrete layers are attached to each other (Le, Austin et al. 2012, Sanjayan, Nematollahi et al. 2018), is now a hot topic, with researchers emphasising the need to investigate the problem. Low shear strength has contributed to the presence of free water on the concrete layer surfaces in some studies (Gillette 1963), though a certain amount of water, required for a SSD state, is deemed necessary to achieve good adhesion between layers (Austin, Robins et al. 1995). In addition, some studies have cited both lack of stability and eccentricity in freshly printed concrete as other important shortcomings (Wolfs, Bos et al. 2018). These problems limit the application of 3D printing concrete in safety contexts, e.g. providing housing for survivors in post-disaster sites.

To address this flaw in the 3D printing technology without hindering its overall advantages, a new method is presented in this thesis. In this method, a layer of adhesive is added between adjunct layers to act as a glue, binding together the layers of cementitious

material. The adhesive can be epoxy or some other polymers. Hence, the first topic in this thesis focuses the adhesive material used to enhance interlayer bonding strength between two layers of mortar.

Once a layer of adhesive is incorporated between two layers of cementitious material, dimensional change is believed to occur due to differential drying shrinkage and differential expansion of two types of different material. A factor that can exacerbate this situation is that for 3D printing, mortar with high presence of sand is used instead of traditional concrete, and the large proportion of sand, a reactive aggregate, is believed to cause the alkali-silica reaction (ASR). ASR which results in long-term durability problems is also called concrete cancer. In this thesis, ASR is investigated, and some nano-materials are introduced into mortar.

As mentioned, differential movement between 3D printed layers can be a severe problem in 3D printing concrete technology. Sensing technology is necessary to measure the relevant properties. The strain gauge is a candidate, but traditional strain gauges made of three-dimensional materials, with low strain level sustainability, limited resolution, slow responsiveness and insufficient sensitivity, are not eligible for 3D printing concrete layer measurement. Recently emerging two-dimensional materials, such as graphene and transition metal dichalcogenides (TMDs), have been investigated and found to possess superior mechanical and optical properties. Moreover, monolayer molybdenum disulphide (MoS₂) and tungsten disulphide (WS₂) have been found as direct bandgap materials with excellent optoelectronic properties. In this thesis, the fabrication of MoS₂ and WS₂ is studied. Some mechanical properties are also investigated for potential sensing purposes.

1.2 Research objectives

This research master's study focuses on some issues of the 3D printing technology of concrete. The approaches used in this thesis include experimental programs, nano-characterisations, MD simulations and FE simulations. The purpose is to investigate some problems facing current 3D printing technology of concrete, and to assist in further development of this technology. This study embraces three main topics with corresponding objectives: (1) finding and optimising an adhesive material to enhance the interlayer bonding strength between two layers of mortar; (2) understanding the mechanism of ASR and developing a potential approach to reduce it in 3D printed mortar; and (3) investigating the potential of TMDs for 3D printed concrete strain sensing for dimensional changes. The following paragraphs provide the details of each objective.

(1) Finding and optimising an adhesive material to enhance the interlayer bonding strength between two layers of mortar.

Polymer materials, such as epoxy adhesive, provide an alternative to enhance the interlayer bonding strength between two layers of 3D printed mortar. Micro-fibres such as polyvinyl alcohol (PVA) fibre, are elements that can be added into the system to enhance it further. An experimental program is carried out to measure the bonding strength, with the expectation of achieving significant improvement with the addition of epoxy. Scanning electron microscopy (SEM) characterisation is conducted in an attempt to discover the physical mechanism explaining why epoxy helps to improve strength. Furthermore, MD simulation is performed to elucidate the chemical bonding between epoxy and mortar. Besides epoxy, another material, a carbon and sulphur polymer, is investigated by MD simulation to determine whether it can achieve chemical bonding with calcium silica hydrates (CSH).

(2) Understanding the mechanism of ASR and developing a potential approach to reduce it in 3D printed mortar.

Nowadays, one of the most serious durability problems in the concrete industry is the ASR. Differential expansion caused by ASR in mortar-epoxy-mortar systems with a high content of sand, a reactive aggregate, can be a severe problem leading to reduction of interlayer bonding and long-term cracks. It is the result of the chemical reaction in the concrete from the hydroxyl ions associated with the alkalis sodium and potassium which are present within the structure of the cement and the reactive silica within the structure of the aggregates (Fernandes and Broekmans 2013). Incorporating graphene oxide (GO) can be one alternative to the problem, and in this study, it is evaluated.

(3) Investigating the potential of TMDs for 3D printed concrete strain sensing for dimensional changes.

Monolayer molybdenum disulphide (MoS_2) and tungsten disulphide (WS_2) are direct bandgap materials with excellent optoelectronic properties. In this thesis, the fabrication of MoS_2 and WS_2 is studied. Some mechanical properties are also studied for the potential sensing purpose. It is expected that a strain gauge made of 2D materials can be manufactured and introduced between 3D printed concrete layers to measure differential movement and related mechanical properties.

1.3 Thesis structure

This thesis is organised into six chapters, three of which are the main chapters with major contributions. Chapters 1, 2 and 6 present the introduction, the literature review and the conclusions and recommendations, respectively.

This Chapter, Chapter 1, introduces the background information of the thesis. It also presents the research objectives and the structure of the thesis.

Chapter 2 is organised based on a published review paper (Xu, Chen et al. 2016). This review covers the following fields:

- AM (3D printing) processes
- Existing methods for 3D printing technology of concrete
- Challenges of current 3D printing technology of concrete

The review provides a broad picture of advances in research into the 3D printing technology of concrete. It also addresses some problems faced by the technology and several potential solutions.

Chapter 3 is the significant chapter introducing approaches to solving the key bottleneck of 3D printing technology of concrete, low interlayer bonding strength. An experimental program is first carried out to test the mechanical strength of samples including control samples, samples introduced by epoxy and samples introduced by epoxy with PVA fibres. The controlled parameters are printing time interval and epoxy curing temperature. The results indicate the positive effect of epoxy and epoxy with PVA fibres. After that, SEM characterisations are conducted to find physical evidence, such as interlocking and bridging mechanisms. To find chemical evidence, such as chemical bonding between epoxy chain and calcium silica hydrates (CSH), MD simulation is conducted. Apart from the above method, another adhesive, a carbon and sulphur polymer, is studied by MD simulation to find excellent chemical bonding as well.

Chapter 4 focuses on the mechanism and an approach to reducing ASR. Given the substantial presence of sand, a reactive aggregate, ASR is expected to be severe in 3D printed mortar structures. It leads to expansion of the mortar and differential movement with the

dimensional change in the mortar-epoxy-mortar system introduced in previous chapter. An alternative is the use of GO to reduce the reaction and potential results. This chapter introduces the experimental part of this investigation and reports some results.

In Chapter 5, a novel material, TMDs, is introduced. It has the potential for producing a new generation strain gauge for the purpose of measuring differential movement and other mechanical properties of 3D printed concrete or mortar, based on its superior mechanical and optoelectronic behaviour. In this chapter, the fabrication method, chemical vapour deposition (CVD), is first studied. Then, a method to transfer fabricated material to various substrates is developed. Finally, mechanical testing is conducted by plastic substrate with WS_2 , and the strain relaxation phenomenon is found.

Chapter 5 summarises the studies presented in this thesis. For each topic, it also provides alternative recommendations. Furthermore, some future research directions are proposed.

Chapter 2. Literature review

2.1 3D printing technology and its potential for construction

Often synonymous with “3D printing”, AM is a cost-effective and time-efficient method for producing 3D objects with complex and customised geometries and advanced material properties and functionality (Huang, Leu et al. 2015). In 2015, ASTM International Committee F42 on AM technologies defined AM as “a process of joining materials to make objects from 3D model data, usually layer upon layer, as opposed to subtractive manufacturing methodologies” (ASTM 2015, Huang, Leu et al. 2015).

Based on the work of Kruth (1991), Wong and Hernandez summarised and updated the classification of AM into the following categories: (1) liquid based: fused deposition modelling (FDM), stereolithography (SL), and polyjet; (2) solid based: laminated object manufacturing (LOM); and (3) powder based: selective laser sintering (SLS), electron beam melting (EBM), laminated engineered net shaping (LENS), 3D printing (3DP), and prometal (Wong and Hernandez 2012).

ASTM International Committee F42 on AM technologies defined the terminology of AM in the standard ASTM F2792-12a and provided seven categories for grouping current and future AM machine technologies (ASTM 2015). Researchers at Loughborough University (Loughborough University 2016) supplied the schematics of each category (see Figure 2-1). In 2015, Huang, Leu et al. summarised the AM processes in ASTM and corresponding techniques and materials as shown in Table 2-1.

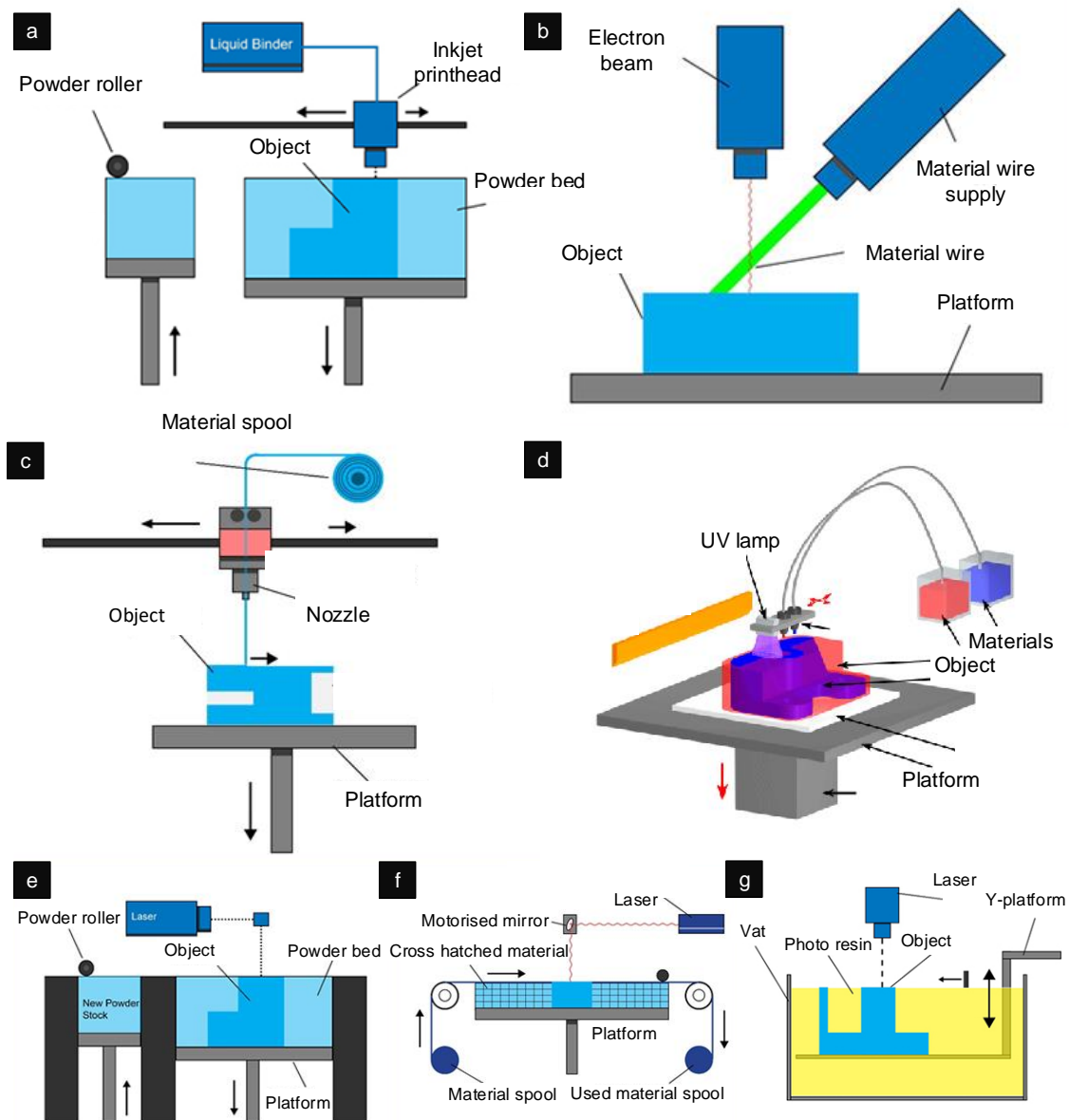


Figure 2-1 Schematics of seven categories of AM in ASTM (Loughborough University 2016): (a) Binder jetting; (b) Directed energy deposition; (c).Material extrusion; (d) Material jetting; (e) Powder bed fusion; (f) Sheet lamination; (g) Vat photopolymerisation.

Table 2-1 AM categories details (ASTM 2015, Huang, Leu et al. 2015).

Process category	Terminology	Example	Material
Binder jetting	AM process in which a liquid agent is selectively deposited to joint powder materials	3DP	Waxes Composites Polymers Ceramics
Directed energy deposition	AM process in which focused thermal energy is used to fuse materials by melting as they are being deposited	LENS	Metals
Material extrusion	AM process in which material is selectively dispensed through a nozzle or orifice	FDM	Thermoplastics
Material jetting	AM process in which droplets of build material are selectively deposited	MJM	Waxes Ceramics UV curable resins
Powder bed fusion	AM process in which thermal energy selectively fuses regions of powder bed	SLS	Waxes Thermoplastics Metals
		SLM	Metals
		EBM	Metals
Sheet lamination	AM process in which sheets of material are bonded to form an object	LOM	Paper Metals Thermoplastics
Vat photopolymerisation	AM process in which liquid photopolymer in a vat is selectively cured by light-activated polymerisation	SLA	UV curable resins

According to the Wohler's Report 2013 (Wohlers and Caffery 2013), the compound annual growth rate (CARG) of revenues of all AM products and services all over the world

over the previous 24 years was 25.4%, and the rate of growth was 27.4% over the period from 2010 to 2012, reaching \$2.2 billion in 2012 (Huang, Leu et al. 2015). Two years later, according to the Wohler's Report 2015 (Wohlers and Caffery 2015), the CARG over the previous 26 years increased to 27.3% while over the 3-year period from 2012 to 2014 it rocketed to an impressive 33.8%, reaching \$4.1 billion in 2014. These figures show that the AM industry has been on a healthy trajectory and it has excellent potential from the economic aspect. Besides, the worldwide revenue was expected to exceed \$100 billion by 2020 (Wohlers and Caffery 2012).

In 2015, two large companies in the USA, Stratasys Inc. and 3D Systems Inc., owned the majority of patents related to these technologies, and employed more than 4000 people worldwide, as reported by Wood (2015). This technology has already helped to transform several industry research sectors, such as prototyping, biomedical and automotive. In the last few decades it has developed in precision, detail and material quality. Improvements in strength, economics, fabrication speed and functionality have made AM suitable for the manufacture of end-use components, not just early stage prototyping (Wood 2015). According to Keating (2014) from the Massachusetts Institute of Technology (MIT), the spatial dimension is no longer a significant concern, with applications from printing a small biological cell to macro structures such as an entire building.

2.2 Existing 3D printing technology in concrete construction

Owing to stress concentrations, rectilinear buildings are weaker than curved structures, but they fit traditional construction techniques. AM-based construction (Keating 2014) could allow the introduction of curvature in buildings, thereby improving structural integrity. At this time, some researchers have invented machines based on technologies of material extrusion and binder jetting to print cementitious materials (Barnett and Gosselin 2015). Combined with

traditional processes (i.e. sculpting and mould-casting), five novel 3D printing-based construction techniques are introduced in this section, as shown in Figure 2-2.

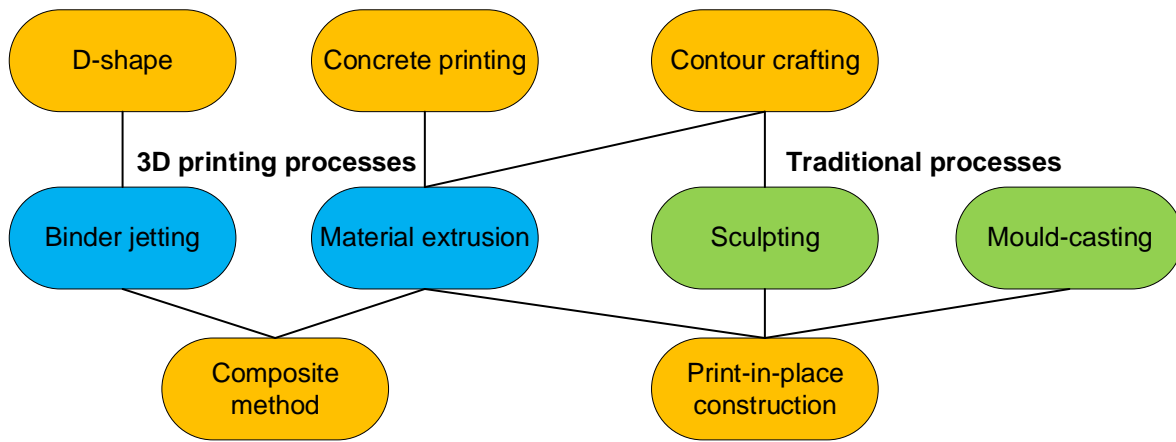


Figure 2-2 Five novel 3D printing-based construction methods (Xu, Chen et al. 2016).

2.2.1 D-shape

In 1997, Pegna used a powder-and-binder method to build structures up in layers, spreading a thin layer of cement and spraying a binder. The Italian inventor Dini (2016) developed a large 3D printer called the D-Shape, which made it possible to print structures in irregular shapes. The construction time required by D-Shape was about a quarter that of the traditional construction method, and the cost was just halved (Feng, Meng et al. 2015). Dini and his company, Monolite UK Ltd, patented this model in 2006. The D-Shape used a binder to selectively deposit the powder bed. In this process, a layer of powder bed was laid and compacted, and then the binder was selectively deposited by nozzles on a gantry frame controlled by the Monolite software (Craveiro, de Matos et al. 2012). The process was repeated layer by layer until a full 3D object was formed and extracted from the powder. Figure 2-3 illustrates the process.

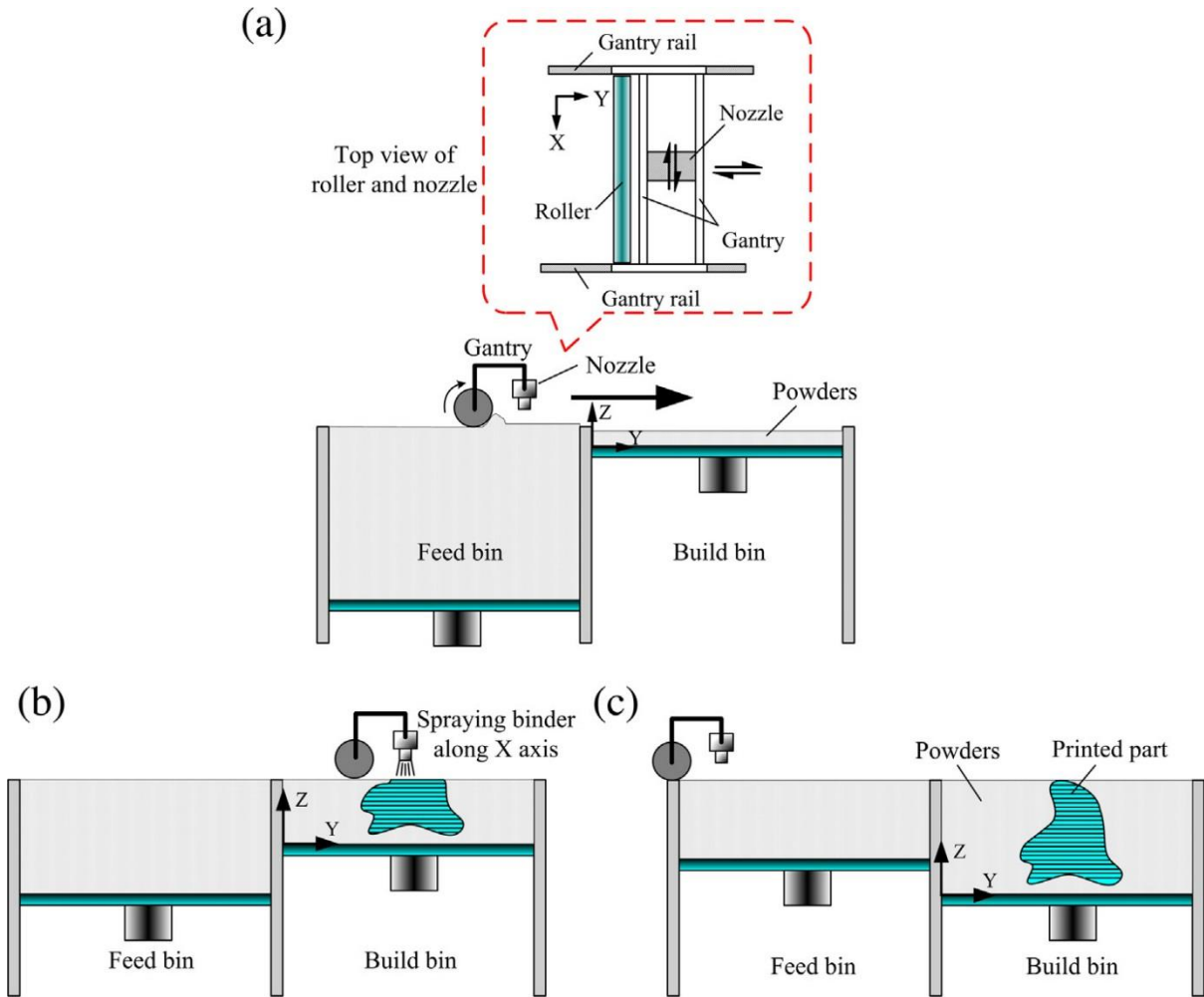


Figure 2-3 Schematic of D-Shape printing process: (a) before printing, (b) during printing, and (c) after printing (Feng, Meng et al. 2015).

Researchers at Tsinghua University tested the D-Shape method by producing oven-dried specimens comprised of a vinyl polymer and carbohydrate plaster powder injected with a water and humectant binder (Feng, Meng et al. 2015). This printing method proved to be capable of producing complex curved products that would be extremely difficult to replicate using traditional mould-casting techniques (Rael and San Fratello 2011), as exemplified by a freestanding 2.7 (H)× 3.6 (W) × 3.6 (L) m structure printed by UC Berkeley researchers (see Figure 2-4) (Williams 2015).



Figure 2-4 The 'Bloom' pavilion (Williams 2015) printed by D-Shape method.

2.2.2 Contour crafting

The contour crafting (CC) method involves the extrusion of wet concrete in 2D layers by an automated gantry as trowel-like fins attached to the print nozzle spread and shape the concrete into smooth forms (Link 2015). The layered concrete filaments are hardened and bind together without the need of formwork, creating the desired 3D object. Generally, a concrete tank attached to a mobile truck supplies two nozzles with cement, with a trowel smoothing the outside for a clean and paint-ready surface. Once a horizontal layer is completed, the height of gantry is increased, and the next layer is printed. Figure 2-5 shows the schematic process.

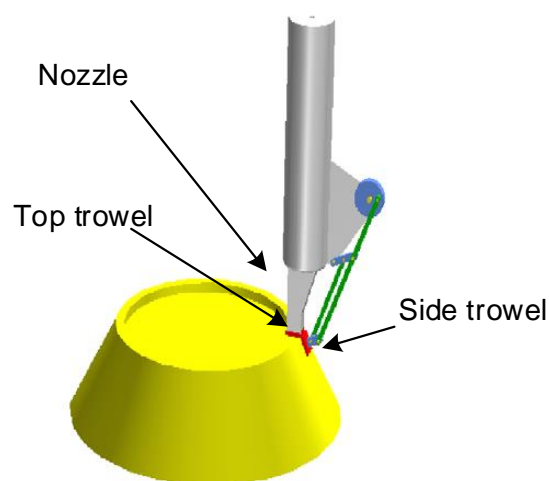


Figure 2-5 Schematic of contour crafting method (Khoshnevis 2004).

This method has been used by researchers at the Loughborough University to print specimens comparable in compressive strength to mould-cast specimens, using a fine sand aggregate mixed with ordinary Portland cement CEM I 52.5 (Leach, Carlson et al. 2012). In the commercial sphere, CC has been successfully implemented by the Chinese company Yingchuang - WinSun, to build ten houses within one day where each house cost \$7,000 (see Figure 2-6) (Havencab 2016). In addition to civil structures, potential applications of CC include low-income housing, emergency shelters and lunar applications (University of Southern California 2014).



Figure 2-6 The highest building worldwide by 3D printing (Havencab 2016).

2.2.3 3DCP technique

Concrete Printing, commonly referred to as 3D Concrete Printing (3DCP), is an extrusion technique developed at Loughborough University (Lim, Buswell et al. 2011). Figure 2-7 shows the process. This method is similar to CC, but it has some advantages. First, the single nozzle (9mm) is smaller than that in CC and furnishes a higher resolution (Eindhoven University of Technology 2015). Also, it retains the 3D freedom assisted by a round nozzle. This makes the tool path simpler as it is independent of the deposition direction (Lim, Buswell et al. 2012). 3DCP does not require the additional axis of rotation needed by rectangular shaped nozzles.

Furthermore, the oval shaped extruded filament maximises the interface, thereby improving interlayer bonding (Lim, Buswell et al. 2012). The mix is cement and gypsum; is a high-performance material commonly used in the construction industry. However, it does require a high degree of control (Lim, Buswell et al. 2011).



Figure 2-7 Concrete printing process (Alec 2014).

2.2.4 Composite method

The composite method utilises extrusion and powder-printing to create powder-supported, extruded 3D objects. Each layer of extruded cementitious material is surrounded by a layer of granular cementitious powder by an automated gantry with dual printing nozzles. Binder is then extruded to harden certain parts of the granular support, producing a multi-material piece (Dezeen 2016). Figure 2-8 illustrates the composite method.



Figure 2-8 The composite method (Jimenez Garcia 2016)

So far, this method has only been tested by students from the Bartlett School of Architecture in their project Amalgamma, where they successfully created both structurally strong and geometrically precise objects (Dezeen 2016).

2.2.5 Print-in-place construction

Researchers at MIT succeeded in providing an emerging idea by combining 3D printing processes and conventional formwork construction methods (see Figure 2-9). Akin to a mould, the “print-in-place” formworks are compatible with pouring any castable material inside. The method provides the possibility of selecting materials with a wide range of tailored properties, such as rapid production and monolithic cast strength. With the use of BASF polyurethane material with a fast curing time, foam can be printed layer by layer into formwork, providing thermal insulation. The process, termed Print-in-Place construction, is designed for on-site fabrication of formwork for castable structures, such as concrete exterior walls and civil infrastructure (Keating and Oxman 2012). After the mould is printed, a conventional concrete casting method is applied (Keating 2014).

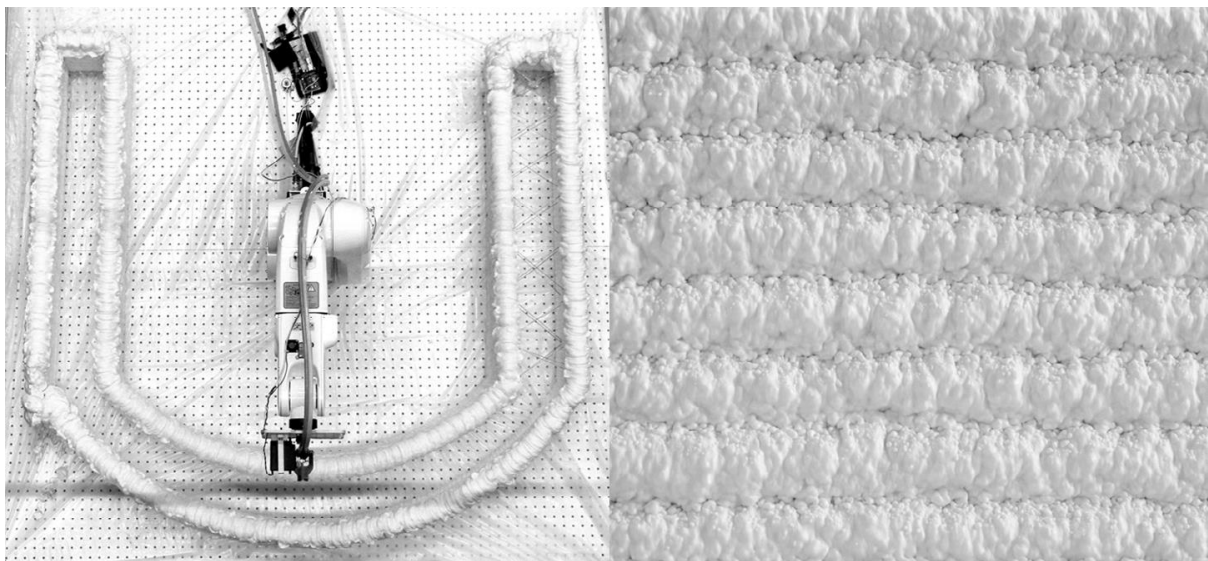


Figure 2-9 Additive fabrication tests using polyurethane spray foam (left) produced test isolative formwork samples with consistent and tunable layer heights (right) (Keating 2014).

Moreover, sculpting may be used to modify this process. Secondary milling techniques improve the surface finish and reduce manufacturing time. The resolution of this modified process is shown in Figure 2-10.



Figure 2-10 Combining additive and subtractive processes in the Print-in-Place construction method

2.3 Challenges of existing methods

According to the summary by Xu et al. 2016, only two processes in 3D printing catalogues, binder jetting and material extrusion, are applied in concrete construction. Combined with two traditional processes, sculpting and mould-casting, five existing 3D printing applications in the cementitious construction industry are reviewed. They are D-Shape, concrete printing, CC, composite method, and Print-in-Place construction. Figure 2-2 shows the relationships between each method and the processes (Xu, Chen et al. 2016). However, there are some obstacles facing the 3D printing concrete method including mechanical properties, reinforcements, curing conditions, durability, interlayer bonding, the relationships among hardening time, pumpability and extrudability, and applicability (Xu, Chen et al. 2016).

2.3.1 Mechanical properties

Deterioration of mechanical properties is a major problem in both powder-based (D-Shape) and extrusion methods (CC and 3DCP). The current D-Shape method may only be suitable for

printing non-structural components, as the material printed by the team at Tsinghua University was very brittle with low compressive strengths around 14 MPa and flexural strengths about 4 MPa (Feng, Meng et al. 2015). The extrusion process also affects mechanical properties. Detailed studies have shown that crack density increases when compared to a cast equivalent mix (Leach, Carlson et al. 2012). Researchers have suggested that the use of high-performance concrete (compressive strength up to 88MPa) is required for 3D printing to meet industry standards (Lim, Buswell et al. 2011). Flexural strength is significantly decreased when loaded at an angle perpendicular to the surface and parallel to printed layers, in which case the tension between the layers results in up to 36% reduction in flexural strength (Leach, Carlson et al. 2012, Lim, Buswell et al. 2012). Similarly, the direct tensile strength is reduced by 23% in such loading conditions (Leach, Carlson et al. 2012).

2.3.2 Reinforcements

In the existing seven categories of 3D printing processes, the incorporation of reinforcements is rarely incorporated, but they are introduced in CC and 3DCP processes. In CC, multiple robotic modules allow for the concurrent implementation of other components, such as insulation or imbedding steel reinforcements (Leach, Carlson et al. 2012). However, the system with an additional mechanical arm increases the complexity in both machining systems and structural designs, leading to extra cost. In 3DCP, voids for conduits designed into the model can be created precisely for the post-placement of utilities or reinforcements. Tensile capacity can be improved by inserting steel bars which are post-tensioned and grouted into place (Lim, Buswell et al. 2012). However, in this method, the implementation of reinforcements is done by labour. The process cannot avoid being labour-intensive and not cost-effective.

2.3.3 Curing

Special curing methods are essential for 3D printed components, which are usually built without formwork. Formwork is also an important barrier to prevent drying of early-age concrete. 3D printed concrete is particularly susceptible to shrinkage cracking, since additional surface area is exposed to evaporation (Leach, Carlson et al. 2012, Yang 2015). It has been found that surfaces exposed to evaporation tend to have decreased flexural strength. Shrinkage cracking occurs when evaporation rates cause concrete to dry out before it sets. Cracking also occurs on the surface of concrete while it is still plastic. When the evaporation rate is greater than the bleeding rate, water recedes below the concrete's surface and forms a menisci between fine cement and aggregate particles, causing a tensile force to develop in the surface layers as are pulled together, and leading to tensile capillary pressure and cracking (National Ready Mix Concrete Association 1998). When a good level of curing is provided, this shrinkage can be kept to an acceptable level (Le, Austin et al. 2012). In addition, excessive loss of water may hinder the hydration reaction of some cement binders.

2.3.4 Hardening time, pumpability and extrudability

Another key challenge is balancing hardening time, pumpability and extrudability. Pumpability is defined as the capacity of concrete to be pumped from the original place with lower gravity potential in a tube to a higher place; extrudability is defined as the capacity of concrete to pass through the narrow tubes and nozzles of printing head and as well as the ability to maintain its extruded shape. These properties are significantly influenced by the mix proportions and the presence of additives including pozzolanic particles, superplasticiser, retarder, accelerator and fibres.

2.3.5 Durability

Durability is always a concern in any concrete construction. Durability is the ability to last a long time without significant deterioration. With respect to concrete, factors influencing durability include resistance to freezing and thawing, resistance to sulphate attack, chloride resistance and resistance to ASR. In 3D printing processes, rapid hardening cement systems, such as calcium sulphoaluminate cement systems, usually contain more ettringite for higher early strength (Taylor 1997). However, the rich ettringite content can lead to poor durability with severe damage to concrete structures due to delayed ettringite formation (DEF) (Taylor, Famy et al. 2001). Also, rapid hardening produces some more side effects with regard to the durability of concrete structures, including lower crack resistance, higher dry shrinkage, higher interlayer corrosion risk and water penetration effects.

Among the durability problems, ASR, a typical type of AAR, can significantly damage concrete in the long term. It is the result of the chemical reaction in concrete between the hydroxyl ions associated with the alkalis sodium and potassium within the structure of cement and the reactive silica within the structure of the aggregates (Farny and Kosmatka 1997). Originally, the structure of quartz (SiO_2) is composed of three-dimensionally linked ($\text{O}_2\text{-Si-O}_2$) silica tetrahedral sharing their oxygen, and the surface is different with unsatisfied charges and loose bonds, especially in poorly crystalline silica. Then, dissolved hydroxyl (OH^-) attaches to unsatisfied siloxane bonds (Si-O-Si) present at the silica surface, forming silanol (Si-OH) groups (Vivian 1951). After that, the silanol (Si-OH) groups combine with sodium and potassium ions, and an alkali-silica gel is formed between the aggregate surface and cement paste. Finally, the hydrophilic alkali-silica gel absorbs water and expands. The resultant internal stress exceeds the tolerance of the aggregate and surrounding cement paste, leading to spalling and cracks (Fernandes and Broekmans 2013). Based on the reaction processes, there three necessary conditions have been summarised for ASR. They are the presence of sufficient

water, sufficient availability of alkalis, and ASR reactive aggregate. ASR is also called concrete cancer (Collepari 2010). It results in deleterious effects such as internal deterioration, cracking, movement and displacement, discoloration and dark patches, efflorescence and exudations, and pop-outs (Clark 1989).

2.3.6 Applicability

Applicability is another crucial issue in the 3D printing technology of concrete. Applicability of 3D printing technology relies on the ease of implementation on site or in local factories. Originally, D-Shape was designed for off-site production and many successful projects were completed. The technique has been used for artistic statues or smaller scale structures such as gazebos and swimming pools. Feasibility in full scale building construction is not yet evident (Dini 2016). Ongoing research seeks to demonstrate the potential for local, on-site printing. Moreover, in some printing techniques such as 3DCP, the aggregate must be very fine (the maximum size of used aggregate being 2 mm (Le, Austin et al. 2012, Le, Austin et al. 2012)), constrained by the small (9 mm) diameter of the nozzle. This size constraint limits the mix design and affects the applicability of the technique in areas lacking suitable aggregates.

2.3.7 Interlayer bonding

The bond strength between printed layers is a critical mechanical property of objects produced by an AM process (Le, Austin et al. 2012). It affects the structural performance, particularly when the process temporarily stops between layers. It leads to low shear strength in the interlayer region where two concrete layers are attached to each other (Le, Austin et al. 2012, Sanjayan, Nematollahi et al. 2018), which contributes to the free water on the concrete layer surfaces reported in some studies (Gillette 1963). Weak interfacial bonding between layered concrete greatly reduces flexural strength in printed specimens. Le et al. (Leach, Carlson et al.

2012) found that printed specimens exhibited flexural strength of approximately 6 MPa when load was applied in-plane with layers, whereas mould-cast specimens of the same composition exhibited flexural strengths of about 11 MPa. However, a certain amount of water required for a SSD state is deemed necessary to achieve good adhesion between layers (Austin, Robins et al. 1995). In addition, some studies have cited the lack of stability and eccentricity in freshly printed concrete as other important shortcomings (Wolfs, Bos et al. 2018). These problem limit the application of 3D-printing concrete in the safety contexts, e.g. providing housing for survivors in post-disaster sites. Traditionally, according to current codes (CAN 2004, Institution 2004, Committee, Institute et al. 2008), factors influencing bonding are (1) concrete compressive strength, (2) normal stress at interface, (3) amount of reinforcement crossing the interface, and (4) the roughness of the substrate surface (Santos and Júlio 2011). However, when it comes to 3D printing concrete, the influence factors can be extremely divergent.

Many researchers have conducted investigations with regard to this issue, seeking solutions to improve interlayer bonding apart from traditional concrete repair theory. One attempt has been made by Lou et al. (Le, Austin et al. 2012) to assess the effectiveness of fibres in the interlayer region. However, fibre reinforcement is not as beneficial as it should be, due to the lack of chemical bonding between the fibres and the cementitious mix. In another study, Yusuo and Xiaozhi in 2016 (Wang and Hu 2016) applied two research conditions: a) epoxy only, and 2) epoxy with short Kevlar fibres 6 mm in length. The results showed the effectiveness of the incorporation of epoxy, and the group with epoxy and Kevlar showed better interfacial strength. Recently, Sanjayan, Nematollahi et al. (2018) investigated the effects of time delay on interlayer strength, with the delay time and interlayer moisture level as the influential factors affecting cement strength.

2.4 Techniques for improving performance of 3D printing layered concrete

Among the summarised seven challenges of existing 3D printing technologies of concrete, the interlayer bonding is very significant and is currently investigated by researchers. In this section, four techniques are introduced to address the issue. Epoxy and PVA fibres assist to improve the interlayer bonding strength itself. GO is used for reducing ASR, which leads to severe dimensional changes and cracks in 3D printed concrete layers. TMDs is studied for potential sensing purposes for 3D printed concrete.

2.4.1 Epoxy

Epoxies, also known as epoxy resins, are a class of reactive prepolymers and polymers with an epoxide functional group (May 1987). They usually react with themselves by catalytic homopolymerisation, or with specific co-reactants including polyfunctional amines, acids, phenols, alcohols and thiols. Epoxy has outstanding properties such as excellent mechanical strength (up to 190 MPa compressive strength, 112 MPa flexural strength, and 85 MPa tensile strength), superior resistance to heat (survives up to 177° (Morena 1988)), good resistance to chemicals, and great adhesive strength. Epoxies have now been widely applied in paints and coating, adhesives, industrial tooling and composites, wind turbine technology composites, electrical systems and electronics, petroleum and petrochemical, consumer and marine applications, aerospace applications, biology, and art.

2.4.2 Polyvinyl alcohol (PVA) fibre

PVA fibre, short for polyvinyl alcohol fibre, was used as glue for adhering pieces of paper together. Then, it became an excellent wood glue. After that, it became an extremely versatile,

waterproof adhesive and sealer, and had an extraordinary number of uses in building construction. Now, it is widely added into cement and mortar to achieve superior mechanical properties (Betterman, Ouyang et al. 1995, Ong, Basheerkhan et al. 1999, Hossain, Lachemi et al. 2013, Noushini, Samali et al. 2013). Moreover, engineered cementitious composites with PVA fibres, called ECC-PVA, have been widely investigated and adopted in applications due to their excellent properties and cost-effectiveness (Pan, Wu et al. 2015).

2.4.3 Graphene oxide (GO)

As a graphene derivative, GO consists of a hexagonal carbon network bearing hydroxyl, epoxide, carboxyl and carbonyl functional groups. These oxygen-containing functional groups render GO sheets hydrophilic and highly dispersible in water (Qiu, Yang et al. 2010). The various functional groups coupled with the large surface area create a highly reactive GO nanomaterial. Therefore, GO has emerged as a potential nano-reinforcement due to the improvement in solubility, ease of production and positive interaction with cement matrix. Detailed information on the fabrication and characterisation of GO cement can be found in the recent US patent (Pan, Duan et al. 2012) filed by CI Duan. The results show that GO sheets can significantly improve compressive strength, flexural strength and fracture toughness as well as the pores of cement.

2.4.4 Transition metal dichalcogenides (TMDs) (MoS₂ and WS₂)

MoS₂ has a two-dimensional layered structure consisting of covalently bonded S-Mo-S sheets, which are unit elements of the bulk material (Splendiani, Sun et al. 2010). The layers are bound by van der Waals force to form the bulk MoS₂. Since the interaction of van der Waals force is not strong enough to maintain the bulk under some circumstances, freestanding monolayer MoS₂ are expected to exist, and can also be fabricated (Mak, Lee et al. 2010, Radisavljevic,

Radenovic et al. 2011, Ganatra and Zhang 2014). The crystal structure in WS_2 is almost the same, with a tungsten atom substituting in the position of the molybdenum atom. In other words, monolayer WS_2 is also valid. Figure 2-11 shows the crystal structures of MoS_2 and WS_2 .

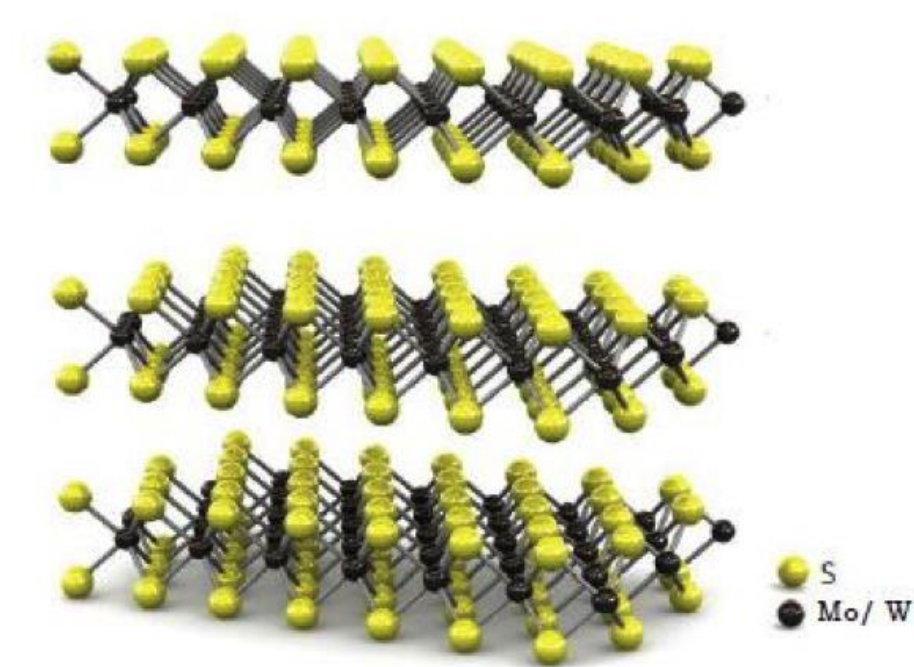


Figure 2-11. Layered crystal structure of MoS_2 and WS_2 (Radisavljevic, Radenovic et al. 2011)

Because the thickness of the monolayer structures is very small, the elastic properties of strength and Young's modulus are expected to be high. Several groups have investigated the relative properties of monolayer MoS_2 ; Table 2-2 summarises the results.

It has been found that the mechanical strength of MoS_2 is relatively high. The Young's modulus is similar to that of steel, which is 206.4 to 210.1 GPa at room temperature (Ledbetter 1981). Theoretically, monolayer WS_2 should have similar properties.

Table 2-2 Elastic properties of monolayer MoS₂.

Reference	Mechanical Properties	
	In-plane stiffness (N/m)	Young's modulus (GPa)
Bertolazzi, Brivio et al. (2011)	180 ± 60	270 ± 100
Yue, Kang et al. (2012)	123	N/A
Castellanos-Gomez, Poot et al. (2012)	N/A	330 ± 70
Cooper, Lee et al. (2013)	N/A	210
Liu, Yan et al. (2014)	N/A	171 ± 11

Photoluminescence (PL) spectroscopy is widely used to characterise electronic and optical properties. In this project, MoS₂ and WS₂ are investigated by photoluminescence.

Photoluminescence occurs when the excitation is effective with photon energy larger than the bandgap of the semiconductor. Light emission is the behaviour.

The CVD method has been reported by a number of groups to successfully fabricate thin MoS₂ or WS₂ flakes with different parameters and different substrates (Zhan, Liu et al. 2011, Lee, Zhang et al. 2012, Shi, Zhou et al. 2012, Van Der Zande, Huang et al. 2013). Figure 2-12(a) shows a typical CVD schematic principle.

Lee et al. (2012) reacted MoO₃ and sulphur powder on SiO₂/Si substrates. The temperature of the reaction chamber was 650°C, and N₂ was applied in the chamber during reaction. The result was of good quality, with star-shaped and atomically thin products. Similarly, Zhan et al. (2012) made that by using Mo thin films as precursors. The temperature in the reaction chamber was controlled to rise from room temperature to 500°C, then to 700°C. The temperature of the sulphur powder was kept 113°C. Shi et al. (2012) decreased the chamber temperature to 400°C, and obtained atomic thickness MoS₂ flakes grown on graphene surface depositing on Cu substrate. Van der Zande et al. (2013) used the same method and parameters as Lee et al. (2012) to fabricate MoS₂. For improvement, careful cleaning of the substrates led

to higher quality products: no seed was observed in the centre of the flakes. Figure 2-12(b) and (c) show high-quality example samples fabricated by van der Zande et al. (2013). The flakes are relatively large with smooth surfaces.

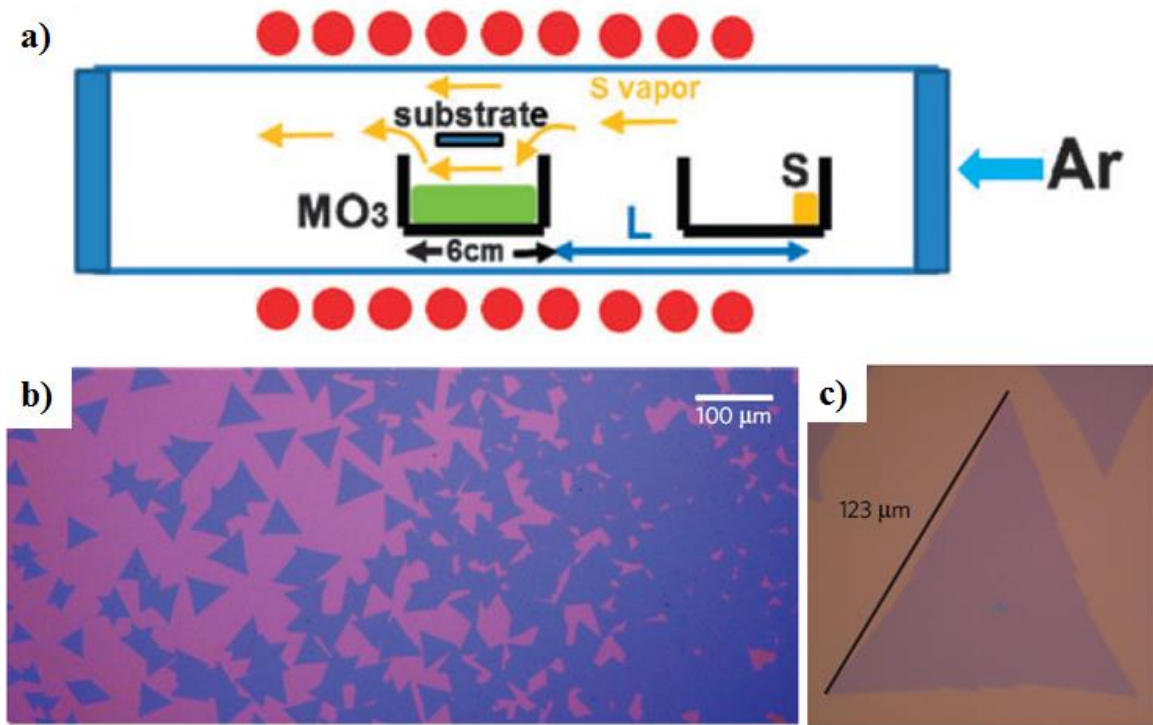


Figure 2-12 a) Typical CVD principle for fabricating thin MoS₂ samples; b) and c) Optical image of MoS₂ flakes grown by van der Zande et al. (2013)

As is well known, the transfer technique is significant for transferring grown materials to new arbitrary substrates. A number of investigations can subsequently be carried out with the flakes on corresponding substrates. The PMMA-assisted transfer technique is widely used.

PMMA-assisted transfer technique is common for graphene, but it can also be applied for MoS₂. Figure 2-13 shows a typical PMMA-assisted MoS₂ transfer process. First, a thin PMMA film is spin-coated onto the original substrate surface on which MoS₂ is grown (sapphire substrate). Then, the sample is soaked in an alkaline solution (usually as KOH or NaOH solution) for a period of time. If needed, the solution can be heated to accelerate the reaction rate. After that, the PMMA film should separate from the original substrate with the

MoS₂ sample attached on it. The film is then placed on the surface of DI water for cleaning purposes, with the assistance of buoyancy, and fished out by a desired new substrate. After it is baked on a hot plate to dry, the experiment concludes. Figure 2-13 shows a schematic of the PMMA-assisted transfer process.

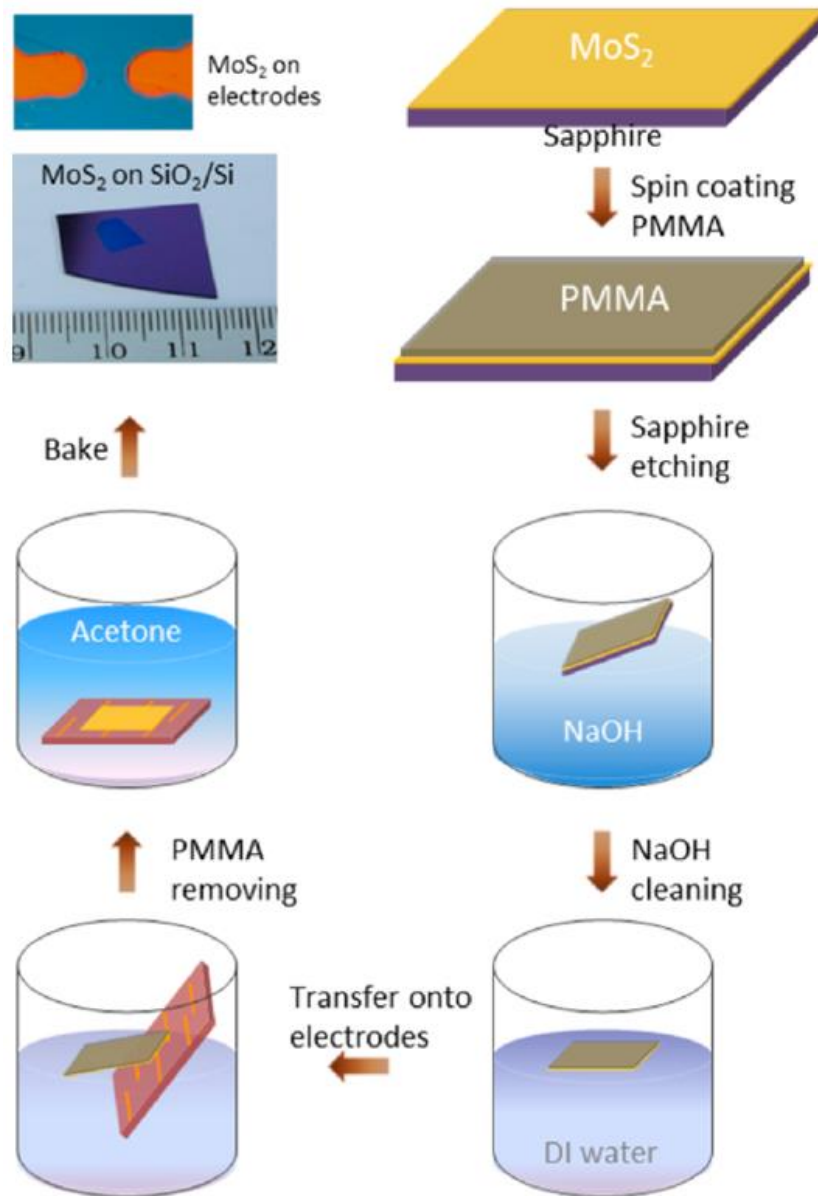


Figure 2-13 Schematic of PMMA-assisted transfer process (Lu, Lu et al. 2014).

Several groups have reported their parameters for this transfer technique, including the concentration of the alkaline solution, the soaking time of the sample in alkaline solution, and the heating temperature of the alkaline solution (Zhan, Liu et al. 2011, Lin, Zhang et al. 2012,

Chiu, Li et al. 2014). Lin et al. (2012) succeeded in transferring CVD-grown MoS₂ on SiO₂ substrates in 2 Mol/L NaOH solution at 100°C for 30 min. Chiu et al. (2014) followed the footprint to stack monolayer MoS₂ on WSe₂ flakes. Zhan et al. (2012) dipped an MoS₂ sample covered by PMMA film into 15 Mol/L KOH solution without heating the solution, and successfully separated the MoS₂ sample directly from the original SiO₂ substrate.

Chapter 3. Investigation of interlayer bonding between 3D printed mortar layers using epoxy adhesive

3.1 Introduction

As introduced in previous chapters, 3D printing technology has the potential for popular use in concrete construction in the future due to its advantages. It is cheaper in production cost and time, incurs lower injury rates at work, helps to create more technology-based jobs and benefits the implementation of complex views in building art (Nematollahi, Xia et al. 2017). Meanwhile, material extrusion processes are widely used for in-situ construction, and successful examples were presented in Chapter 2. If the differences between each method are ignored, the mechanism in summary is the extrusion of cementitious materials from a nozzle layer by layer. After the substrate has hardened to form ideal structures, the upper layer material is extruded over the substrate. By repeating this procedure, a monolithic structure can be manufactured, depending on the printing device capacity and velocity. However, the weak point of the whole structure can be identified as the interlayer region because of the interval time between printing successive layers, which makes it impossible for two layers to merge completely. Meanwhile, stress concentration can occur due to potential flaws caused by the loose merge between two layers, which may also considerably reduce the interlayer strength. In summary, the strength of 3D printed cementitious materials is highly dependent on the interlayer bonding strength (Le, Austin et al. 2012). According to reports, the interlayer strength of printed concrete is 0.2 to 0.65 MPa, which is very weak compared to the tensile strength of cast-in-place concrete. At this stage, the huge gap between 3D printing technology of concrete and conventional concrete

construction is the reason for endeavouring to enhance the interlayer bonding strength of the former up to real coherence, as high as that of integrated concrete.

Based on the foregoing literature review, when concrete-to-concrete bonding is considered, concrete repair theory becomes the principle. Only four factors are considered by current codes: a) the concrete compressive strength; b) the normal stress at the interface; c) the amount of reinforcement crossing the interface; and d) the roughness of the substrate surface (Santos and Júlio 2011). However, when these factors are applied to 3D printing of concrete, they cannot contribute very much to improving the interlayer bonding to equal that of integrated concrete. Many researchers have conducted investigations with regard to this issue, seeking solutions to improve interlayer bonding apart from traditional concrete repair theory. One trail was followed by Lou et al. (Le, Austin et al. 2012), who assessed the effectiveness of fibres in the interlayer region. However, fibre reinforcement is not as beneficial as anticipated, due to the lack of chemical bonding between the fibres and the cementitious mix. Another course of investigation was taken by Yusuo and Xiaozhi in 2016 (Wang and Hu 2016), who compared two conditions in their research: a) epoxy only, and b) epoxy with short Kevlar fibres 6 mm in length. The results showed the effectiveness of the incorporation of epoxy, and the group with epoxy and Kevlar showed better interfacial strength. Recently, Sanjayan, Nematollahi et al. (2018) investigated the effects of time delay on interlayer strength, with the delay time and interlayer moisture level found to be as the influential factors affecting cement strength.

In this section, research is conducted to investigate the issue, with the aim of improving interlayer bonding strength as much as possible, up to real coherence. The research plan is to apply a thin layer of epoxy resin between two layers of cementitious materials, mortar in this case. After that, the advanced plan is the incorporation of PVA fibres between epoxy and mortar to increase interlayer bonding strength between mortar and epoxy. For both plans,

experimental work is necessary to simulate 3D printing conditions and to test mechanical strength for comparison purposes. Meanwhile, parameters, curing conditions, and printing interval time are adjusted to determine the optimum situation. After experimental work, SEM characterisations are conducted to find the mechanism of the improvement. Meanwhile, MD and quantum calculations are used to assess the effect of epoxy resin applied in the interlayer region of 3D printed mortar, to compare with the experimental work.

3.2 Experimental program

3.2.1 Materials

In this study, 3D printed cementitious materials are simulated, to achieve the final specimen size of 80*80*20mm. In this case, mortar with sand as aggregate is applied instead of concrete. GP (General Purpose) Cement conforming to AS 3972 is used as binder to ensure that the properties are the same in each batch. The water for mixture is tap water. Construction sand is heated and dried for over 12 hours before mixing. Sika ViscoCrete-2100, a type of high-range water-reducing admixture, is used to improve the workability of the mortar. The water/cement ratio is 0.3. The sand/cement ratio is 1.5. The Sika ViscoCrete-2100/ cement ratio is 0.3%. The mould size is 80*80*80mm, and the first-demoulded specimen before cutting is a cube. Meanwhile, the epoxy resin Araldite 2000+ is used, and the ratio between Part A and Part B is 1.25. The foregoing specifications are for the materials preparation for specimens with epoxy but without fibres. For specimens with fibres, PVA fibres are used with the length of 13mm and diameter of 0.1mm. The volume of epoxy is 0.3%.

3.2.2 Experimental methods

Mortar is mixed conforming to ASTM C 305. For each mixture, 150g water is placed in a bowl with 1.5g superplasticiser. After adding 500g cement, the mixer is started to mix at slow speed (140 r/min) for 30 seconds. Over the next 30 seconds, 750g sand is gradually added into the bowl at slow speed mixing rate. Then, the mixer is accelerated to medium speed (285 r/min) for 30 seconds. Finally, after a pause of 90 seconds, the mixing procedure concludes by mixing for 60 seconds at medium speed (285 r/min).

The epoxy is mixed by a planetary centrifugal epoxy mixer. For each mixture, 33g Araldite Part A and 26.4g Araldite Part B are mixed into a container, and the container is put into the mixer to mix for 3 mins at the rate of 2000 rpm. For specimens with PVA fibres, 1.4g PVA fibres are added into the container together with two parts of epoxy. The mix design is shown in Table 3-1.

Table 3-1 Mix design for mortar-epoxy system (weight: grams)

	Mortar	Mortar with epoxy	Mortar with epoxy and PVA
Cement	500	500	500
Water	150	150	150
Sand	750	750	750
Sika ViscoCrete-2100	1.5	1.5	1.5
Araldite 2000+ Part A	0	33	33
Araldite 2000+ Part B	0	26.4	26.4
PVA Fibres	0	0	1.4

After the mortar has been mixed, the first layer of mortar is cast. The mould size is 80*80*80mm, and the first layer of mortar is 80*80*38.5mm (L*W*H). The surface of the mortar layer is smoothed, and the layer is vibrated on a vibration table for 30 seconds. After half of the printing interval time, a layer of epoxy 3mm in thickness is cast over the first layer.

After waiting for the duration of the other half of the printing interval time, the second layer of mortar (80*80*38.5mm) is cast over the layer of epoxy, and the vibration table is used to compact as well. A two-dimensional schematic is shown in Figure 3-1(a).

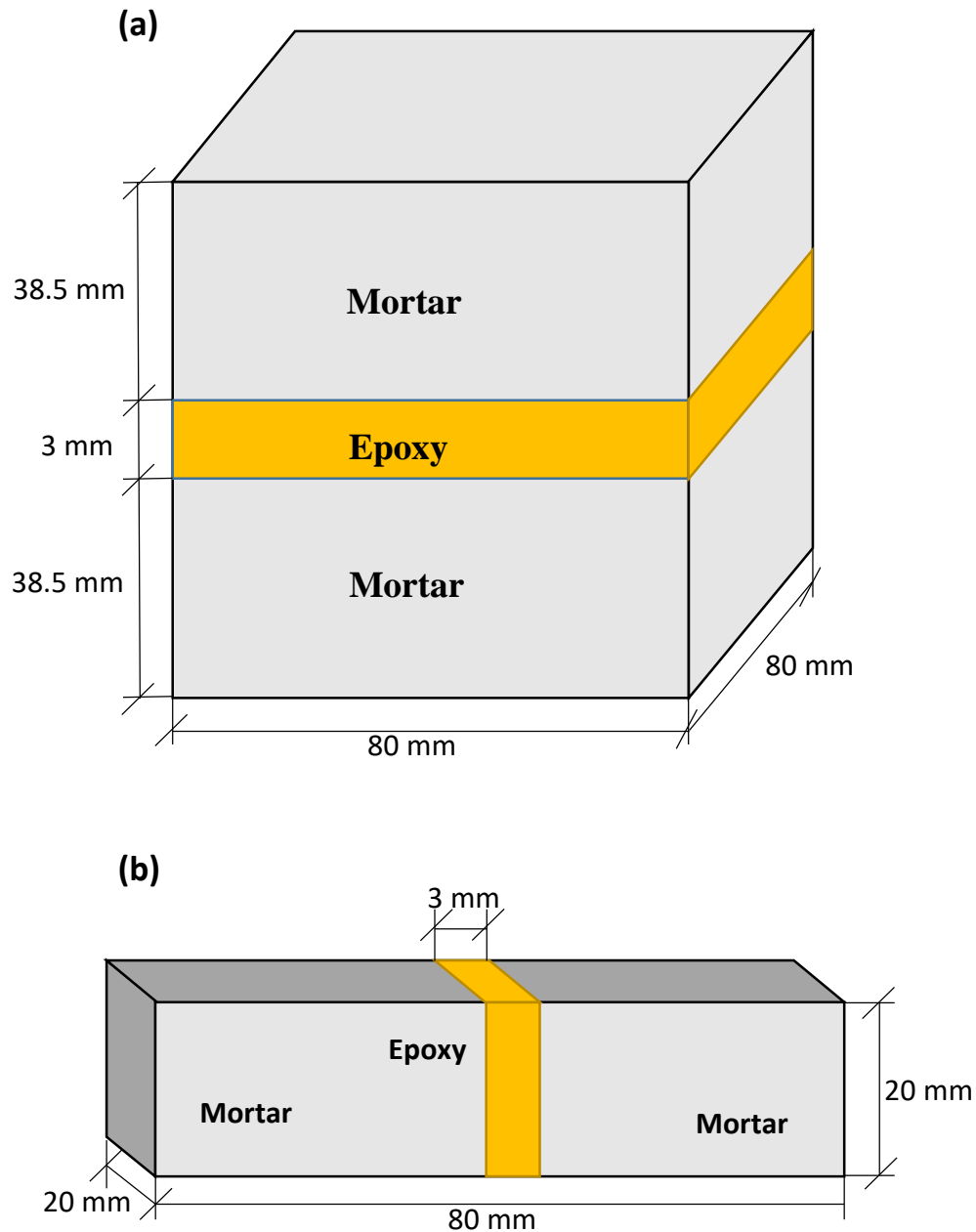


Figure 3-1 Schematic of the specimens: a) the procedure to cast cubic specimens; b) the final specimen used for strength test by cutting.

Following one day of hardening, the cubic specimens are demoulded and cured in saturated lime water at 20 degree. This curing is mainly for the mortar. One day before each

strength test, the cubic specimens are taken from the curing tank to be cut into specimens 20*20*80mm in size. A schematic of the specimen is shown in Figure 3-1(b). After that, these specimens are cured in an oven at a specified curing temperature for 10 hours to cure the epoxy part. Finally, strength testing is applied. Table 3-2 shows the experimental schedule.

Table 3-2 Experimental schedule.

Day	Actions
1	Mix mortar. Cast cubic specimens.
2	Demould cubic specimens. Cure them in lime water for mortar.
7	Cut cubic specimens into stick specimens. Cure them in oven for epoxy.
8	Conduct 7 days strength testing.
14	Cut cubic specimens into stick specimens. Cure them in oven for epoxy.
15	Conduct 14 days strength testing.
28	Cut cubic specimens into stick specimens. Cure them in oven for epoxy.
29	Conduct 28 days strength testing.

For mechanical strength testing, a three-point bending test is applied to test the tensile strength between interlayer structures. Figure 3-2 shows schematics of both the load path and a cross-section of the test, under ‘Instron 4204 50kN’. The distance between two rollers was 65mm, and the loading rate was 0.02 mm/min. The tensile strength can be calculated by the formula $\sigma = \frac{My}{I}$.

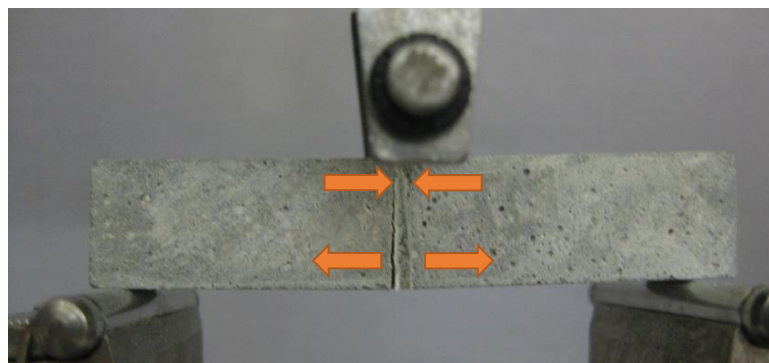


Figure 3-2 load path for 3-point bending test

3.2.3 SEM characterisation

Scanning electron microscopy (SEM) is a type of microscopy using a focused beam of electrons scanned over the surface of a sample to reconstruct a magnified image of the sample surface. It can be used to reveal information about a sample's morphology, topography and chemical composition, using different available detectors. In this study, SEM is used to characterise fracture surface morphology to investigate the failure type and potential mechanism between mortar and epoxy (and PVA fibre). Figure 3-3 shows a fracture surface to be scanned by SEM.

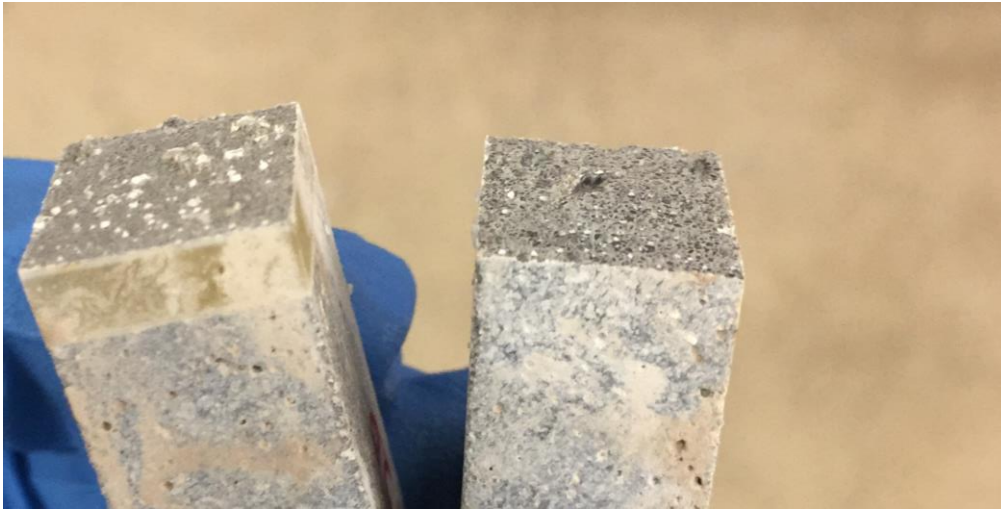


Figure 3-3. Fracture surface by three-point bending test for SEM scanning

3.3 Molecular dynamics simulation

This section corresponds to declarations #4 and #5.

In this study through MD simulation, two pairs of bonding are investigated. One is the effects of epoxy adhesive on the performance of the interlayer zone of 3D printing mortar, and the other is a new type of sulphur-carbon (BCS) polymer. Resin and calcium silicate hydrate (CSH) gel unit cells of modified cementitious composites were built and optimised separately. A new model of the nanoscale interactions between CSH and epoxy resin was introduced. The

trajectories of atoms and molecules of CSH and epoxy resin were determined by numerically solving Newton's equations of motion for a system of interacting particles, where forces between the particles and their potential energies were calculated using interatomic potentials and COMPASS force field. Also, density functional theory (DFT) calculations were utilised to assess the valence electron density and charges to help further assess the interaction between these materials.

A tobermorite 14Å structure CSH model was adopted to simulate the CSH matrix (Tao and Shahsavari 2017). The model was intended to preserve the periodic boundary conditions in three dimensions, thus presenting a suitable model for the reinforcing role of epoxy resin and its thermodynamic interactions with the CSH matrix. In the designed cell, epoxy resin was wrapped in CSH matrix on all sides. The dimensions for the periodic cell of CSH-epoxy resin was set to $78.5 \text{ Å} \times 108.5 \text{ Å} \times 153.9 \text{ Å}$. A COMPASS force field (Wei, Wang et al. 2017) was adopted to model the interatomic interactions between epoxy resin and CSH matrix. The designed system should come to equilibrium at its lowest energy level. Optimisation of the structure and minimisation of the energy level were achieved using the SMART method, which is a combination of the steepest descent, conjugate gradient and Newton–Raphson method (Al-Ostaz, Wu et al. 2010). For the system to reach $P = 0.001 \text{ GPa}$ (air pressure) and $T = 298 \text{ K}$ (room temperature), a total analysis time of up to 300 Ps with an NPT ensemble was employed to optimise the shape of the supercell. To control the temperature and pressure respectively, Nose thermostat and Berendsen Barostat were set (Berendsen, Postma et al. 1984). To preserve the equilibrium, changes in energy, temperature and density were monitored until they fluctuated around a constant value. To reach a homogenous volume structure, an NVT ensemble for 300 PS was employed.

DFT calculations were performed through the Cambridge Serial Total Energy Package (CASTEP) (Clark, Segall et al. 2005). To calculate the distribution of electron density between

atoms, the spin-polarised (Topsakal and Ciraci 2010) generalised gradient approximation (GGA-PW91) was used (Perdew 1992). The cut-off energy of plane waves responsible for basis set size determination was obtained as 700 eV. The energy and electronic calculations were done using k-point sampling for the Brillouin zone by 4×4×1 Monkhorst-pack k-point mesh. Full atomic relaxation was achieved when all remaining forces went below 0.01 eV Å⁻¹.

3.4 Results and discussion

In this section, the results of the aforementioned experimental program, SEM characterisations, and MD simulation are presented. First, the effectiveness of epoxy adhesive to improve mortar interlayer bonding is reported by mechanical tests. SEM characterisation proves the physical mechanism and MD simulation provides evidence in the chemical bond aspect. Second, by introducing PVA fibres into the previous system, additional improvement is obtained. Also, the physical mechanism is reported as bridging features in SEM. Then, two parameters, epoxy curing temperature and printing interval time, are controlled respectively to find the optimal approach.

3.4.1 Effectiveness of epoxy adhesive to improve mortar interlayer bonding

The purpose of this section is to check the effectiveness of epoxy adhesive incorporated between two layers of mortar to enhance interlayer bonding. Four groups of specimens are compared and the details are shown in Table 3-3. In this section, the results of the three-point bending tests are presented to compare the tensile strength between the interlayer zones of different groups of specimens. Codes for the nominated specimen groups follow the rule for names of 'Ax-y'. 'A' means the specimen type, such as 'C' for control, 'P' for plain, 'E' for epoxy, and 'F' for fibre. 'x' means the 10-hour curing temperature one day before the tests,

such as ‘20’ for 20 degrees. ‘y’ means the printing interval time between two layers of mortar casting, such as ‘30’ for 30 minutes. For example, the group of specimens ‘E20-30’ means the specimens with epoxy incorporated between two layers of mortar with the printing interval time of 30 minutes, and the curing temperature of 20 degrees in the oven one day before the test.

Table 3-3 Details of specimens’ parameters for investigating the effectiveness of epoxy to improve interlayer bonding

Code	Description	Oven curing temperature	Printing interval time
I20-30	Control sample. Integrated mortar without layer structures.	20 degree	30 mins
P20-30	Control sample. Plain mortar in two layers.	20 degree	30 mins
E20-30	Epoxy adhesive incorporated between two layers of mortar.	20 degree	30 mins
E40-30	Epoxy adhesive incorporated between two layers of mortar.	40 degree	30 mins

Figure 3-4 shows the three-point bending test results for 7 days, 14 days and 28 days, for the four groups of specimens shown in Table 3-3.

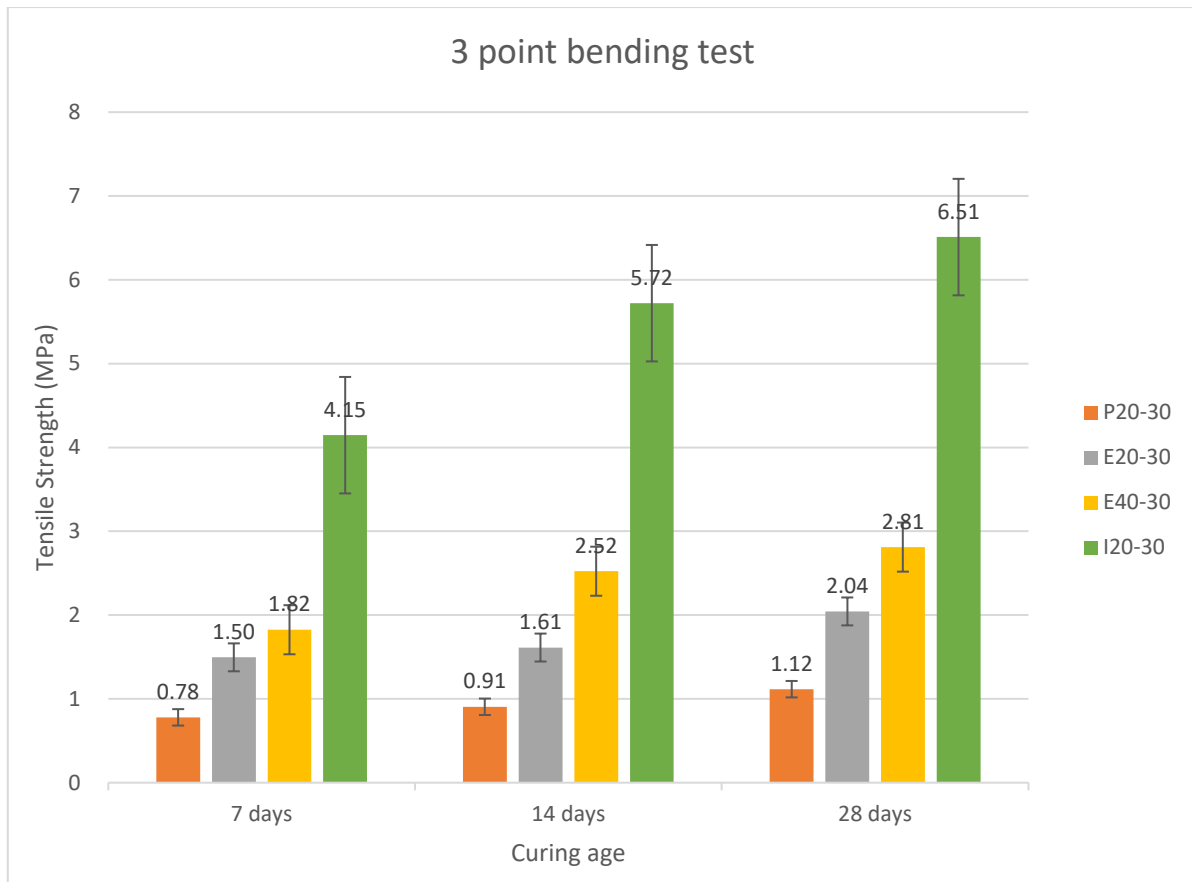


Figure 3-4 Three-point bending test results showing effectiveness of epoxy in improving interlayer bonding

For the group P20-30, it is shown that the tensile strength at 28 days is 1.12MPa, which is greater than the results reported in the literature (0.2-0.65 MPa). The reason is that in this experiment, mortar rather than concrete was used as the binder. Thus, the tensile strength measured is higher than the reports. However, in comparison with the other control sample I20-30 with integrated mortar as 6.51 MPa, P20-30 has only 17% of that strength. Once incorporated by epoxy between two layers of mortar, controlled under the same circumstance, the group E20-30 shows great improvement compared to P20-30. At 7 days, the tensile stress reaches 1.5 MPa with a 92.3% increase over the control sample. At 14 days, the tensile stress reaches 1.61 MPa with a 76.9% increase. At the 28 days test, the tensile stress has increased by 82.1%, to 2.04 MPa. However, this group of specimens was cured at 20 degrees before testing, without specific oven curing for the epoxy element. The optimal curing condition is 40

degrees for 3 hours. The group cured at 40 degrees in the oven for 10 hours before testing, E40-30, is compared with groups without the epoxy curing. At 7 days, the tensile stress of E40-30 reaches 1.82 MPa, increases of 133% and 21.3% over that of P20-30 and E20-30, respectively. At 14 days, the tensile stress increases to 2.52 MPa, which is 177% higher than P20-30 and 56.5% higher than E20-30. At 28 days, the tensile stress increases to 2.81 MPa, a 151% increase over that of P20-30 and a 37.7% increase over that of E20-30. Even compared with the control group I20-30, integrated mortar without a layer structure, the results are not bad. The tensile stress of the group E40-30 reaches 43.9%, 44.1% and 43.2% of the strength of control group I20-30 over 7 days, 14 days and 28 days, respectively. Clearly, the results show obvious increments between groups and between tests, and are reliable.

A coincidence found during the testing process is that the fracture always occurs between the first layer of mortar and the layer of epoxy. This finding indicates that the strength of the lower interface is always lower than that of the upper interface. Analysis of the process of the experiments reveals that the reason is related to the vibration. The vibration process causes a tiny amount of bleeding, with extra moisture on the surface of the first layer of mortar. The extra moisture leads to the decrease in strength.

Based on the mechanical strength test results, SEM characterisations are also performed on the fracture surfaces of both the epoxy side and the mortar side. Figure 3-5 shows the SEM pictures of group E40-30. On the epoxy side, see Figure 3-5(a) and (c), a large amount of cement hydrates adheres on the epoxy surface, and interlocking phenomena can be found between epoxy and cement hydrates. On the cement side, Figure 3-5(b) and (d) show that little epoxy can be found adhering to the cement. Hence, the failure in the interface between epoxy and cement occurs on cement side near the interface, and it appears to be in the interfacial transition zone (ITZ) of the cement.

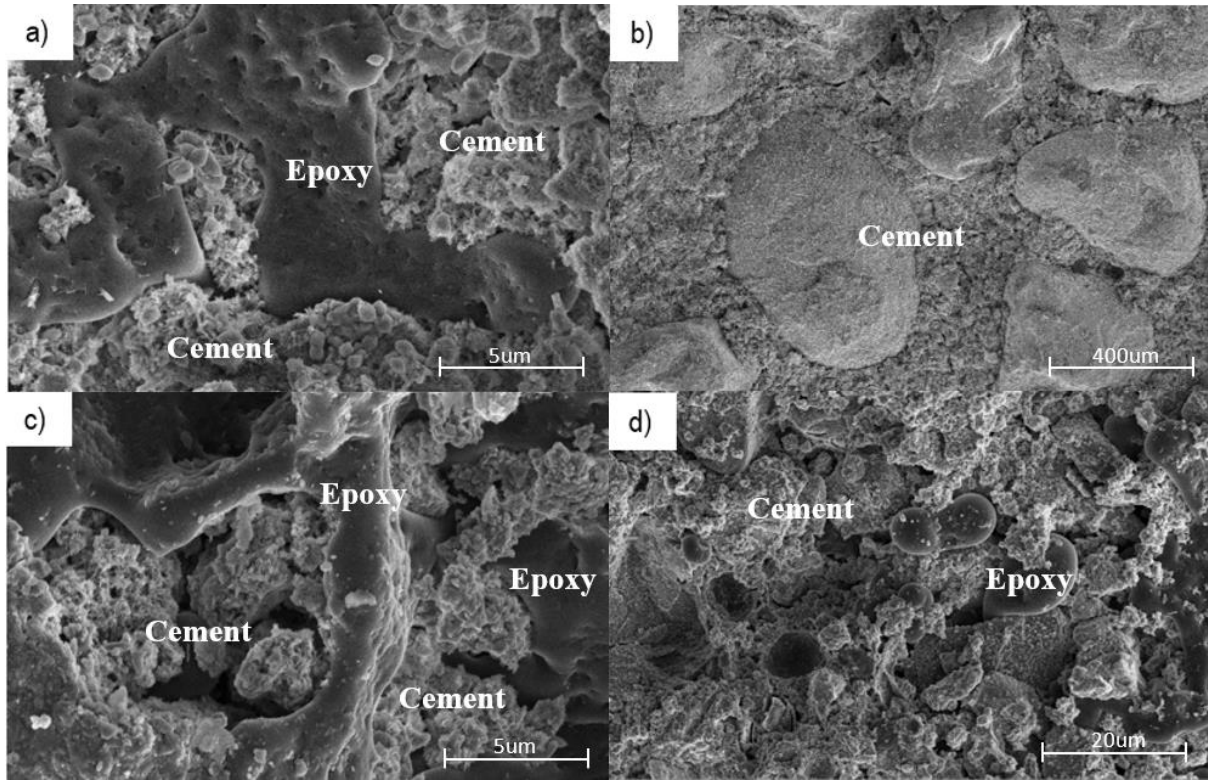


Figure 3-5 SEM for group E40-30: a) on epoxy side with CSH and interlocking phenomenon; b) on mortar side without epoxy features; c) on epoxy side with CSH and interlocking; and d) on mortar side with a few epoxy features

The following MD simulation section refers to declarations #3 and #4. For more validation and relating information, please refer to that papers.

Figure 3-6 demonstrates a general view of the model, the direction of imposed strain and the obtained stress-strain diagram for both the composite and the cement matrix, here modelled with CSH. Figure 3-6(a) shows the composite model, with epoxy resin confined by two layers of CSH. In Figure 3-6(b), the weakest direction of the model is depicted, where the tensile stress is inflicted, to directly assess the strength of the interlayer cohesion. The diagram shown in Figure 3-6(c) depicts the behaviour of the pristine CSH and the composite matrix under tensile stress. The first part of the diagram demonstrates both structures in the elastic region, with the CSH and the CSH-epoxy resin composites peaking at 4.13 GPa and 4.73 GPa, in 7.5% and 10% strains, respectively. These figures indicate that the addition of epoxy resin between the CSH layers strengthens the structure, extending the cement elastic region by a

third. Taking a more in-depth look at the diagram, it is clear that in the later phases, both structures show similar behaviour, gradually degrading in terms of resistance, with the interlayer region slowly beginning to dissent at the weakest plane; with CSH layers separating in higher strains in the pristine specimen, whereas in the CSH-epoxy resin specimen, the separation occurs in the intermediate region between the CSH and epoxy resin.

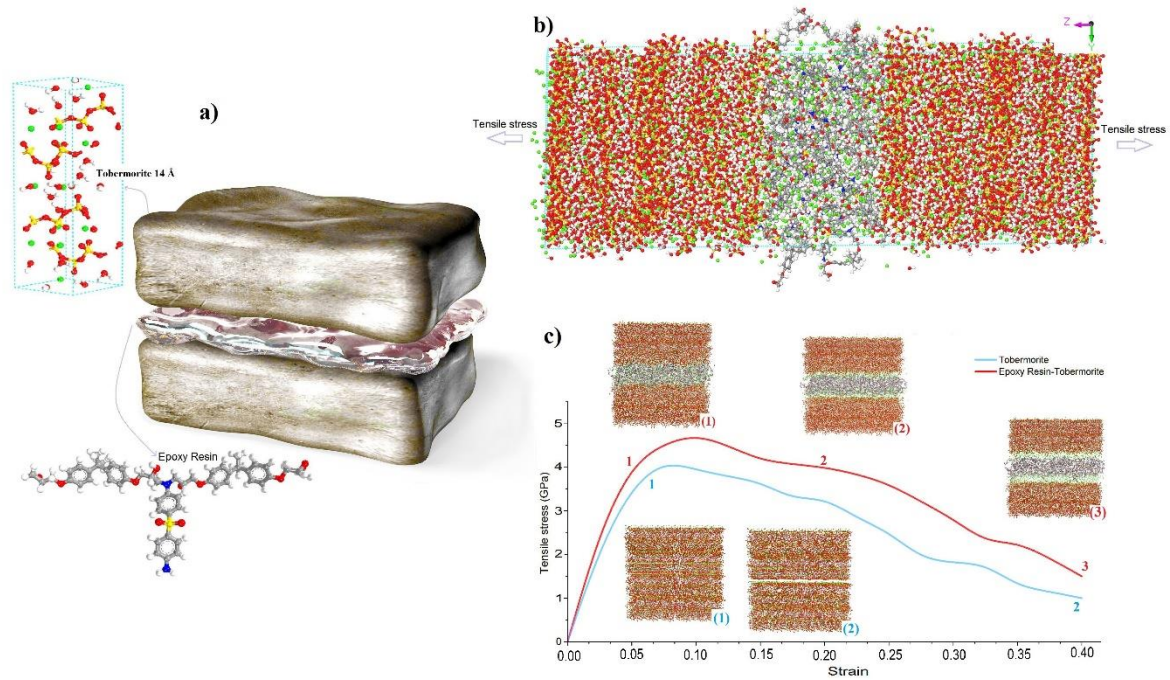


Figure 3-6 (a) Model of the CSH-epoxy resin composite; (b) direction of imposed strain on the model; (c) Stress-strain diagram of pristine CSH and CSH-epoxy resin composite

Further study explores the use of a new type of sulphur-carbon polymer to provide a dependable bonding material between adjunct layers of 3D printed mortar. Figure 3-7(b) shows the MD model at two different stages: first at zero strain and secondly at 12% strain. The second strain value shown in Figure 3-7(b) is where the maximum stress is tolerated, and the expansion is more significant in the CSH layers than in the BCS polymer. Shear strength is a more practical factor in 3D printing; as a matter of fact, the shear strength and flexibility of a structure are directly related to the feasibility of the 3D printing industry. Figure 3-7(c) shows the interfacial shear stress for each model. CSH1, the monolith CSH model, bears about twice as

much interfacial shear stress than the pure CSH-CSH model. It is followed closely by the BCS-enhanced model, the interfacial shear strength of which is 17% less than that of the CSH1 model and 50% higher than that of the CSH2 model. To gain better understanding of the shear failure process, the BCS-enhanced interface is assessed in the atomic scale. Considering shear strength in the interface between CSH layers, the model shown in Figure 3-7(d) is a good measure of crack propagation in the structure. Cracks begin at the interface between the BCS polymer and the CSH layer where the shear force is imposed. However, Figure 3-7(d) also demonstrates the cohesion established between the BCS polymer and the CSH layers even under large deformations.

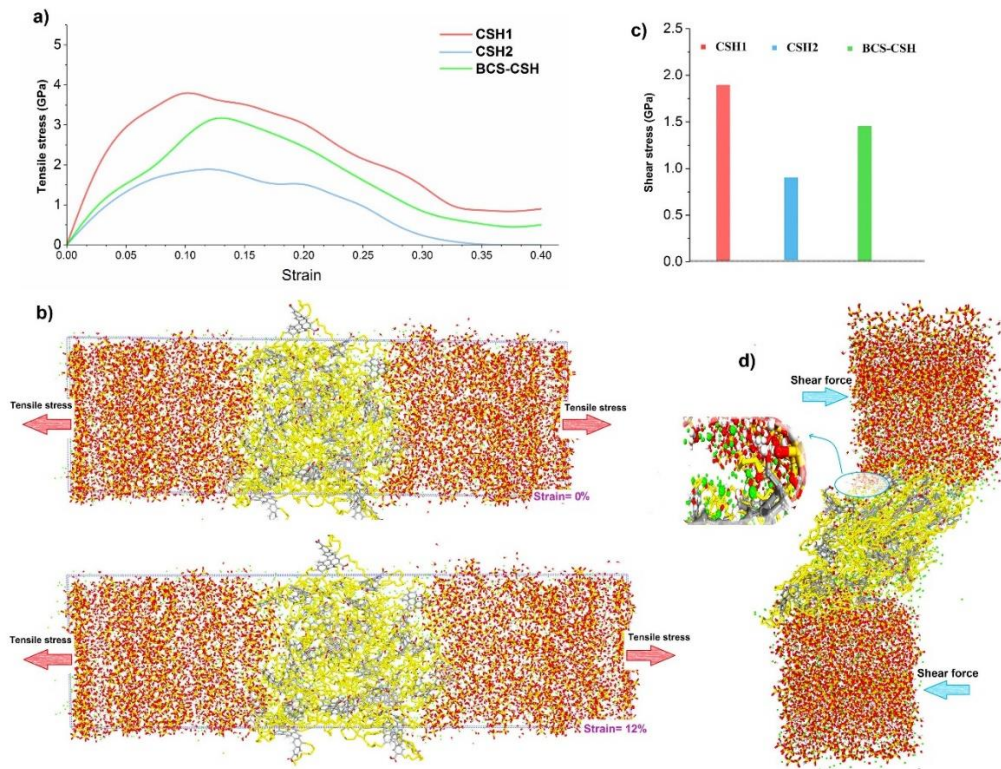


Figure 3-7 a) Stress-strain behaviour of printed mortar, BCS polymer enhanced printed mortar; b) Modelled interaction zone under tensile strain c) Interfacial shear strength for pristine printed mortar, BCS-enhanced printed mortar and seamless mortar specimen d) Modelled interaction zone under shear force

3.4.2 Enhancement of mortar-epoxy system by PVA fibres

In section 3.4.1 it was stated that, in the group E40-30, the ITZ is considered to be the weakness in this system when the interlayer bonding is enhanced by epoxy. Hence, PVA fibre was incorporated into the system to enhance the ITZ, in the sample group designated F40-30. Also, control groups of integrated and layered mortar were created, named I20-30 and P20-30, using the same composite and cured at 20 degrees (normal field condition) in the 10 hours before the test results were compared. The diameter of the PVA fibre is 100 micro metres and length is 13mm. Table 3-4 shows the detailed parameters of the compared specimen groups.

Table 3-4 Parameters of specimens used to investigate the effectiveness of PVA fibre to improve interlayer bonding

Code	Description	Oven curing temperature	Printing interval time
I20-30	Control sample. Integrated mortar without layer structures.	20 degree	30 mins
P20-30	Control sample. Plain mortar in two layers.	20 degree	30 mins
E40-30	Epoxy adhesive incorporated between two layers of mortar.	40 degree	30 mins
F40-30	Epoxy with PVA fibres incorporated between two layers of mortar.	40 degree	30 mins

Figure 3-8 shows the three-point bending test results for 7 days, 14 days and 28 days for the four groups of specimens shown in Table 3-4.

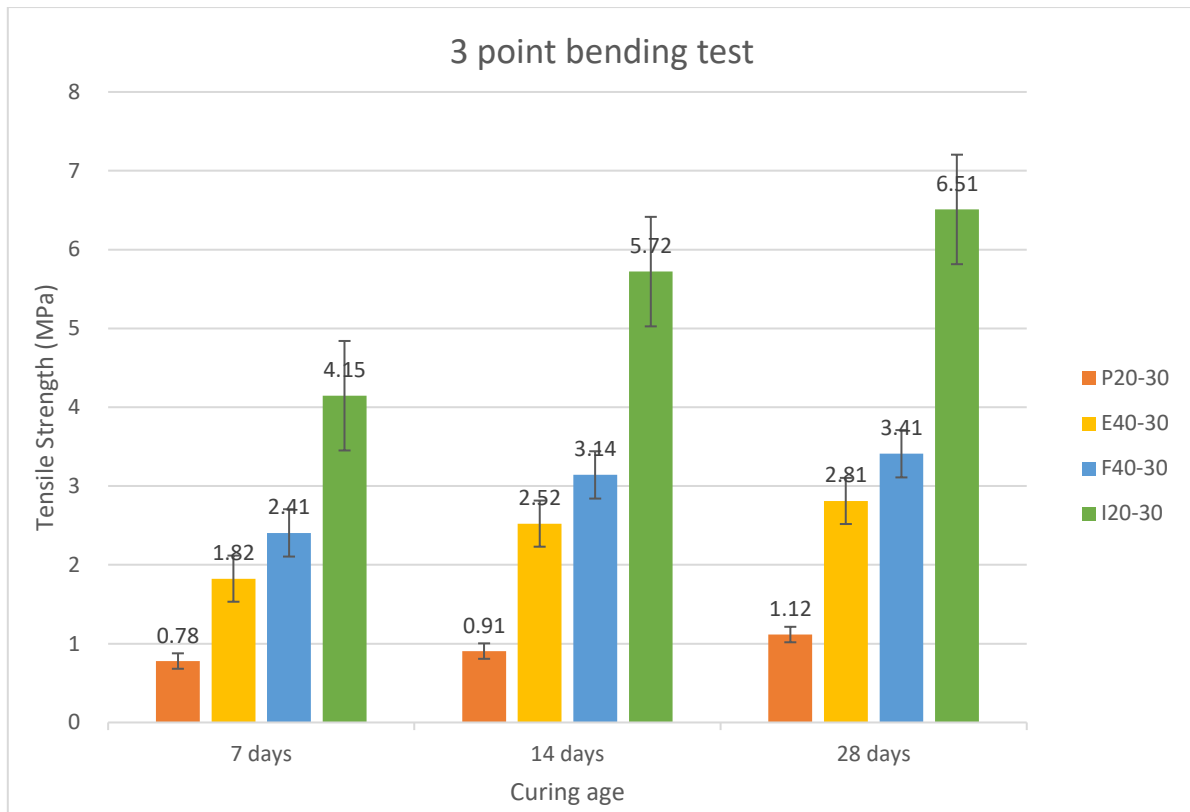


Figure 3-8 Three-point bending test results showing the effectiveness of PVA fibres in improving the previous approach.

Clearly, the effectiveness of PVA fibres is superior compared to the results without the incorporation of fibre. After 7 days, the tensile stress in the E40-30 group increases by 32.4% compared to that in the F40-30 group. After 14 days, it increases by 24.6%. After 28 days, it again increases by 21.4%. These results indicate marked improvement produced by the introduction of PVA fibres. Moreover, when the results of the F40-30 group are compared with those of the I20-30 control group, the tensile stress of F40-30 increases by 58.1%, 54.9% and 52.4% compared to that of the control group for 7 days, 14 days and 28 days, respectively. It can be concluded that this type of material, enhanced by epoxy and PVA fibres, is suitable for 3D printing mortar constructions. To a certain extent, the PVA fibre enhancement provides enough strength for 3D printed structures, and it can be an alternative method for addressing the problem of low interlayer bonding.

When the mechanism of improvement by the incorporation of PVA fibres is considered, SEM characterisation can provide evidence. Figure 3-9 shows SEM pictures for the group of specimens F40-30. In Figure 3-9(a), a hole in the mortar can be clearly seen, with the same diameter as that of the PVA fibres. It is the evidence of fibre pull-out. From Figure 3-9(b), a fibre incorporated into the system is broken in mortar. Fibre pull-out is evident in Figure 3-9(c). In Figure 3-9(d), both pull-out and the breaking phenomenon can be found.

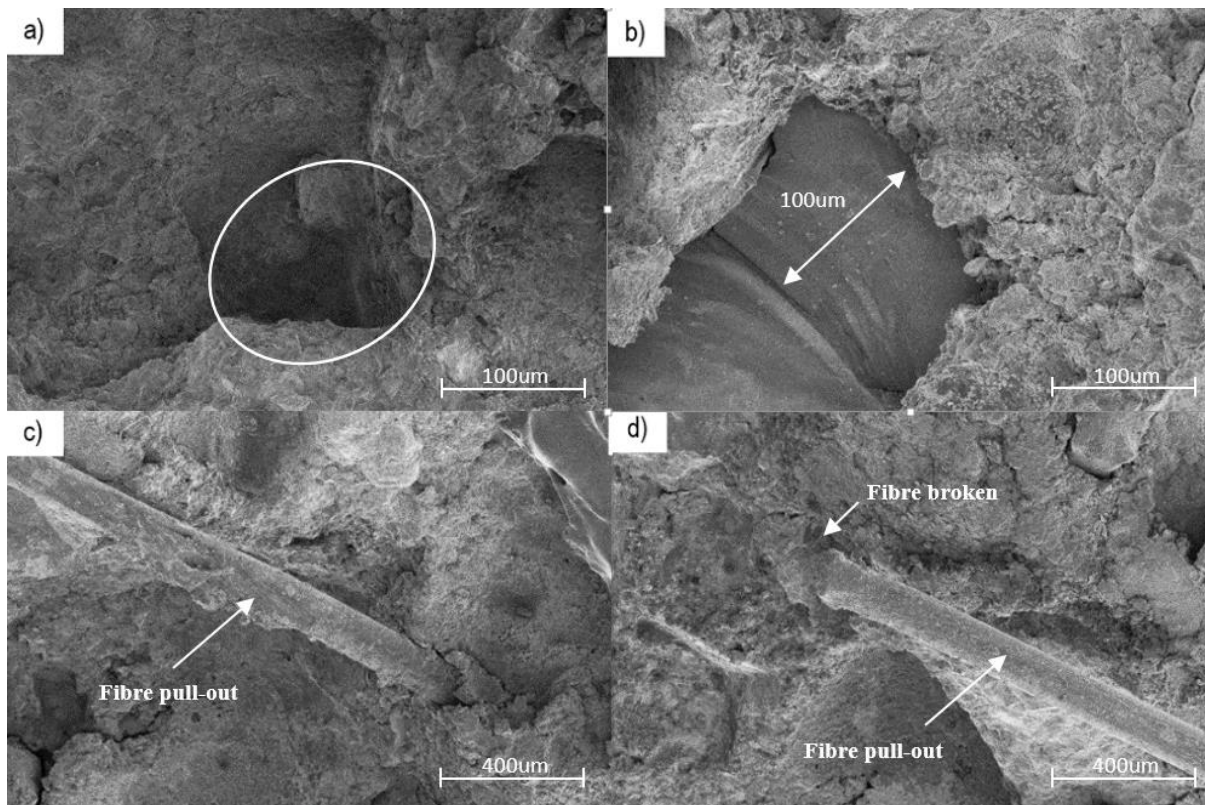


Figure 3-9 SEM for group F40-30: a) hole left by fibre pull-out; b) fibre broken in mortar; c) pull-out phenomenon; and d) fibre pull-out and broken.

3.4.3 The influence of oven curing temperature on epoxy-mortar and epoxy-fibre-mortar system

In section 3.4.1, the strength difference between E20-30 and E40-30 was found, indicating the influence of oven curing (mainly for epoxy) in the final strength of specimens. In this section, the influence of oven curing temperature is investigated as a parameter. Four groups of curing

temperatures are chosen, 20 degrees, 30 degrees, 40 degrees and 60 degrees. The printing interval time is kept at 30 mins. Table 3-5 shows the detailed parameters of the compared specimen groups, and Figure 3-10, Figure 3-11 and Figure 3-12 illustrate the three-point bending test results for 7 days, 14 days and 28 days, respectively.

Table 3-5 Details of specimens' parameters for investigating the influence of epoxy curing temperature on interlayer bonding in mortar-epoxy and mortar-epoxy-PVA systems

Code	Description	Oven curing temperature	Printing interval time
E20-30	Epoxy adhesive incorporated between two layers of mortar	20 degrees	30 mins
F20-30	Epoxy with PVA fibres incorporated between two layers of mortar	20 degrees	30 mins
E30-30	Epoxy adhesive incorporated between two layers of mortar	30 degrees	30 mins
F30-30	Epoxy with PVA fibres incorporated between two layers of mortar	30 degrees	30 mins
E40-30	Epoxy adhesive incorporated between two layers of mortar	40 degrees	30 mins
F40-30	Epoxy with PVA fibres incorporated between two layers of mortar	40 degrees	30 mins
E60-30	Epoxy adhesive incorporated between two layers of mortar	60 degrees	30 mins
F60-30	Epoxy with PVA fibres incorporated between two layers of mortar	60 degrees	30 mins

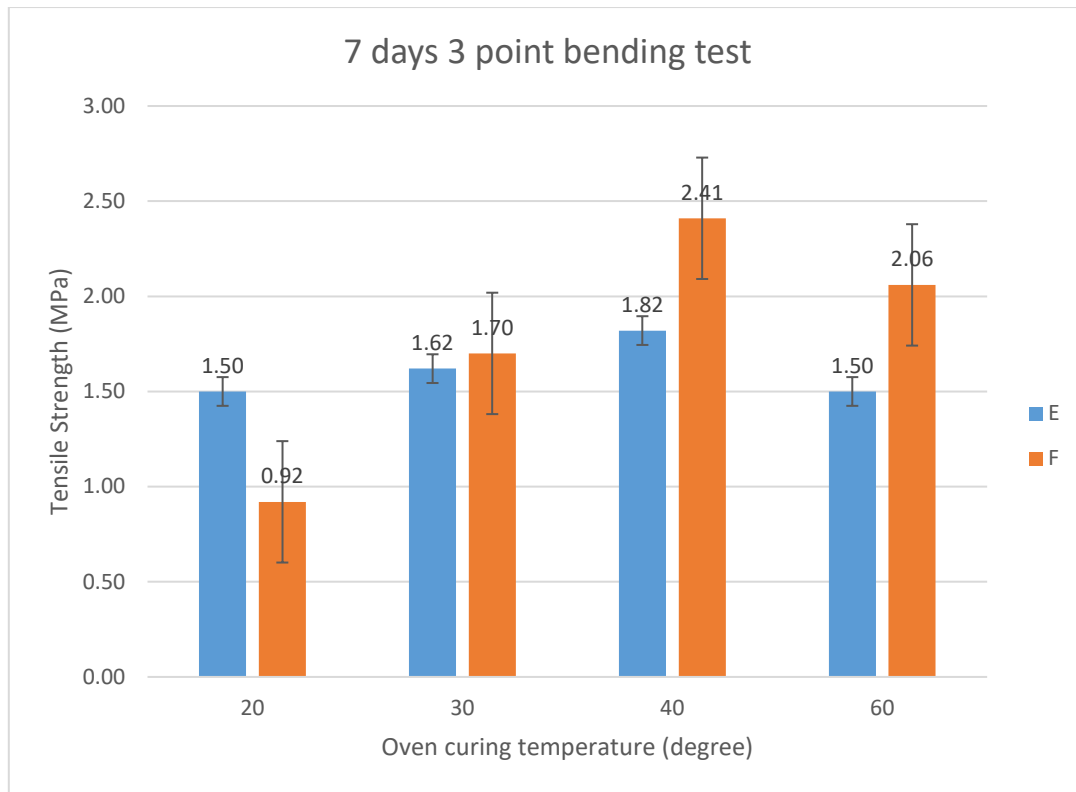


Figure 3-10 7 days three-point bending test results to determine the influence of oven curing temperature

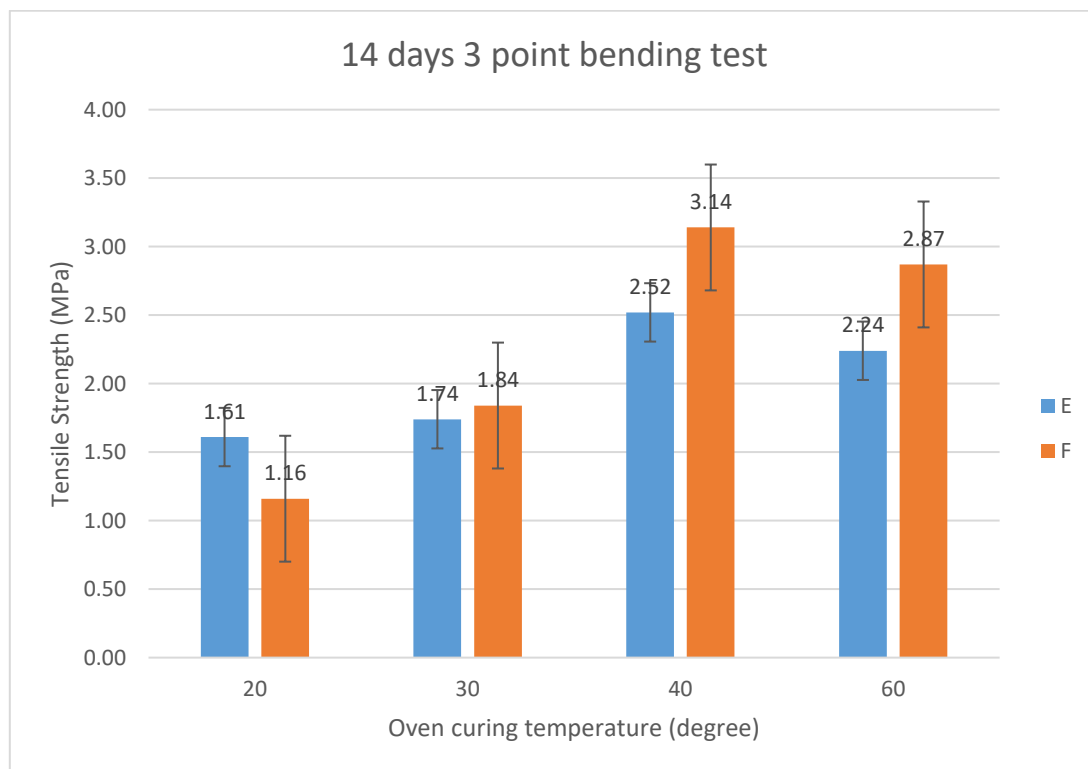


Figure 3-11 14 days three-point bending test results to determine the influence of oven curing temperature

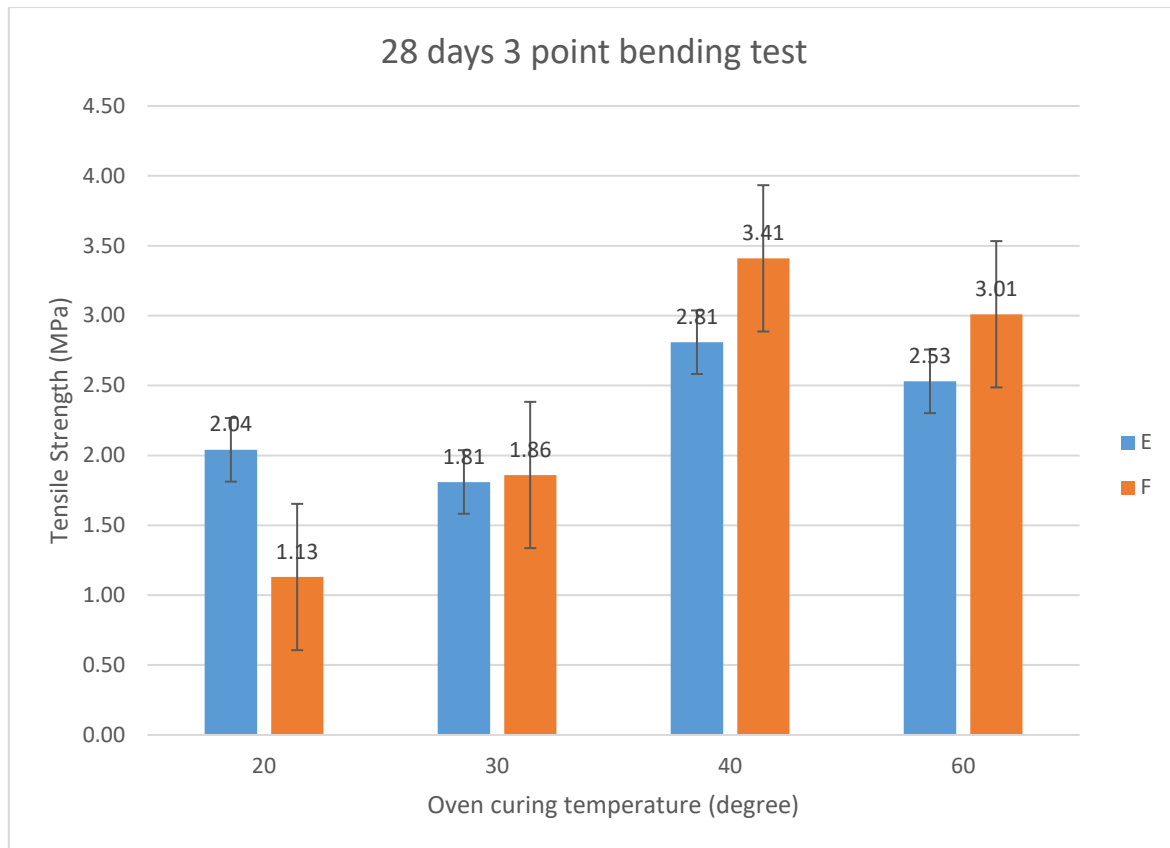


Figure 3-12 28 days three-point bending test results to determine the influence of oven curing temperature

From the results shown in these three figures, it is evident that, except for the groups E20-30 and F20-30, groups containing PVA fibres always display higher tensile stress than groups without PVA fibres. In particular, in groups with the oven curing temperatures of 40 and 60 degrees, the difference is much more apparent. Globally, the groups with the oven curing temperature of 40 degrees show the greatest strength. The groups with the oven curing temperature of 60 degrees have the second highest strength. It can be concluded that the curing temperature for epoxy plays an important role in influencing the tensile strength of 3D printed mortar, both with epoxy and with epoxy introduced by PVA fibres. One exception is for specimens with 20 degrees epoxy curing: there is a marked decrease in tensile strength in the F20-30 group compared to the E20-30 group. On the basis of the data presented, it is hypothesised that PVA fibres play both positive and negative roles in improving interlayer

bonding. The positive effect comes from mechanical enhancement, such as bridging. However, the chemical bond between CSH and PVA fibres is not strong. Once large amount of PVA is incorporated into the system, weak bonding results in a decrease in strength. Hence, in the group F20-30, the negative effect dominates the result. In the group F30-30, both sides contribute, thus there is only a small difference between E30-30 and F30-30. In the groups F40-30 and F60-30, a positive effect predominates.

In conclusion, the optimal curing condition for both approaches is 40 degrees for 10 hours, which is the same as the recommendation for the epoxy itself. Curing benefits not only the epoxy strength, but also the interface.

3.4.4 The influence of printing interval time on epoxy-mortar and epoxy-fibre-mortar system

Apart from curing temperature, another important parameter influencing the interlayer bonding strength is printing interval time, which is the time delay between two layers of mortar casting. In this case, the groups E40-30 and F40-30 become the reference for comparison by changing the printing interval time from 15 mins to 2 hours. Table 3-6 shows the detailed parameters for specimens E40-15, F40-15, E40-30, F40-30, E40-60, F40-60, E40-120, and F40-120. Figure 3-13, Figure 3-14 and Figure 3-15 illustrate the three-point bending test results for 7 days, 14 days and 28 days, respectively.

Table 3-6 Details of specimens' parameters for investigating the influence of printing interval time on interlayer bonding of mortar-epoxy and mortar-epoxy-PVA systems

Code	Description	Oven curing temperature	Printing interval time
E40-15	Epoxy adhesive incorporated between two layers of mortar.	40 degrees	15 mins
F40-15	Epoxy with PVA fibres incorporated between two layers of mortar.	40 degrees	15 mins
E40-30	Epoxy adhesive incorporated between two layers of mortar.	40 degrees	30 mins
F40-30	Epoxy with PVA fibres incorporated between two layers of mortar.	40 degrees	30 mins
E60-30	Epoxy adhesive incorporated between two layers of mortar.	40 degrees	60 mins
F60-30	Epoxy with PVA fibres incorporated between two layers of mortar.	40 degrees	60 mins
E120-30	Epoxy adhesive incorporated between two layers of mortar.	40 degrees	120 mins
F120-30	Epoxy with PVA fibres incorporated between two layers of mortar.	40 degrees	120 mins

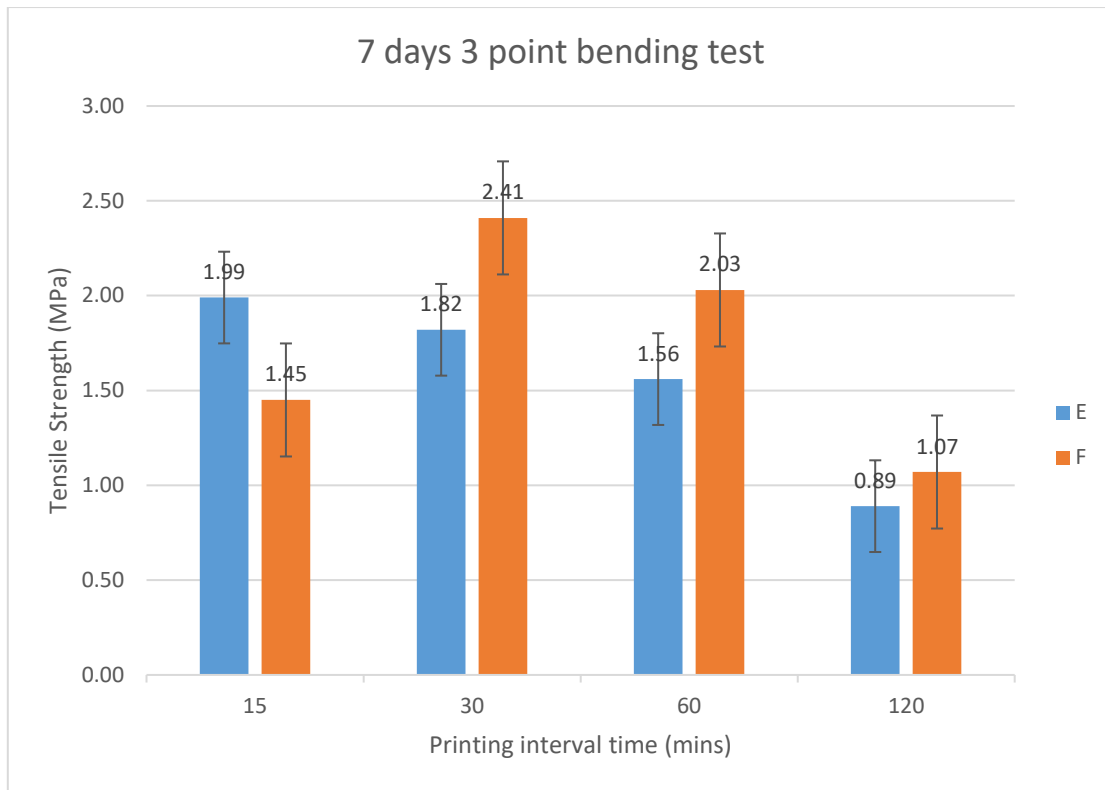


Figure 3-13 7 days three-point bending test results to determine the influence of printing interval time.

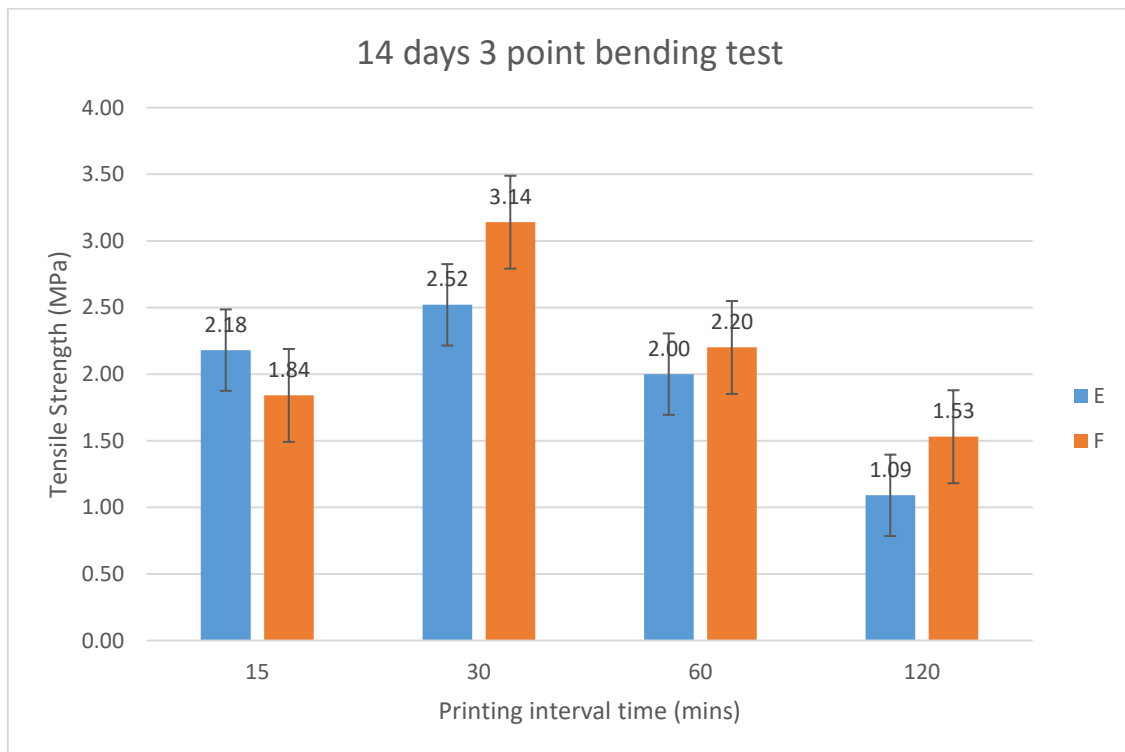


Figure 3-14 14 days three-point bending test results to determine the influence of printing interval time.

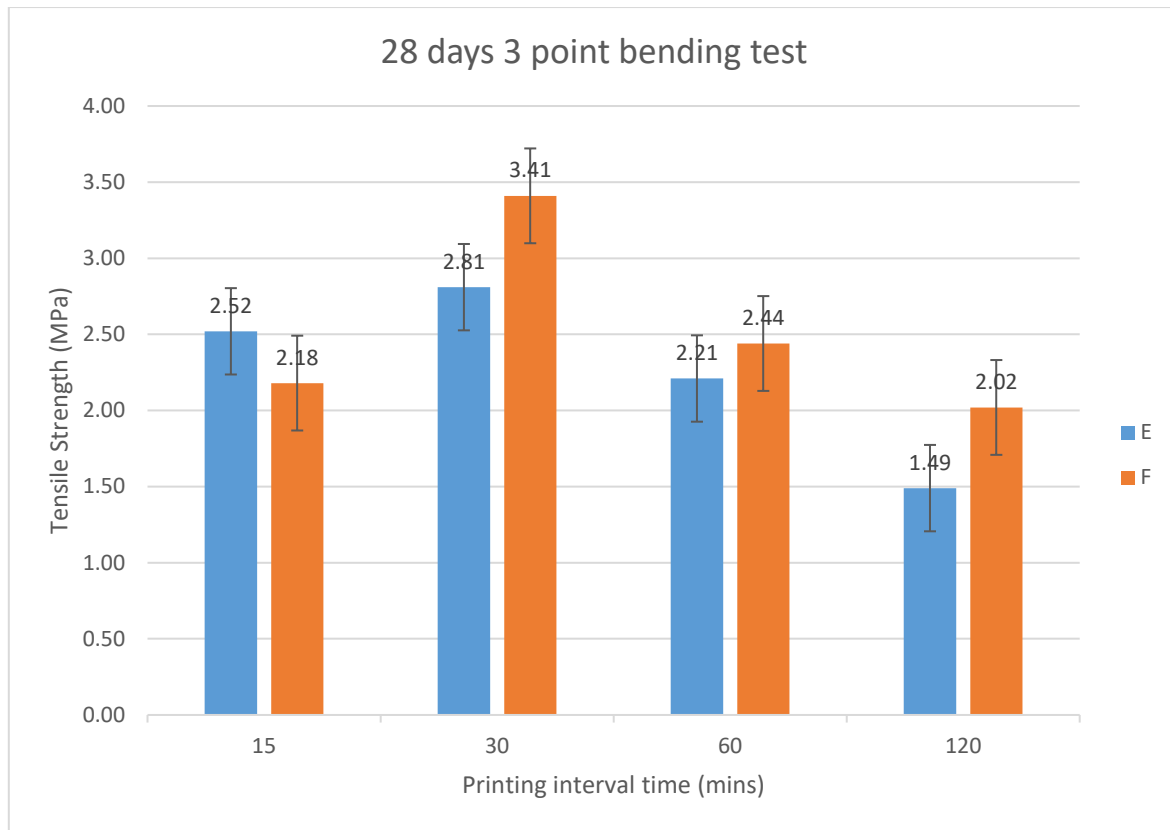


Figure 3-15 28 days three-point bending test results to determine the influence of printing interval time

For the epoxy-mortar system specimen groups E40-15, E40-30, E40-60 and E40-120, it is clear that the interlayer bonding strength decreases with increasing the printing interval time for 7 days. However, for the longer terms of 14 days and 28 days, the strength of E40-15 is lower than that of E40-30. Thus the optimal printing interval time for the long term for the epoxy group is 30 mins. The group E40-15 has the highest interlayer bonding strength within the E groups, of 2.74 MPa. However, that is still lower than the interlayer bonding strength of the group F40-30, of 3.14 MPa. For the epoxy-PVA-mortar system, specimen groups F40-15, F40-30, F40-30 and F40-120, a similar tendency is found, except in the group F40-15, which shows lower strength than that of the group E40-15. The reason is supposed to be the presence of high moisture content due to bleeding affecting the bonding between PVA fibres and mortar. In summary, the group F40-30 has the highest tensile stress of 3.41 MPa in 28 days, and 30 minutes printing interval time is the optimal level of this parameter for both approaches.

3.5 Conclusions

With the advances in the field of construction, numerous methods have been proposed to introduce automation to the industry. 3D printing is one such method and it is gaining prominence more quickly than the others. The problem with the 3D printed mortar lies within the interaction region, where the layers of extruded mortar interact. This region shows insufficient strength, causing the layers to be easily separated by a moderate shear force.

In this study, two enhancement approaches were proposed and were investigated by an experimental program, SEM characterisation and MD simulation. One approach was the introduction of a thin layer of epoxy adhesive between layers of mortar. The second approach was incorporation of PVA fibres in the epoxy-mortar system. Apart from the epoxy adhesive, a carbon and sulphur polymer was also investigated by MD simulation. The following conclusions were drawn.

1. With the first approach, the epoxy adhesive helped improve the interlayer bonding, with specific curing condition for epoxy, by more than 150% at 28 days. This result indicates the effectiveness of epoxy in enhancing the interlayer bonding strength of 3D printed mortar. SEM characterisation explained the reason in the physical aspect, as interlocking between epoxy and CSH was found. Moreover, chemical bonds between them were also found by MD simulation, providing strong evidence of the significant strength improvement. A new type of BCS polymer was also investigated by MD simulation, and proved to be effective.
2. Incorporating PVA fibres into the abovementioned system further improved interlayer bonding strength. With 3 vol.% PVA fibres, the specimens showed a 21% increase compared to those without PVA fibres. The improvement achieved compared to the control integrated mortar reached 52.4%. This result indicates that the approach has

potential for application in concrete construction. SEM characterisation explained the additional improvement in the physical aspect, by the bridging mechanism of PVA fibres between epoxy and mortar.

3. The curing temperature for the epoxy influenced the interlayer bonding strength. The curing temperature affected not only the epoxy strength itself, but also the interface between epoxy and mortar. For both approaches, 40 degrees was recommended as the optimal curing temperature. Between the curing temperatures of 30 degrees and 60 degrees, the second approach showed better performance.
4. Printing interval time also affected the interlayer bonding strength. For long-term durability, the 30 minutes printing interval time is recommended, having the highest tensile strength of both groups with epoxy and epoxy with PVA fibres. The reason why the 15 minutes time delay shows lower strength is hypothesised to be attributable to bleeding water. Thus, the water/binder ratio can influence the final bonding strength of the interlayer.

Chapter 4. Study of the effectiveness of GO in reducing alkali-silica reaction (ASR) in 3D printed mortar

4.1 Introduction

This chapter refers to declaration #5.

The approaches in Chapter 3 provide insights for improving the low interlayer bonding strength of 3D printed mortar. Even if mechanical issues are improved, however, there are some durability problems. Usually, mortar with a high proportion of sand is used for 3D printing technology, rather than traditional concrete of coarse aggregates. In 3D printed mortar, due to the high content of sand, which is an ASR reactive aggregate, ASR can lead to serious durability problems in the long term.

Internationally, durability performance is one of the key factors which affect the long-term reliability of concrete structures. Inadequate durability often shortens their entire projected design lifetime. For example, a large number of concrete buildings and bridges in China have been rendered unserviceable within just half of their design life span (i.e., 20~30 years). Improving the durability properties of concretes using GO provides a promising solution for the cracking, corrosion and durability problems in concrete.

As a graphene derivative, GO consists of a hexagonal carbon network bearing hydroxyl, epoxide, carboxyl and carbonyl functional groups. These oxygen-containing functional groups render GO sheets hydrophilic and highly dispersible in water (Qiu, Yang et al. 2010). The various functional groups, coupled with the large surface area, create a highly reactive GO nanomaterial. Therefore, GO has emerged as a potential nano-reinforcement due to its

contribution to improvement in solubility, ease of production and positive interaction with cement matrix. Detailed information regarding the fabrication and characterisation of GO cement can be found in the recent US patent (Pan, W.H. Duan et al. 2012) filed by CI Duan. The results show that GO sheets can significantly improve compressive strength, flexural strength and fracture toughness, as well as the pores of cement.

ASR is a kind of reaction between certain kinds of silica which occasionally exist in large quantities in aggregates and some hydroxyl ions in pore water of concrete (Hobbs 1986). In 1940s, the presence of ASR was considered a harmful process in the components of concrete. It was found very early that, considering exposure to natural environmental conditions, cement and aggregates are more liable to this type of concrete deterioration, which is caused by the opaline aggregates and high-alkali cement used in concrete (Swamy 2002). Some typical features of ASR in concrete structures are expansion, cracking and misalignment. However, none of these features can be considered to be uniquely the cause of ASR (Thomas 2011). In this project, GO was indicated to be effective to improve ASR problem by refining the mortar pore structures.

4.2 Experimental program

4.2.1 Expansion testing of ASR mortar

This test is used to determine the dosage of GO and dune sand needed to reduce the mortar bar expansion below the innocuous threshold of 0.1% (ASTM C441 2012). ASTM C150 type I Portland cement is used. GO and dune sand are used at different replacement levels (mass based) to evaluate their efficiency in controlling ASR. Pyrex glass as a type of ASR-reactive aggregate is used to accelerate the progress of the experiment (ASTM C1567 2012). To assess the influence of GO on ASR, accelerated mortar bar (25mm*25mm*280mm) tests are used.

During the test, expansion of samples is monitored. Nine samples containing different amounts of Pyrex glass (0, 50% and 100% replacement) and GO (0,0.02% and 0.04%) are prepared, three samples for each kind. The mix design is as shown in Table 4-1. The proportion of dry materials for the test mortar is 1 part cementitious materials to 2.25 parts of the combination of Pyrex glass and sand by mass. All mortars are prepared with water-to-cementitious materials ratio (w/cm) = 0.47, and the sand and Pyrex glass used have gradation in the range of 4.75 mm–150µm in accordance with ASTM C1567 and C441.

Table 4-1 Mix design of expansion test of ASR mortar

Mix Design(we assume the mass of cement is 1)						
Number of different kinds	Portland cement	Water	Sand	Pyrex Glass	Water reducer	GO
A1	1	0.47	2.25	0	0.01	0
A2	1	0.47	2.25	0	0.01	0.0002
A3	1	0.47	2.25	0	0.01	0.0004
B1	1	0.47	1.125	1.125	0.01	0
B2	1	0.47	1.125	1.125	0.01	0.0002
B3	1	0.47	1.125	1.125	0.01	0.0004
C1	1	0.47	1.6875	0.5625	0.01	0
C2	1	0.47	1.6875	0.5625	0.01	0.0002
C3	1	0.47	1.6875	0.5625	0.01	0.0004

For the initial storage and reading, each mould was placed in a moist cabinet or room immediately after the moulds were filled. The specimens remained in the moulds for 24±2 h. Specimens were then removed from the moulds and, while being protected against loss of moisture, were properly identified and an initial comparator reading was made (ASTM C441 2012). The initial and all subsequent readings were recorded to the nearest 0.002 mm. All specimens were covered with sufficient tap water to totally immerse them. The containers were sealed and placed in an oven or water bath at 80.0±2 degrees for a period of 24 h ± 2 h. For

subsequent storage and measurement, subsequent comparator readings were made at 1, 3, 5, 7, 10, 14, 21 and 28 days, at approximately the same time each day. The mass of each specimen was measured while the length was tested.

4.2.2 Mechanical testing of ASR mortar

To examine the effect of GO on the flexural strength (i.e., modulus of rupture) of the mortars, 40mm*40mm*160mm prisms were tested in 3-point bending (Glasser and Kataoka 1981). The specimens were prepared and cured following the procedure of GB/T17671-1999. The mix design of this experiment was the same as that for ASTM C1567 already presented. The composition of the 9 sample groups was the same as that of expansion test. Thus there were 9 groups, with 27 samples in total. Each sample was placed in a curing room immediately after the moulds had been filled. The specimens remained in the moulds for 24 ± 2 h. Then the prisms were removed from the moulds. The prisms were tested after 28 days. For the equipment used to test flexural strength, 50kN Instron was used. The distance between the left point and right point was 110mm. The rate of loading was 0.04 mm/min and the testing took almost 20 min for each sample.

4.2.3 SEM characterisation

To understand the mechanism of the limiting effect of the GO on the expansion of ASR mortar, SEM was used to observe the micro features of the nine groups of samples.

4.3 Results and discussion

4.3.1 Expansion test

The length change of the prisms was calculated as a percentage at a particular age, using the expression:

$$\text{Percentage increase in length (\%)} = \frac{L_n - L_0}{L_0} \times 100\%$$

where L_n is the length measurement at n days, L_0 is the initial length (Glasser and Kataoka 1981).

Figure 4-1 shows the expansion test results. Group A samples contain no Pyrex glass. Thus, the expansion rate of the samples is the lowest among the three groups. But the effect of GO on controlling the expansion from the first day is evident. Sample A1 contains no GO and sample A2 contains 0.02% GO. There is almost no difference during the first 21 days, meaning that the amount of GO (0.02%) is insufficient to control the expansion from the beginning of reaction. But from the 21st day, the expansion of A2 is clearly slower than that of A1, indicating the limiting effect of GO on expansion. Group A3 contains 0.04% GO. It is clear that the limited expansion of samples containing 0.04% GO occurs at the beginning of curing, meaning that 0.04% GO is more effective in controlling expansion at the early age of the mortar. In accordance with ASTM C441, the test period should be 14 days. But in this experiment the time was extended to 28 days, which, it seems, was still not enough. Comparison of groups A2 and A3 shows that from the 21st to the 28th day, the expansion of the two groups was becoming similar, which might indicate that, over a longer period, the difference between 0.02% GO and 0.04% GO might be small, or could even be ignored. If so, it would not be necessary to add as much GO as 0.04%.

In group B, 50% Pyrex glass was used to replace common sand, to accelerate the reaction between aggregate and alkali. It is evident that the expansion in the three samples, which contain different GO ratios, is almost the same during the early stage. But from the 7th day, the expansion rate varies. In particular, after the 21st day, obvious expansion difference between the sample with 0.02% GO and with 0.04% GO appears. As is evident, the reactivity in group B is much faster than that in group A, due to the use of Pyrex glass.

In group C, regulation is evident of the effect of GO on controlling expansion. Over the first 7 days, the expansion of the three kinds of samples is almost the same, but after the 7th day, the effect of GO appears. It is also clear that the samples with 0.04% GO show less expansion than those with 0.02% GO, indicating that the amount of GO also contributes to the control of expansion.

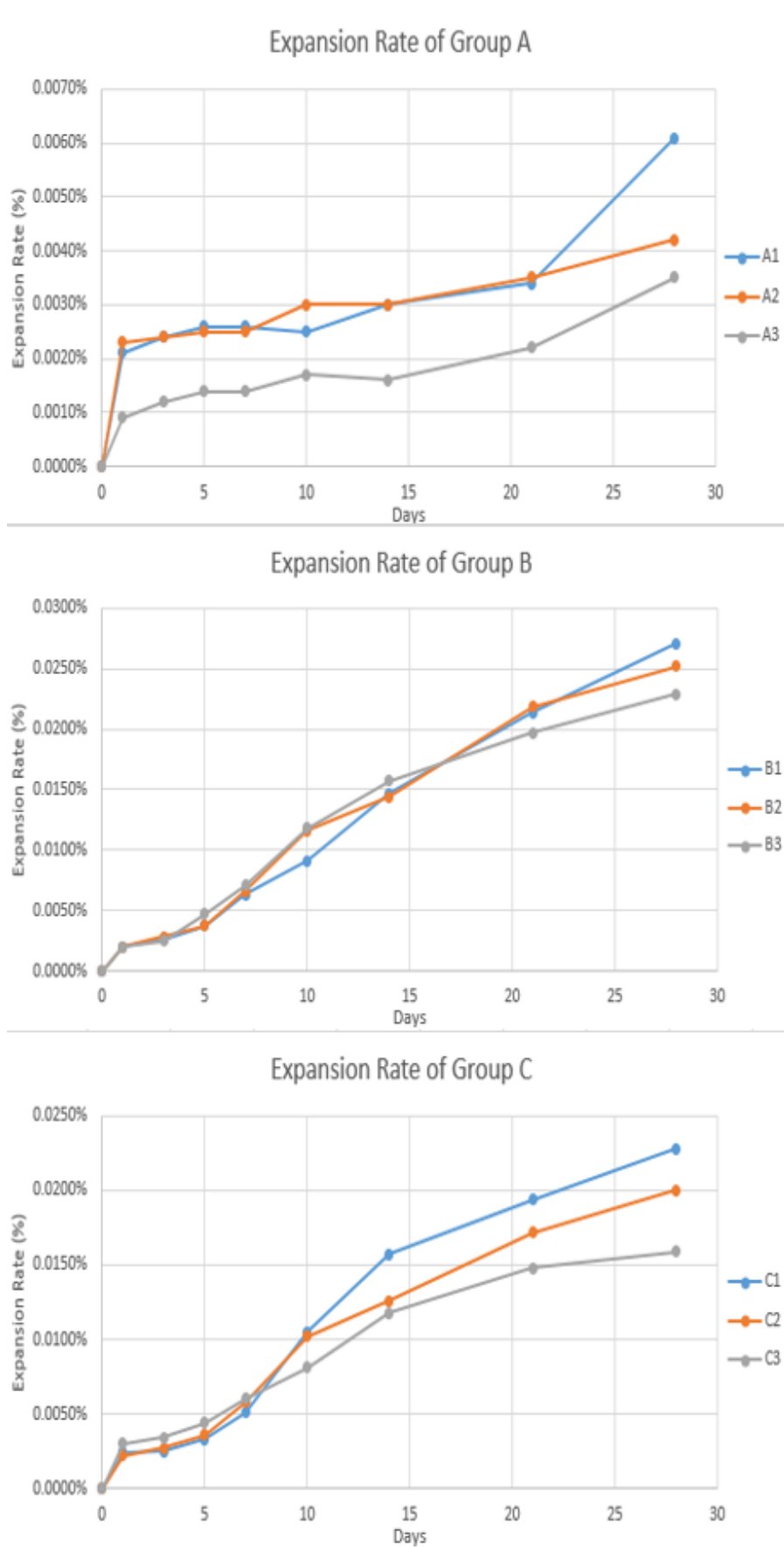


Figure 4-1 Mortar bar test results of expansion rates for three groups.

4.3.2 Mechanical test

Figure 4-2 shows the flexural test results. Group A1 contains no GO, group A2 contains 0.02% GO and group A3 contains 0.04% GO. None of the samples contains Pyrex glass. The beneficial effect of the GO on flexural strength is obvious. The strength of A2 increases by 5.56% compared with that of A1, whereas the strength of A3 increases by 24.17% compared with that of A1. This is an amazing increase in flexural strength with the use of a very small amount of GO.

Compared with the improvement in group A, the regulation of flexural strength in group B is less apparent. But it is still possible to observe the increase by comparing B3 and B1. The flexural strength of B2 does not increase, which may due to measuring error. By comparing A1, B1, A2, B2, A3 and B3, it is evident that the samples containing Pyrex glass are more fragile than those in group A, which may be the result of the more acute reaction between glass and alkali. More cracks form with the more reactive aggregates, directly causing the decrease in flexural strength.

The regulation of flexural strength in group C is almost the same as that in group B. There is only a 3.7% increase in flexural strength from group C1 to C3. From comparisons of groups B and C, it is evident that the flexural strength has decreased.

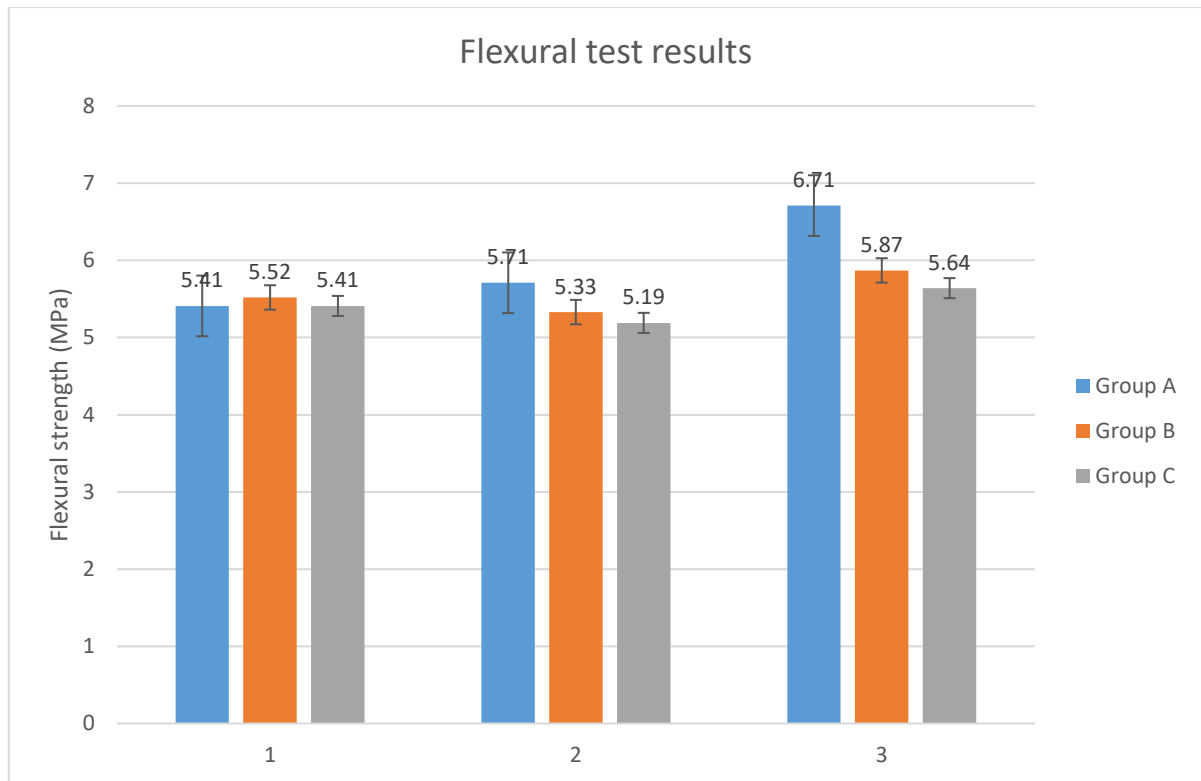


Figure 4-2 Flexural test results.

4.3.3 SEM characterisation

SEM characterisation has been conducted to investigate this project and try to find some cracks with GO presences. The samples was prepared from the mortar bar samples, with GO and Pyrex Glass. In Figure 4-3(a) and (b), details of one of the cracks can be observed. But it is difficult to find any clue of GO in the crack. Therefore the method of seeking GO was changed. Some faults were selected to search for GO, with the result that something that looked like GO was found (see Figure 4-3(c) and (d)). Translucent materials can be seen on the fault, but one could not be totally confident that it was GO. More research was needed.

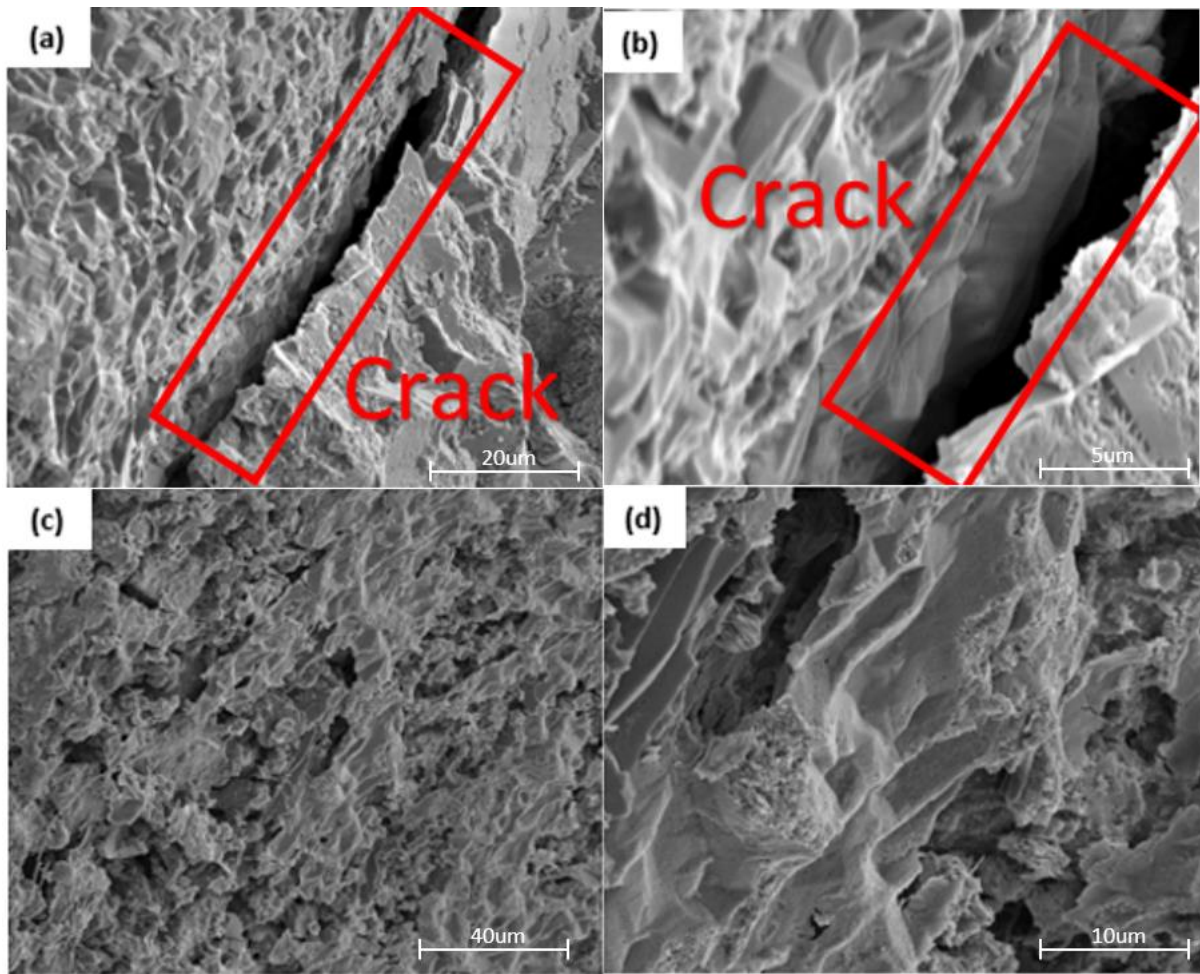


Figure 4-3 SEM showing cracks and GO-like features.

4.4 Conclusions

The main conclusions drawn from this research can be summarised as follows:

1. As evidenced in expansion testing, groups containing various proportions of GO showed lower expansion than control samples. This finding indicated the effect of GO to reduce ASR. However, the difference was not significantly large. Probable factors included lack of workability control and lack of long-term testing for late ages. Further research is necessary to improve on these experiments, especially focusing on those two factors. Meanwhile, with the use of SEM, micro-structural features were observed such as micro-cracks and different types

of ettringite. Evidence of GO in the cracks was not observed unequivocally, and further study is necessary.

2. The mechanical properties of mortar with GO were increased up to 25% for flexural strength. The samples containing 0.04% GO clearly showed the highest strength. One of the reasons for the improvement is supposed to be the pore structure refined by GO. More research is necessary to explain the mechanism by which GO improves mechanical properties. In the future, GO mortar has potential to be applied in 3D printing concrete for improved ASR resistance as investigated in this study. There may be other improvements in 3D printed concrete using GO mortar such as improvements in layer bonding as well as mechanical properties.

Chapter 5. Research on MoS₂ and WS₂: potential sensing material for 3D printing technology in concrete construction

5.1 Introduction

This chapter refers to declarations #2, #6 and #7.

It was mentioned in Chapter 1 that dimensional changes between layers of 3D printing concrete, especially with a second material incorporated, can result in significant durability problems in the long term. Differential movements between layers and potential cracks are dangerous to concrete structures. Thus, appropriate sensors for such strain changes are necessary. Usually, strain gauges are used to measure strain in an object. The gauges are often attached to objects by a suitable adhesive. As the objects are deformed, the foil is deformed, leading to the electrical resistance to change. By calculation through the gauge factor and the electrical resistance change, the strain can be obtained. However, most strain gauges are currently made of three-dimensional materials. The four disadvantages of conventional strain gauges are low strain level sustainability, limited resolution, slow responsivity and insufficient sensitivity. To overcome these drawbacks and provide sensors for the 3D printing technology of concrete construction, research has been conducted into semiconducting TMDs, due to their superior mechanical and optoelectronic properties.

The family (Mo,W) (S,Se)₂ has recently been intensively studied. First, TMDs undergo indirect to direct bandgap transition when thinning down to monolayer (Mak, Lee et al. 2010). The direct bandgap gives TMDs strong light absorption and photoluminescence (PL). Second, atomically thin TMDs are strongly covalently bonded yet have chemically inert van der Waals surfaces. Thus, TMDs are stable in various environments and demonstrate extremely small

bending rigidity k and exceptionally high Young's modulus (Bertolazzi, Brivio et al. 2011, Castellanos-Gomez, Poot et al. 2012, Liu, Yan et al. 2014). Third, monolayer TMDs show piezoelectricity due to broken inversion symmetry (Wu, Wang et al. 2014, Zhu, Wang et al. 2015). As a result, monolayer TMDs may have significant potential for flexible optoelectronics (Pu, Yomogida et al. 2012, Lee, Yu et al. 2013), piezotronics (Wu, Wang et al. 2014, Zhu, Wang et al. 2015), mechanically enhanced nanocomposites (Eksik, Gao et al. 2014) and smart materials for strain sensing (Bissett, Tsuji et al. 2014). In these applications, strain is inevitably a critical object requiring comprehensive understanding.

So far, substantial effort has been spent in the study of strain engineering to the band structure of TMDs by using bending (Castellanos-Gomez, Roldán et al. 2013, Conley 2013, He, Poole et al. 2013, Zhu, Wang et al. 2013, Wang 2015), high-pressure compression (Hui, Liu et al. 2013, Chi, Zhao et al. 2014, Nayak, Bhattacharyya et al. 2014, Nayak, Pandey et al. 2014, Fan, Zhu et al. 2015, Nayak, Yuan et al. 2015, Peña-Álvarez, del Corro et al. 2015, Zhao, Zhang et al. 2015, Dou, Ding et al. 2016) and tensile elongation (Liu, Amani et al. 2014). Results indicate that strain is an effective way to tune the bandgap from direct to indirect, generate the redshifts of trion and exciton peaks, and change the material conductivity from semiconducting to metallic (Roldán, Castellanos-Gomez et al. 2015). However, the important question of how strain relaxes within TMDs is still open.

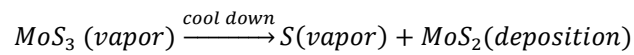
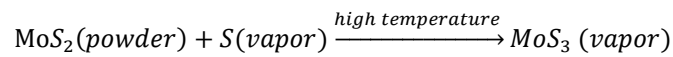
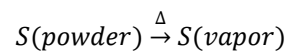
5.2 Experimental program

In this section, the methodology to address the research purposes is introduced. Generally, the main methodology in this project is laboratory experiments. The first is a CVD experiment to fabricate high-quality monolayer MoS₂ and WS₂ samples with large and ultra-smooth surfaces. The second is transferring CVD-grown monolayer samples to different substrates for further investigation. The third is analysing the CVD-grown samples and the transferred samples by

optical and atomic force microscopy (AFM). The fourth is finite element (FE) simulation by ABAQUS.

5.2.1 CVD technique for fabrication of monolayer MoS₂ and WS₂

In this project, a novel CVD method instead of mechanical exfoliation is applied to fabricate monolayer MoS₂ and WS₂ crystals. The governing reactions for MoS₂ are shown as follows, but that of WS₂ is much more complex and is not displayed here.



The groups of reactant are reacted in a CVD instrument, and Figure 5-1 provides a schematic representation of the experimental instrument and reactant.

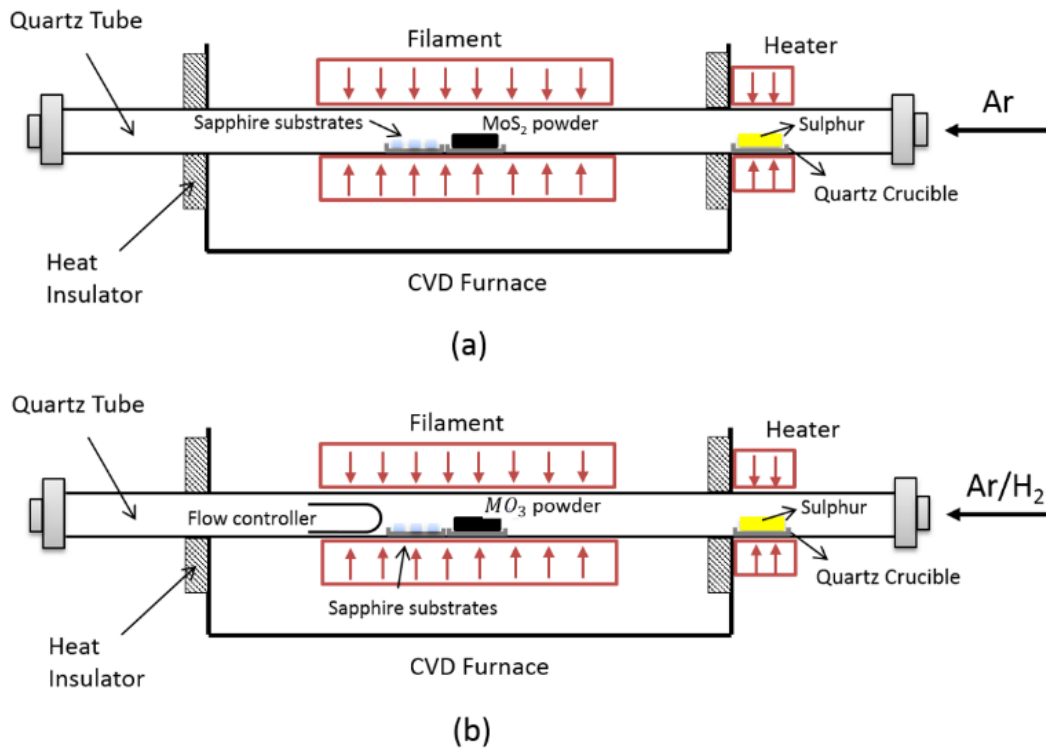


Figure 5-1 Schematic representation of the experimental instrument and reactants: a) MoS₂ and b) WS₂ (Zhang, Chang et al. 2016).

To fabricate monolayer MoS₂ and WS₂ crystals of high quality, the parameters of temperature, gas flow rate, heating rate, cooling rate and precursor powders should be optimised. To grow MoS₂, sulphur powder is heated to around 220°C for 30 min to produce sulphur vapour into the furnace. The temperature in the CVD furnace is gradually increased to around 950°C over 30 min. The reaction is protected by argon gas (60 sccm). At temperatures above 800°C, sulphur vapour reacts with MoS₂ powder to form MoS₂, which is volatile and forms MoS₂ vapour. After reaching the maximum target temperature, the furnace is rapidly cooled, to deposit MoS₂ flakes on sapphire substrates next to the MoS₂ powder on the quartz crucible. The reaction mechanism for growing WS₂ is similar, with some differences of precursor powder (WO₃), temperature and flow-rate control. The maximum temperature for WS₂ deposition is around 830°C, and the gas is substituted by a combination of argon and hydrogen with a tube-shaped flow controller.

5.2.2 Wet-chemical transfer technique

Wet-chemical transfer is versatile and suitable for transferring MoS₂ and WS₂ crystals onto different types of substrate including curved surfaces, silicate and polymer. The technique is based on the water wetting effect: water wets hydrophilic surfaces and avoids hydrophobic ones. Generally the wet-chemical transfer method has been used to prepare polymer-coated transmission electron microscopy grids before (Schneider, Calado et al. 2010).

In this project, MoS₂ and WS₂ flakes were transferred onto other substrates by the eight steps shown in Figure 5-2: (a) Spin coat PMMA film (hydrophobic) onto a sample by a spinner; (b) Make 3 Mol/L KOH solution; (c) Soak the sample in KOH solution at 100 °C for 2 hours; (d) Separate PMMA film with the help of the surface tension of water; (e) Soak PMMA film

in DI water for 1 hour; (f) Fish out PMMA film upwards onto a new substrate; (g) Bake the transferred sample for 10 to 15 mins; (h) Observe the transferred sample by optical microscope.

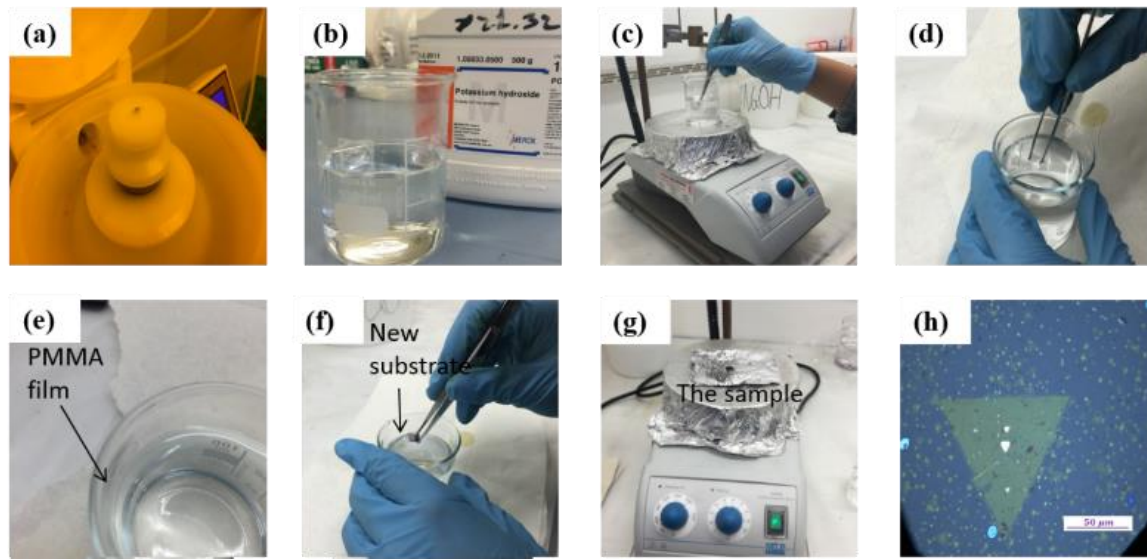


Figure 5-2 Eight steps for wet-chemical transfer technique.

5.2.3 Optical and AFM measurements

Raman/PL measurements were performed using a confocal microscope system (WITec alpha 300R) with a 50 \times objective lens. A 532 nm laser was used to excite samples placed on the loading frame. The spectra were collected using a 600-line mm⁻¹ grating. To avoid sample damage, 50 μ W laser power and 1 s integration time were applied during PL and Raman mapping. The PL intensity images were obtained by summing the PL intensity from 590 to 660 nm. The PL peaks of natural and charged excitons were estimated from Lorentzian fitting. The AFM measurement was carried out on a Bruker Dimension Icon in tapping mode.

5.2.4 FE simulation

The FE simulation of monolayer WS₂/PDMS model under tension was performed by ABAQUS (version 6.12). The model with WS₂ thickness of 20 μ m consisted of 30,315 nodes and 27,709 elements and the model with WS₂ size of 5 μ m consisted of 19,135 nodes and

17,107 elements. Perfect bonding was assumed at the interface between monolayer WS₂ and underlying polydimethylsiloxane (PDMS) in the model. Appropriate boundary conditions were applied along the edges of the specimen to simulate a uniaxial tensile test. The material properties of Young's modulus and Poisson's ratio adopted in the simulation were 350 kPa and 0.5 for PDMS, and 300 GPa and 0.3 for WS₂.

5.3 Results and discussion

5.3.1 Chemical vapour deposition (CVD) fabrication

CVD was applied to grow high-quality WS₂ crystals on atomically flat Al₂O₃ (0001) using WO₃ and S powders as the precursors; see Figure 5-3 and the Experimental section. In brief, the powders were located into the middle (WO₃) and upstream (S) of a 25 mm quartz tube and heated by furnace and heating tape to 800 and 200 °C in 0.5 h, respectively. Monolayer WS₂ was grown on sapphire substrates by maintaining the temperatures for 0.25 h. Figure 5-3(a), (b) and (c) shows the optical image and AFM topography of a representative grown WS₂ crystal on sapphire. The zoomed-in AFM image shown in Figure 5-3(c) indicates the atomic flatness of WS₂ crystals grown on the terraces of sapphire (0001). The edges of the triangular WS₂ crystal are raised in height due to water intercalation into the interface between the WS₂ and the hydrophilic sapphire substrate (Zheng, Xu et al. 2015). Scanning PL images taken under 532 nm excitation indicate uniform PL and Raman signals across the WS₂ crystal except for extraordinary PL intensity at the edges; see Figure 5-3(d), (e), and (f). It is inferred that the extraordinary PL intensity at the edges is related to the intercalated water based on the AFM image (Zheng, Xu et al. 2015). It should be noted that the uniform PL peak energy image shown in Figure 5-3(f) was obtained using single peak Lorentzian fitting to the mapped PL spectra.

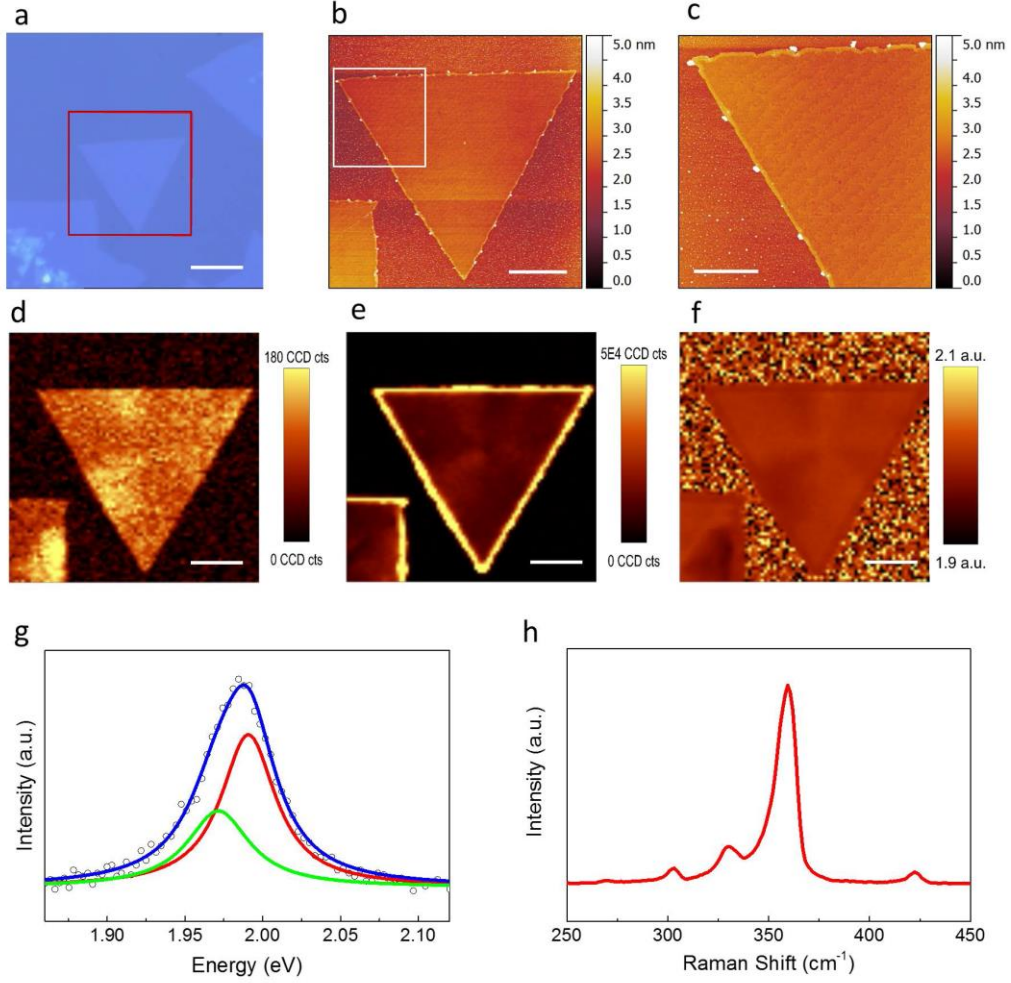


Figure 5-3 (a) Optical image of a WS₂ crystal grown on sapphire. (b) AFM height image of the WS₂ crystal on sapphire. (c) Height image of the square region shown in (b). (d-f) Integrated Raman intensity, integrated PL intensity and PL peak position mapping of the WS₂ crystal on sapphire. (g) PL spectrum of WS₂ on sapphire. Black circles are experimental data; blue line is a fit to the sum of two Lorentzians (red and green lines). (h) Raman spectrum of WS₂ on sapphire. Scale bar: 5 μ m in (a,b) and (d-f); 2 μ m in (c) (Zhang, Chang et al. 2016).

Figure 5-3(g) shows the PL spectrum of the WS₂ crystal on the sapphire growth substrate. A fit of the spectrum (blue line) indicates two Lorentzian peaks identified as due to the trion (X⁻, 1.972 eV, green line) and exciton (X₀, 1.991 eV, red line) with 19 MeV difference. The peak intensity ratio of exciton to trion is ≈ 2.0 , close to WS₂ or MoS₂ on SiO₂/Si with 10 V gate voltage, which is at negative doping (Mak, He et al. 2013, Zhu, Chen et al. 2015). It is therefore deduced that the trion binding energy should be ≤ 19 MeV since the energy difference between X⁻ and X₀ increases as the negative doping increases (Chernikov,

Van Der Zande et al. 2015, Zhu, Chen et al. 2015). The energies of trion binding as well as the X^- and X_0 peak energies are much smaller than those observed for WS_2 on SiO_2/Si (Zhu, Chen et al. 2015), possibly due to the larger dielectric constant of Al_2O_3 . Owing to the weak laser power (50 μW) of 532 nm excitation, the Raman spectrum taken from the WS_2 crystal only indicates the E' peak without showing the $A'1$ peak; see Figure 5-3(h).

5.3.2 Wet-chemical transfer technique

For the purpose of strain measurement, CVD-grown WS_2 crystals were transferred to PDMS substrates by the poly (methyl methacrylate) (PMMA)-assisted wet transfer method (see the Experimental Program section and Figure 5-4). Figure 5-4(a), (b), and (c) show the optical image and AFM topography mapping of the same WS_2 crystal as presented in Figure 5-4, after being transferred on PDMS. The flake is rotated due to the transfer process. It can be seen that the transferred crystal remains intact and clean except for serration of the edges and the appearance of a few wrinkles; see the zoomed-in topography image in Figure 5-5(c). The bulk of the crystal is unaffected by the transfer process. The serration of the edges points to defects along the edges as active locations for potassium hydroxide (KOH) etching of the WS_2 crystal, while no KOH etching is observed on the main body of the WS_2 crystal, indicating a lack of substantial defects. It should be noted that the extraordinary PL intensity around the edges of WS_2 disappears after being transferred to PDMS; see Figure 5-4(e). The disappearance is likely caused by the combination of KOH etching to the edge and the inability of water intercalation in the space between WS_2 and hydrophobic PDMS (Zheng, Xu et al. 2015). Also, the PL intensity decreases from edge to centre after being transferred. This feature has been observed on intact CVD-grown WS_2 as well as due to the chemical heterogeneity (Kim, Yun et al. 2016, Liu, Lu et al. 2016). It is therefore believed that the crystals transferred here remain high in quality, comparable to those before being transferred. In particular, the uniform Raman (Figure

5-4(d)) and PL peak position signal (Figure 5-4(f)) across the crystal confirm the quality of the transferred crystals without substantial defects such as cracks and holes.

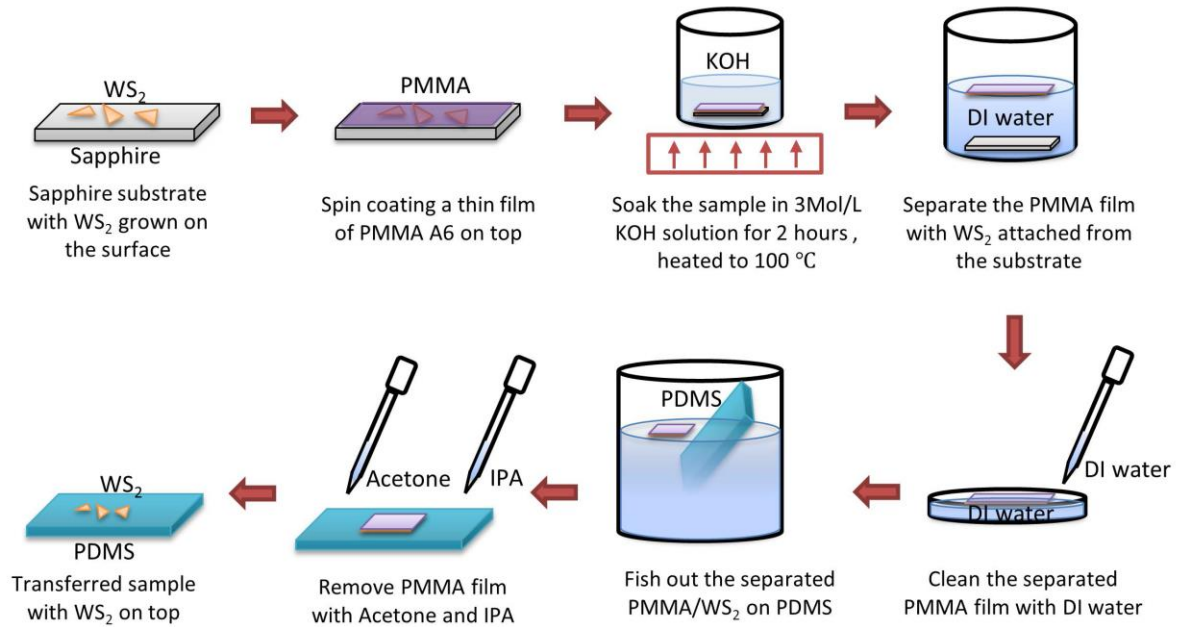


Figure 5-4 Schematic illustration of WS_2 crystals transferred by a PMMA-assisted wet-chemical method on PDMS substrate (Zhang, Chang et al. 2016).

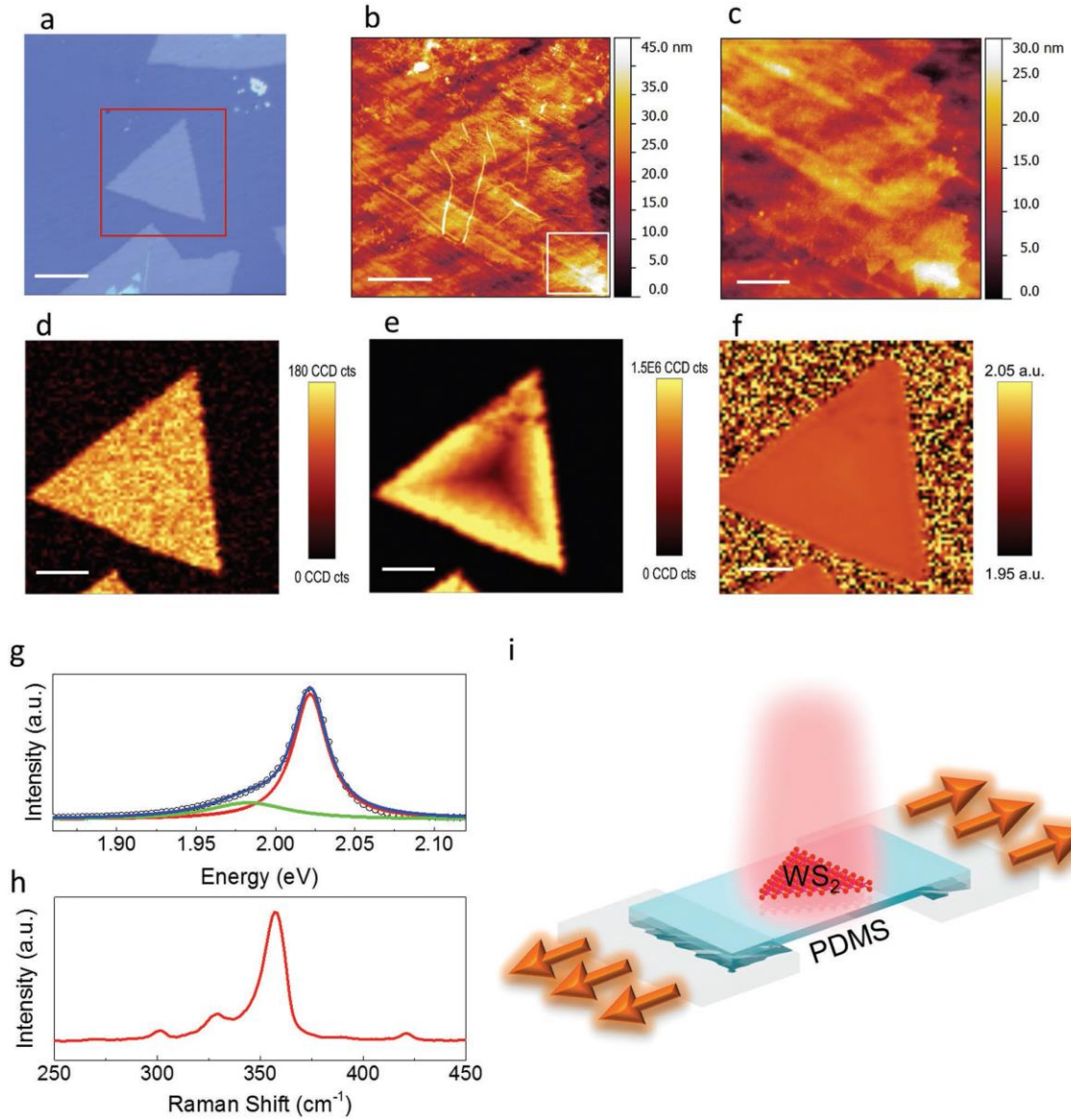


Figure 5-5 a) Optical image of a WS₂ crystal transferred on PDMS substrate. b) AFM height image of the WS₂ crystal on PDMS. c) Height image of the square region shown in (b). d–f) Integrated Raman intensity, integrated PL intensity and PL peak position mapping of the WS₂ crystal on PDMS. g) PL spectrum of WS₂ on PDMS without strain. Black circles are experimental data; blue line is a fit to the sum of two Lorentzians (red and green lines). h) Raman spectrum of WS₂ on PDMS without strain. i) Schematic of tensile stress loading frame. Scale bar: 5 μm in (a) and (b) and (d)–(f); 1 μm in (c) (Zhang, Chang et al. 2016).

Figure 5-5 (g) shows a PL spectrum of the transferred crystal at zero strain ($\epsilon = 0$, black circle). By Lorentzian fitting, the PL spectrum is composed of trion X⁻ (green) and exciton X₀ (red) emissions at 1.983 and 2.022 eV, respectively, with ≈ 40 MeV difference. The peak positions and difference are shifted somewhat relative to the unstrained crystal on sapphire, again possibly due to change in the dielectric environment. The dominance of the X₀ peak, of

which the peak intensity is approximately seven times higher than that of X^- , indicates that PDMS is a clean substrate contributing little doping (Buscema, Steele et al. 2014). The clean substrate is desirable to maintain strong light–matter interaction and achieve a sharp PL peak for sensitive applications, since high doping weakens the PL intensity and broadens the peak width (Mak, He et al. 2013, Buscema, Steele et al. 2014, Zhu, Chen et al. 2015). Figure 5-4(i) shows the schematic of the strain measurement setup. The WS_2 /PDMS substrate can be strongly attached to the homemade loading frame after oxygen plasma treatment to the contact surface of PDMS. The loading frame is designed to fit into the commercial Raman microscope (WITec, Alpha300 R) for in-situ optical spectrum measurement of strained crystals.

5.3.3 Strain relaxation of WS_2 on PDMS substrate by Raman and PL and FE simulation

These experiments indicated that the WS_2 crystals undergo linear redshifts of X_0 and X^- peaks in PL and the E' peak in Raman, when the uniaxial tensile strain of PDMS substrate is increased from 0 to 0.16. However, strain relaxation of WS_2 was observed in the formation of wrinkles and cracks (in large crystals) when the substrate strain was further increased from 0.16 to 0.32. More interestingly, the wrinkle patterns were found to depend on the crystal orientation relative to the tensile strain direction. While the wrinkles were distributed uniformly across the triangular WS_2 crystal with an edge parallel to the tensile direction, localised wrinkles within the crystal were formed with an edge perpendicular to the tensile direction. These observations were explained by the FE simulations indicating that the pattern of wrinkling reflected the pattern of strain distribution within each crystal, see Figure 5-6. These results indicated that for 2D TMD materials to be employed in the stretchable electronics field, the linear relationship between optical spectral shift to tensile strain only applied when tensile strains were small. Beyond a critical strain value, a new relationship must be established for

correct strain indication, taking wrinkle formation into consideration. Also, triangular TMD crystals with one edge oriented parallel to the tensile strain direction were preferable for straintronics due to more uniform strain distribution. These results will help understanding of the mechanical properties of TMD crystals and shed light on the design of high-quality straintronics and flexible electronics.

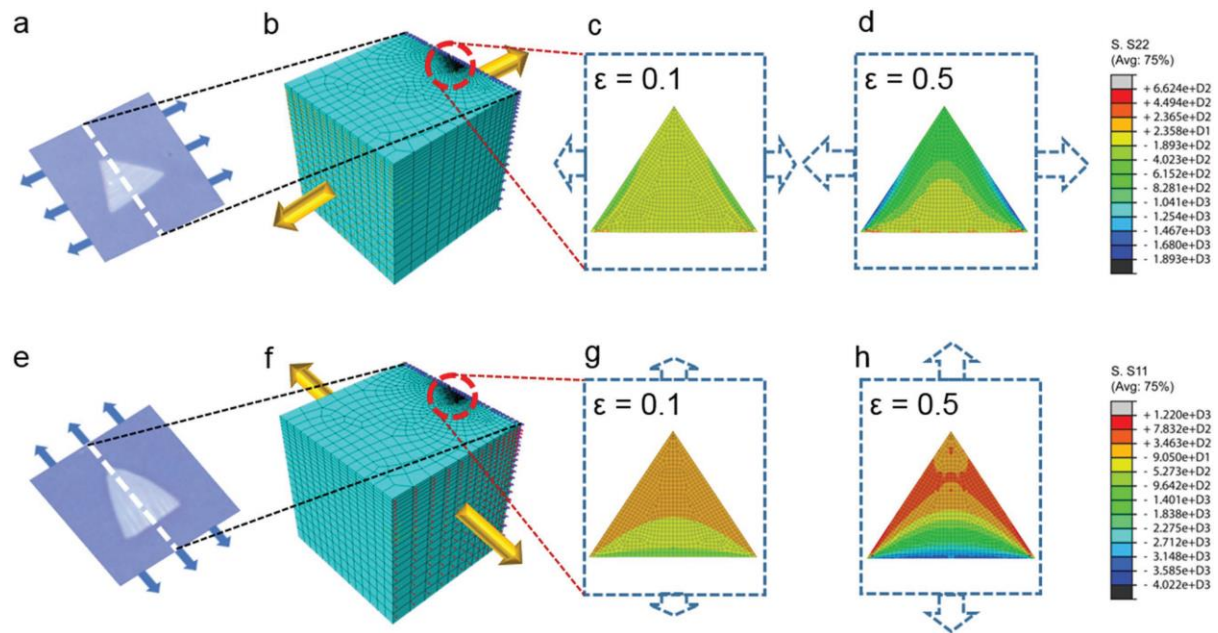


Figure 5-6 Finite element (FE) simulation of WS_2 under tensile strain. a,b) FE model of WS_2 /PDMS sample under tensile strain corresponding to the case in Figure 4a. c,d) Snapshots of FE simulation results of WS_2 under the substrate strain at 0.1 and 0.5. e,f) FE model of WS_2 /PDMS sample under tensile strain corresponding to the case in Figure 4b,c. g,h) Snapshots of FE simulation results of WS_2 under substrate strain at 0.1 and 0.5 (Zhang, Chang et al. 2016)..

5.4 Conclusions

TMDs such as MoS_2 and WS_2 have the potential to be made into new generation strain gauges due to their superior mechanical and optoelectronic properties. This can lead to the development of a sensing technique for 3D printing technology of concrete construction. For example, such TMDs could be embedded into 3D printed mortar layers to monitor dimensional changes by strain. In this study, the fabrication, transfer methods and some strain behaviours were investigated, and the corresponding conclusions were drawn as follows.

1. The CVD method proved to be a strong candidate for the fabrication of thin-layer MoS_2 and WS_2 flakes with smooth surface in large quantity.
2. The wet transfer method was successfully used to transfer fabricated MoS_2 and WS_2 from sapphire to other substrates such as PDMS.
3. PL and Raman results indicated linear tensile strain by elongating the PDMS substrate on which the transferred WS_2 crystals sat, when the uniaxial tensile strain of PDMS substrate was increased from 0 to 0.16. However, with the tensile strain increased from 0.16 to 0.32, strain relaxation of WS_2 occurred. Moreover, triangular TMD crystals with one edge oriented parallel to the tensile strain direction were preferable for straintronics due to more uniform strain distribution. The situation was confirmed by FE simulation.

Chapter 6. Conclusions and recommendations

3D printing has become an alternative to replace the traditional concrete construction industry by virtue of its specific advantages such as high automation, cost-effectiveness, time-efficiency, and ease in customising structures. However, there are still some bottlenecks facing this technology on concrete, with regard to mechanical properties, reinforcements, curing conditions, durability, interlayer bonding, the relationships among hardening time, pumpability and extrudability, and applicability (Xu, Chen et al. 2016). Among these, poor interlayer bonding is a typical obstacle currently limiting the development of 3D printing technology on concrete construction. In this thesis, research into enhancement approaches to bonding between 3D printed layered mortars was performed. Next, ASR was investigated, since the potential dimensional change caused by a high content of ASR reactive aggregate in 3D printing mortar is believed to result in marked deterioration in the long term. Thirdly, emphasis was placed on the sensing method for dimensional change between 3D printed layered mortars, especially with the incorporation of epoxy or other adhesive. TMDs such as MoS₂ and WS₂ have potential as candidates for addressing problems such as strain gauge. Studies of fabrication, transfer and mechanical testing of the materials was conducted.

In this chapter, conclusions and recommendations are drawn. The key findings are summarised from the previous chapters, on which basis recommendations are put forward corresponding to each chapter.

6.1 Key research findings

1. Epoxy adhesive helps improve interlayer bonding, with the specific curing condition by epoxy being 150% over 28 days. This finding indicates the effectiveness of epoxy in enhancing the interlayer bonding strength of 3D printed mortar. SEM

characterisation explains the reason in the physical aspect, as interlocking between epoxy and CSH is found. Moreover, chemical bonds between layers are also found by MD simulation, which is strong evidence for the significant strength improvement. A new BCS polymer was investigated by MD simulation, and proved to be effective.

2. Incorporating PVA fibres into the abovementioned system further improves interlayer bonding strength. With 3 vol.% PVA fibres, specimens showed a 21% increase compared with those without PVA fibres. It reaches 52.4% of control of integrated mortar. This finding indicates that the approach has potential for application in concrete construction. SEM characterisation explains the additional improvement in the physical aspect by a bridging mechanism formed of PVA fibres between epoxy and mortar.
3. Curing temperature for epoxy influences the interlayer bonding strength. Curing temperature affects not only epoxy strength itself, but also the interface between epoxy and mortar. For both approaches, 40 degrees is recommended as the optimised curing temperature. Between curing temperatures 30 and 60 degrees, the second approach showed better performance.
4. Printing interval time affects the interlayer bonding strength as well. For the long term, 30 minutes printing interval time is recommended with highest tensile strength for both groups with epoxy and epoxy with PVA fibres. The reason why 15 minutes time delay shows lower strength is supposed to be attributed to bleeding water. Thus, the water/binder ratio can influence the final interlayer bonding strength.
5. Based on the expansion test, groups containing various proportions of GO show less expansion compared to control samples. This finding indicates the effect of GO on reducing ASR. However, the difference is not significantly large. Likely factors include lack of workability control and lack of long-term testing for late ages. Further research is necessary to extend the experiments, especially based on these two factors.

6. The CVD method proves to be an excellent candidate for fabricating large quantities of thin-layer MoS₂ and WS₂ flakes with smooth surfaces. The wet transfer method was successfully used to transfer fabricated MoS₂ and WS₂ from sapphire to other substrates such as PDMS. PL and Raman results indicated linear tensile strain by elongating the PDMS substrate on which the transferred WS₂ crystals sat, when the uniaxial tensile strain of the PDMS substrate was increased from 0 to 0.16. However, when the tensile strain was increased from 0.16 to 0.32, strain relaxation of WS₂ occurred. Moreover, triangular TMD crystals with one edge oriented parallel to the tensile strain direction are preferred for straintronics due to their more uniform strain distribution. This situation was confirmed by FE simulation.

6.2 Recommended approaches and parameters

Based on this research master's study, recommendations are made in this section. First, the approach of using epoxy adhesive to enhance interlayer bonding of 3D printed mortar is shown in Table 6-1 with parameters. Additionally, the approach of using epoxy and PVA fibres to the bond is recommended in Table 6-2 with parameters. For both these recommendations, it is suggested that researchers refer to them and optimise the parameters based on their research objectives.

Table 6-1 Parameters of the approach using epoxy adhesive to enhance interlayer bonding of 3D printed mortar

Type of cement	GP cement conforming to AS 3972
Type of water reducer	Sika ViscoCrete-2100
Type of epoxy	Araldite 2000+
Water to cement mass ratio	0.3
Sand to cement mass ratio	1.5
Water reducer to cement mass ratio	0.3%
Epoxy Part A to Part B mass ratio	1.25
Printing interval time	30 mins
Epoxy curing temperature	40 centidegrees
Epoxy curing time	10 hours

Table 6-2 Parameters of the approach using epoxy and PVA fibres to enhance interlayer bonding of 3D printed mortar

Type of cement	GP cement conforming to AS 3972
Type of water reducer	Sika ViscoCrete-2100
Type of epoxy	Araldite 2000+
Type of fibre	PVA fibre
Diameter of fibre	0.1 mm
Length of fibre	13 mm
Water to cement mass ratio	0.3
Sand to cement mass ratio	1.5
Water reducer to cement mass ratio	0.3%
Epoxy Part A to Part B mass ratio	1.25
Fibre to epoxy volume ratio	3%
Printing interval time	30 mins
Epoxy curing temperature	40 centidegrees
Epoxy curing time	10 hours

For studies using GO to reduce ASR, the optimal fraction of GO is 0.04% of cement as recommended. However, because the improvement was not as significant as expected, researchers should repeat and modify such experiments in future.

For the study of TMDs, the CVD method is recommended. To grow MoS₂, sulphur powder is heated to around 220°C in 30 min to transmit sulphur vapour into the CVD furnace. In the CVD furnace, the temperature is gradually increased to around 950°C over 30 min. The reaction is protected by argon gas (60 sccm). At temperatures above 800°C, sulphur vapour reacts with MoS₂ powder to form MoS₃ which is volatile and forms MoS₃ vapour. After reaching the maximum target temperature, the furnace is rapidly cooled to deposit MoS₂ flakes on sapphire substrates next to the MoS₂ powder on a quartz crucible. For WS₂, the reaction mechanism is similar with some differences in the precursor powder (WO₃), temperature and flow-rate control. The maximum temperature for WS₂ deposition is around 830°C, and the gas is substituted by the combination of argon and hydrogen with a tube-shaped flow controller. In future, based on the current findings, there is high incentive for investigation of TMDs as candidates for sensing material. This would help solve some of the problems in 3D printing technology on concrete, especially sensing aspects.

6.3 Future research

Due to time limitation of the master's study, the study is not comprehensive enough to provide application perspective. In the future, there are still some relating works based on this study can be investigated.

1. It has been shown that epoxy can be one approach to improving interlayer bonding strength of 3D printed mortar. In this study, the epoxy has been used for study is Aradite 2000+. More

types of epoxy are necessary to be investigated to see whether they have similar properties, and to find the best resolution.

2. PVA fibres have been proved to be effective to improve interlayer bonding of epoxy modified 3D printed mortar. However, the dosage and parameters of the fibres have not been specified. In the future, researchers need to do more research on the parameters and even types of fibres to modify this approach.

3. About the study to use GO to improve ASR in 3D printing concrete, experiment data is limited. Future researchers need to do more experiments, and simulations if applicable.

References

- Al-Ostaz, A., W. Wu, A.-D. Cheng and C. Song (2010). "A molecular dynamics and microporomechanics study on the mechanical properties of major constituents of hydrated cement." Composites Part B: Engineering **41**(7): 543-549.
- Alec. (2014). "Minnesotan man builds the world's first 3D printed concrete castle in his own backyard, designing a kid that can print two-story houses." Retrieved 08/06, 2016, from <http://www.3ders.org/articles/20140826-minnesotan-world-first-3d-printed-concrete-castle-in-his-own-backyard.html>.
- ASTM (2015). Standard Terminology for Additive Manufacturing Technologies. F2792-12a. West Conshohocken, ASTM International.
- ASTM C441 (2012). Standard Test Method for Effectiveness of Pozzolans or Ground Blast-Furnace Slag in Preventing Excessive Expansion of Concrete Due to the Alkali-Silica Reaction. ASTM C441. West Conshohocken, Pennsylvania, American Society for Testing and Materials.
- ASTM C1567 (2012). Standard Test Method for Determining the Potential ASR of Combinations of Cementitious Materials and Aggregate. West Conshohocken, Pennsylvania, American Society for Testing and Materials.
- Austin, S., P. Robins and Y. Pan (1995). "Tensile bond testing of concrete repairs." Materials and Structures **28**(5): 249.
- Australian Government (2014). Green Paper on Developing Northern Australia. D. o. t. P. M. a. Cabinet.
- Australian Government (2015). Building Australia's infrastructure. Australia Budget 2014-2015.
- Barnett, E. and C. Gosselin (2015). "Large-scale 3D printing with a cable-suspended robot." Additive Manufacturing **7**: 27-44.
- Begum, R. A., S. K. Satari and J. J. Pereira (2010). "Waste generation and recycling: comparison of conventional and industrialized building systems." American Journal of Environmental Sciences **6**(4): 383-388.
- Berendsen, H. J., J. v. Postma, W. F. van Gunsteren, A. DiNola and J. Haak (1984). "Molecular dynamics with coupling to an external bath." The Journal of chemical physics **81**(8): 3684-3690.
- Bertolazzi, S., J. Brivio and A. Kis (2011). "Stretching and breaking of ultrathin MoS₂." ACS nano **5**(12): 9703-9709.
- Betterman, L., C. Ouyang and S. Shah (1995). "Fiber-matrix interaction in microfiber-reinforced mortar." Advanced Cement Based Materials **2**(2): 53-61.
- Bissett, M. A., M. Tsuji and H. Ago (2014). "Strain engineering the properties of graphene and other two-dimensional crystals." Physical Chemistry Chemical Physics **16**(23): 11124-11138.
- Buscema, M., G. A. Steele, H. S. van der Zant and A. Castellanos-Gomez (2014). "The effect of the substrate on the Raman and photoluminescence emission of single-layer MoS₂." Nano research **7**(4): 561-571.
- CAN, C. (2004). "A23. 3." Design of concrete structures. Canadian Standards Association, Rexdale, Ontario, Canada.
- Castellanos-Gomez, A., R. Roldán, E. Cappelluti, M. Buscema, F. Guinea, H. S. van der Zant and G. A. Steele (2013). "Local strain engineering in atomically thin MoS₂." Nano letters **13**(11): 5361-5366.

Castellanos - Gomez, A., M. Poot, G. A. Steele, H. S. van der Zant, N. Agrait and G. Rubio - Bollinger (2012). "Elastic properties of freely suspended MoS₂ nanosheets." Advanced Materials **24**(6): 772-775.

Chernikov, A., A. M. Van Der Zande, H. M. Hill, A. F. Rigosi, A. Velauthapillai, J. Hone and T. F. Heinz (2015). "Electrical tuning of exciton binding energies in monolayer WS₂." Physical review letters **115**(12): 126802.

Chi, Z.-H., X.-M. Zhao, H. Zhang, A. F. Goncharov, S. S. Lobanov, T. Kagayama, M. Sakata and X.-J. Chen (2014). "Pressure-induced metallization of molybdenum disulfide." Physical review letters **113**(3): 036802.

Chiu, M.-H., M.-Y. Li, W. Zhang, W.-T. Hsu, W.-H. Chang, M. Terrones, H. Terrones and L.-J. Li (2014). "Spectroscopic signatures for interlayer coupling in MoS₂-WSe₂ van der Waals stacking." ACS nano **8**(9): 9649-9656.

Clark, L. (1989). Critical review of the structural implications of the alkali silica reaction in concrete, Bridges Design, Structures Group, Transportation and Road Research Laboratory.

Clark, S. J., M. D. Segall, C. J. Pickard, P. J. Hasnip, M. I. Probert, K. Refson and M. C. Payne (2005). "First principles methods using CASTEP." Zeitschrift für Kristallographie-Crystalline Materials **220**(5/6): 567-570.

Collepari, M. (2010). "Damage of concrete by sulphate attack and alkali-silica reaction." International Journal of Structural Engineering **1**(2): 108-115.

Committee, A., A. C. Institute and I. O. f. Standardization (2008). Building code requirements for structural concrete (ACI 318-08) and commentary, American Concrete Institute.

Conley, H. J. (2013). "HJ Conley, B. Wang, JI Ziegler, RF Haglund, ST Pantelides, and KI Bolotin, Nano Lett. 13, 3626 (2013)." Nano Lett. **13**: 3626.

Cooper, R. C., C. Lee, C. A. Marianetti, X. Wei, J. Hone and J. W. Kysar (2013). "Nonlinear elastic behavior of two-dimensional molybdenum disulfide." Physical Review B **87**(3): 035423.

Craveiro, F., J. M. de Matos, H. Bártolo and P. Bártolo (2012). An Innovation System for Building Manufacturing. ASME 2012 11th Biennial Conference on Engineering Systems Design and Analysis, American Society of Mechanical Engineers.

Designing Buildings Wiki. (2016). "Lead times for construction." Retrieved 06/06, 2016, from http://www.designingbuildings.co.uk/wiki/Lead_times_for_construction.

Dezeen. (2016). "Amalgamma develops 3D-printed concrete for building." Retrieved 07/06, 2016, from <http://www.dezeen.com/2016/01/21/amalgamma-devel-ops-3d-printing-concrete-technique-building-structures-bartlett/>.

Dini, E. (2016). "D-Shape." Monolite UK Ltd.< <http://www.d-shape.com/cose> >.

Dou, X., K. Ding, D. Jiang, X. Fan and B. Sun (2016). "Probing spin-orbit coupling and interlayer coupling in atomically thin molybdenum disulfide using hydrostatic pressure." ACS nano **10**(1): 1619-1624.

Eindhoven University of Technology. (2015). "TU Eindhoven starts using kingsize 3D concrete printer." Retrieved 07/06, 2016, from <https://www.tue.nl/en/university/news-and-press/news/22-10-2015-tu-eindhoven-starts-using-kingsize-3d-concrete-printer/>.

Eksik, O., J. Gao, S. A. Shojaei, A. Thomas, P. Chow, S. F. Bartolucci, D. A. Lucca and N. Koratkar (2014). "Epoxy nanocomposites with two-dimensional transition metal dichalcogenide additives." ACS nano **8**(5): 5282-5289.

Fan, W., X. Zhu, F. Ke, Y. Chen, K. Dong, J. Ji, B. Chen, S. Tongay, J. W. Ager and K. Liu (2015). "Vibrational spectrum renormalization by enforced coupling across the van der Waals gap between Mo S₂ and W S₂ monolayers." Physical Review B **92**(24): 241408.

- Farny, J. A. and S. H. Kosmatka (1997). Diagnosis and control of alkali-aggregate reactions in concrete, Portland Cement Association.
- Feng, P., X. Meng, J.-F. Chen and L. Ye (2015). "Mechanical properties of structures 3D printed with cementitious powders." Construction and Building Materials **93**: 486-497.
- Fernandes, I. and M. A. Broekmans (2013). "Alkali-silica reactions: an overview. Part I." Metallography, Microstructure, and Analysis **2**(4): 257-267.
- Ganatra, R. and Q. Zhang (2014). "Few-Layer MoS₂: A Promising Layered Semiconductor." ACS nano.
- Gillette, R. W. (1963). Performance of Bonded Concrete Overlays. Journal Proceedings.
- Glasser, L. D. and N. Kataoka (1981). "The chemistry of 'alkali-aggregate' reaction." Cement and Concrete Research **11**(1): 1-9.
- Havencab. (2016). "3D Printing Construction: sustainability and cost effectiveness." Retrieved 07/06, 2016, from <http://www.havencab.com.au/3d-printing-construction-sustainability-and-cost-effectiveness/>.
- He, K., C. Poole, K. F. Mak and J. Shan (2013). "Experimental demonstration of continuous electronic structure tuning via strain in atomically thin MoS₂." Nano letters **13**(6): 2931-2936.
- Hobbs, D. (1986). "Deleterious expansion of concrete due to alkali-silica reaction: influence of PFA and slag." Magazine of Concrete Research **38**(137): 191-205.
- Hossain, K., M. Lachemi, M. Sammour and M. Sonebi (2013). "Strength and fracture energy characteristics of self-consolidating concrete incorporating polyvinyl alcohol, steel and hybrid fibres." Construction and Building Materials **45**: 20-29.
- Huang, Y., M. C. Leu, J. Mazumder and A. Donmez (2015). "Additive manufacturing: Current state, future potential, gaps and needs, and recommendations." Journal of Manufacturing Science and Engineering **137**(1): 014001.
- Hui, Y., X. Liu and W. Jie (2013). "YY Hui, X. Liu, W. Jie, NY Chan, J. Hao, Y.-T. Hsu, L.-J. Li, W. Guo, and SP Lau, ACS Nano 7, 7126 (2013)." ACS Nano **7**: 7126.
- Hurd, M. K. (2005). Formwork for concrete, American Concrete Institute.
- Institution, B. S. (2004). Eurocode 2: Design of Concrete Structures: Part 1-1: General Rules and Rules for Buildings, British Standards Institution.
- Jaillon, L., C.-S. Poon and Y. Chiang (2009). "Quantifying the waste reduction potential of using prefabrication in building construction in Hong Kong." Waste management **29**(1): 309-320.
- Jimenez Garcia, M. (2016). "RC4 – Amalgamma." Retrieved 07/06, 2016, from <https://www.behance.net/gallery/33526609/RC4-Amalgama>.
- Keating, S. (2014). "Beyond 3D Printing: The New Dimensionsof Additive Fabrication." Designing for Emerging Technologies: UX for Genomics, Robotics, and the Internet of Things: 379.
- Keating, S. and N. Oxman (2012). "Immaterial robotic fabrication." Proceedings of RobArch: robotic fabrication in architecture, art and design.
- Khoshnevis, B. (2004). "Automated construction by contour crafting—related robotics and information technologies." Automation in construction **13**(1): 5-19.
- Kim, M. S., S. J. Yun, Y. Lee, C. Seo, G. H. Han, K. K. Kim, Y. H. Lee and J. Kim (2016). "Biexciton emission from edges and grain boundaries of triangular WS₂ monolayers." ACS nano **10**(2): 2399-2405.
- Kruth, J.-P. (1991). "Material inccress manufacturing by rapid prototyping techniques." CIRP Annals-Manufacturing Technology **40**(2): 603-614.

- Le, T. T., S. A. Austin, S. Lim, R. A. Buswell, A. G. Gibb and T. Thorpe (2012). "Mix design and fresh properties for high-performance printing concrete." Materials and structures **45**(8): 1221-1232.
- Le, T. T., S. A. Austin, S. Lim, R. A. Buswell, R. Law, A. G. Gibb and T. Thorpe (2012). "Hardened properties of high-performance printing concrete." Cement and Concrete Research **42**(3): 558-566.
- Leach, N., A. Carlson, B. Khoshnevis and M. Thangavelu (2012). "Robotic construction by contour crafting: the case of lunar construction." International Journal of Architectural Computing **10**(3): 423-438.
- Ledbetter, H. (1981). "Stainless - steel elastic constants at low temperatures." Journal of Applied Physics **52**(3): 1587-1589.
- Lee, G., Y. Yu and X. Cui (2013). "G.-H. Lee, Y.-J. Yu, X. Cui, N. Petrone, C.-H. Lee, MS Choi, D.-Y. Lee, C. Lee, WJ Yoo, K. Watanabe, T. Taniguchi, C. Nuckolls, P. Kim, and J. Hone, ACS Nano 7, 7931 (2013)." ACS Nano **7**: 7931.
- Lee, Y. H., X. Q. Zhang, W. Zhang, M. T. Chang, C. T. Lin, K. D. Chang, Y. C. Yu, J. T. W. Wang, C. S. Chang and L. J. Li (2012). "Synthesis of large - area MoS₂ atomic layers with chemical vapor deposition." Advanced materials **24**(17): 2320-2325.
- Lehmann, S. (2013). "Low carbon construction systems using prefabricated engineered solid wood panels for urban infill to significantly reduce greenhouse gas emissions." Sustainable Cities and Society **6**: 57-67.
- Lim, S., R. A. Buswell, T. T. Le, S. A. Austin, A. G. Gibb and T. Thorpe (2012). "Developments in construction-scale additive manufacturing processes." Automation in construction **21**: 262-268.
- Lim, S., R. A. Buswell, T. T. Le, R. Wackrow, S. A. Austin, A. G. Gibb and T. Thorpe (2011). "Development of a viable concrete printing process."
- Lin, Y.-C., W. Zhang, J.-K. Huang, K.-K. Liu, Y.-H. Lee, C.-T. Liang, C.-W. Chu and L.-J. Li (2012). "Wafer-scale MoS₂ thin layers prepared by MoO₃ sulfurization." Nanoscale **4**(20): 6637-6641.
- Link, J. (2015). "3D printing concrete: a 2500-square-foot house in 20 hours and an eye on a moon shot." Retrieved 07/06, 2016, from <https://lineshapespace.com/3d-printing-concrete/>.
- Liu, H., J. Lu, K. Ho, Z. Hu, Z. Dang, A. Carvalho, H. R. Tan, E. S. Tok and C. H. Sow (2016). "Fluorescence concentric triangles: a case of chemical heterogeneity in WS₂ atomic monolayer." Nano letters **16**(9): 5559-5567.
- Liu, K., Q. Yan, M. Chen, W. Fan, Y. Sun, J. Suh, D. Fu, S. Lee, J. Zhou and S. Tongay (2014). "Elastic Properties of Chemical-Vapor-Deposited Monolayer MoS₂, WS₂, and Their Bilayer Heterostructures." Nano letters **14**(9): 5097-5103.
- Liu, Z., M. Amani, S. Najmaei, Q. Xu, X. Zou, W. Zhou, T. Yu, C. Qiu, A. G. Birdwell and F. J. Crowne (2014). "Strain and structure heterogeneity in MoS₂ atomic layers grown by chemical vapour deposition." Nature communications **5**: 5246.
- Loughborough University. (2016). "The 7 categories of Additive Manufacturing." Retrieved 08/06, 2016, from <http://www.lboro.ac.uk/research/amrg/about/the7categoriesofadditivemanufacturing/>.
- Lu, J., J. H. Lu, H. Liu, B. Liu, K. X. Chan, J. Lin, W. Chen, K. P. Loh and C. H. Sow (2014). "Improved photoelectrical properties of MoS₂ films after laser micromachining." Acs Nano **8**(6): 6334-6343.
- Lu, W. and H. Yuan (2010). "Exploring critical success factors for waste management in construction projects of China." Resources, conservation and recycling **55**(2): 201-208.
- Ma, G. and L. Wang (2017). "A critical review of preparation design and workability measurement of concrete material for largescale 3D printing." Frontiers of Structural and Civil Engineering: 1-19.

- Mak, K. F., K. He, C. Lee, G. H. Lee, J. Hone, T. F. Heinz and J. Shan (2013). "Tightly bound trions in monolayer MoS 2." Nature materials **12**(3): 207.
- Mak, K. F., C. Lee, J. Hone, J. Shan and T. F. Heinz (2010). "Atomically thin MoS 2: a new direct-gap semiconductor." Physical review letters **105**(13): 136805.
- Mao, C., Q. Shen, L. Shen and L. Tang (2013). "Comparative study of greenhouse gas emissions between off-site prefabrication and conventional construction methods: two case studies of residential projects." Energy and Buildings **66**: 165-176.
- May, C. (1987). Epoxy resins: chemistry and technology, CRC press.
- Morena, J. J. (1988). Advanced composite mold making, Van Nostrand Reinhold co. New York.
- National Ready Mix Concrete Association (1998). "CIP5 - Plastic Shrinkage Cracking."
- Nayak, A. P., S. Bhattacharyya, J. Zhu, J. Liu, X. Wu, T. Pandey, C. Jin, A. K. Singh, D. Akinwande and J.-F. Lin (2014). "Pressure-induced semiconducting to metallic transition in multilayered molybdenum disulphide." Nature communications **5**: ncomms4731.
- Nayak, A. P., T. Pandey, D. Voiry, J. Liu, S. T. Moran, A. Sharma, C. Tan, C.-H. Chen, L.-J. Li and M. Chhowalla (2014). "Pressure-dependent optical and vibrational properties of monolayer molybdenum disulfide." Nano letters **15**(1): 346-353.
- Nayak, A. P., Z. Yuan, B. Cao, J. Liu, J. Wu, S. T. Moran, T. Li, D. Akinwande, C. Jin and J.-F. Lin (2015). "Pressure-modulated conductivity, carrier density, and mobility of multilayered tungsten disulfide." ACS nano **9**(9): 9117-9123.
- Nematollahi, B., M. Xia and J. Sanjayan (2017). Current progress of 3D concrete printing technologies. ISARC. Proceedings of the International Symposium on Automation and Robotics in Construction, Vilnius Gediminas Technical University, Department of Construction Economics & Property.
- Noushini, A., B. Samali and K. Vessalas (2013). "Effect of polyvinyl alcohol (PVA) fibre on dynamic and material properties of fibre reinforced concrete." Construction and Building Materials **49**: 374-383.
- Ong, K., M. Basheerkhan and P. Paramasivam (1999). "Resistance of fibre concrete slabs to low velocity projectile impact." Cement and Concrete Composites **21**(5-6): 391-401.
- Pan, Z., W.H. Duan, D. Li and F. Collins (2012). Graphene oxide reinforced cement and concrete. Australia, WO. **PCT/AU2012/001**: 582.
- Pan, Z., C. Wu, J. Liu, W. Wang and J. Liu (2015). "Study on mechanical properties of cost-effective polyvinyl alcohol engineered cementitious composites (PVA-ECC)." Construction and Building Materials **78**: 397-404.
- Pathirage, C. P., D. G. Amaratunga and R. P. Haigh (2007). "Tacit knowledge and organisational performance: construction industry perspective." Journal of knowledge management **11**(1): 115-126.
- Pegna, J. (1997). "Exploratory investigation of solid freeform construction." Automation in construction **5**(5): 427-437.
- Peña-Álvarez, M., E. del Corro, Á. Morales-García, L. Kavan, M. Kalbac and O. Frank (2015). "Single layer molybdenum disulfide under direct out-of-plane compression: low-stress band-gap engineering." Nano letters **15**(5): 3139-3146.
- Perdew, J. P. (1992). "JP Perdew, JA Chevary, SH Vosko, KA Jackson, MR Pederson, DJ Singh, and C. Fiolhais, Phys. Rev. B 46, 6671 (1992)." Phys. rev. B **46**: 6671.
- Pu, J., Y. Yomogida, K.-K. Liu, L.-J. Li, Y. Iwasa and T. Takenobu (2012). "Highly flexible MoS2 thin-film transistors with ion gel dielectrics." Nano letters **12**(8): 4013-4017.

- Qiu, L., X. Yang, X. Gou, W. Yang, Z. F. Ma, G. G. Wallace and D. Li (2010). "Dispersing carbon nanotubes with graphene oxide in water and synergistic effects between graphene derivatives." Chemistry–A European Journal **16**(35): 10653-10658.
- Radisavljevic, B., A. Radenovic, J. Brivio, V. Giacometti and A. Kis (2011). "Single-layer MoS₂ transistors." Nature nanotechnology **6**(3): 147-150.
- Rael, R. and V. San Fratello (2011). "Developing Concrete Polymer Building Components for 3D Printing."
- Rafael Roldán, Andres Castellanos-Gomez, Emmanuele Cappelluti and F. Guinea (2015). "Strain engineering in semiconducting two-dimensional crystals." J. Phys.: Condens. **27**(313201).
- Robert, H. (2007). "Think formwork-reduced cost." Structure Magazine, April.
- Safe Work Australia. (2016). "Model work health and safety regulations." Retrieved 16/06, 2016, from <http://www.safeworkaustralia.gov.au/sites/swa/whs-information/construction/pages/construction>.
- Sanjayan, J. G., B. Nematollahi, M. Xia and T. Marchment (2018). "Effect of surface moisture on inter-layer strength of 3D printed concrete." Construction and Building Materials **172**: 468-475.
- Santos, P. M. D. and E. N. B. S. Júlio (2011). "Factors affecting bond between new and old concrete." ACI Materials Journal **108**(4): 449-456.
- Schneider, G. F., V. E. Calado, H. Zandbergen, L. M. Vandersypen and C. Dekker (2010). "Wedging transfer of nanostructures." Nano letters **10**(5): 1912-1916.
- Shi, Y., W. Zhou, A.-Y. Lu, W. Fang, Y.-H. Lee, A. L. Hsu, S. M. Kim, K. K. Kim, H. Y. Yang and L.-J. Li (2012). "van der Waals epitaxy of MoS₂ layers using graphene as growth templates." Nano letters **12**(6): 2784-2791.
- Splendiani, A., L. Sun, Y. Zhang, T. Li, J. Kim, C.-Y. Chim, G. Galli and F. Wang (2010). "Emerging photoluminescence in monolayer MoS₂." Nano letters **10**(4): 1271-1275.
- Swamy, R. N. (2002). Role and effectiveness of mineral admixtures in relation to alkali-silica reaction. The Alkali-Silica Reaction in Concrete, CRC Press: 112-137.
- Tam, C., V. W. Tam, J. K. Chan and W. C. Ng (2005). "Use of prefabrication to minimize construction waste-a case study approach." International Journal of Construction Management **5**(1): 91-101.
- Tao, L. and R. Shahsavari (2017). "Diffusive, displacive deformations and local phase transformation govern the mechanics of layered crystals: The case study of tobermorite." Scientific reports **7**(1): 5907.
- Taylor, H., C. Famy and K. Scrivener (2001). "Delayed ettringite formation." Cement and concrete research **31**(5): 683-693.
- Taylor, H. F. (1997). Cement chemistry, Thomas Telford.
- Thomas, M. (2011). "The effect of supplementary cementing materials on alkali-silica reaction: A review." Cement and Concrete Research **41**(12): 1224-1231.
- Topsakal, M. and S. Ciraci (2010). "Elastic and plastic deformation of graphene, silicene, and boron nitride honeycomb nanoribbons under uniaxial tension: A first-principles density-functional theory study." Physical Review B **81**(2): 024107.
- University of Southern California. (2014). "Contour crafting robotic construction system." Retrieved 07/06, 2016, from <http://www.contourcrafting.org/>.
- Van Der Zande, A. M., P. Y. Huang, D. A. Chenet, T. C. Berkelbach, Y. You, G.-H. Lee, T. F. Heinz, D. R. Reichman, D. A. Muller and J. C. Hone (2013). "Grains and grain boundaries in highly crystalline monolayer molybdenum disulphide." Nature materials **12**(6): 554.

- Vivian, H. (1951). "Studies in cement aggregate reaction. XVI. The effect of hydroxyl ions on the reaction of opal." Australia Journal of Applied Science **2**: 108-113.
- Wang, Y. (2015). "Y. Wang, C. Cong, W. Yang, J. Shang, N. Peimyoo, Y. Chen, J. Kang, J. Wang, W. Huang, and T. Yu, Nano Res. 8, 2562 (2015)." Nano Res. **8**: 2562.
- Wang, Y. and X. Hu (2016). "Benefits of short Kevlar fiber reinforcement at the interface for repair of concrete-like materials." Journal of Materials in Civil Engineering **28**(9): 04016087.
- Wei, Q., Y. Wang, W. Chai, Y. Zhang and X. Chen (2017). "Molecular dynamics simulation and experimental study of the bonding properties of polymer binders in 3D powder printed hydroxyapatite bioceramic bone scaffolds." Ceramics International **43**(16): 13702-13709.
- Williams, A. (2015). "Berkeley researchers pioneer new powder-based concrete 3D printing technique." Retrieved 6/06, 2016, from <http://www.gizmag.com/berkeley-researchers-pioneer-powder-based-concrete-3d-printing/36515/>.
- Wohlers, T. and T. Caffery (2012). Wohlers Report 2012: Additive Manufacturing and 3D Printing State of the Industry: Annual Worldwide Progress Report, Fort Collins: Wohlers Associates, Inc.
- Wohlers, T. and T. Caffery (2013). Wohlers Report 2013: Additive Manufacturing and 3D Printing State of the Industry: Annual Worldwide Progress Report, Fort Collins: Wohlers Associates, Inc.
- Wohlers, T. and T. Caffery (2015). Wohlers Report 2015: Additive Manufacturing and 3D Printing State of the Industry: Annual Worldwide Progress Report, Fort Collins: Wohlers Associates, Inc.
- Wolfs, R., F. Bos and T. Salet (2018). "Early age mechanical behaviour of 3D printed concrete: Numerical modelling and experimental testing." Cement and Concrete Research **106**: 103-116.
- Wong, F. and Y. Tang (2012). "Comparative embodied carbon analysis of the prefabrication elements compared with in-situ elements in residential building development of Hong Kong." World Academy of Science **62**(1): 161-166.
- Wong, K. V. and A. Hernandez (2012). "A review of additive manufacturing." ISRN Mechanical Engineering **2012**.
- Wong, R., J. Hao and C. M. Ho (2003). Prefabricated building construction systems adopted in Hong Kong. Proc. of the International Association for Housing Science on World Congress of Housing: Process and Product, Montreal, Canada.
- Wood, B. M. (2015). "5 Multifunctionality in Additive Manufacturing." Design and Manufacture of Plastic Components for Multifunctionality: Structural Composites, Injection Molding, and 3D Printing: 171.
- Wu, W., L. Wang, Y. Li, F. Zhang, L. Lin, S. Niu, D. Chenet, X. Zhang, Y. Hao and T. F. Heinz (2014). "Piezoelectricity of single-atomic-layer MoS₂ for energy conversion and piezotronics." Nature **514**(7523): 470.
- Xu, G., S. J. Chen, A. H. Korayem, W. H. Duan, J. G. Sanjayan and C. M. Wang (2016). 3D printing technology of concrete – an emerging construction method for industry. Concrete in Australia. **43**: 32-41.
- Yan, H., Q. Shen, L. C. Fan, Y. Wang and L. Zhang (2010). "Greenhouse gas emissions in building construction: A case study of One Peking in Hong Kong." Building and Environment **45**(4): 949-955.
- Yang, W. (2015). The issues and discussion of modern concrete science, Springer.
- Yue, Q., J. Kang, Z. Shao, X. Zhang, S. Chang, G. Wang, S. Qin and J. Li (2012). "Mechanical and electronic properties of monolayer MoS₂ under elastic strain." Physics Letters A **376**(12): 1166-1170.

- Zhan, Y., Z. Liu, S. Najmaei, P. M. Ajayan and J. Lou (2011). "Large area vapor phase growth and characterization of MoS₂ atomic layers on SiO₂ substrate." arXiv preprint arXiv:1111.5072.
- Zhang, Q., Z. Chang, G. Xu, Z. Wang, Y. Zhang, Z. Q. Xu, S. Chen, Q. Bao, J. Z. Liu and Y. W. Mai (2016). "Strain relaxation of monolayer WS₂ on plastic substrate." Advanced Functional Materials **26**(47): 8707-8714.
- Zhao, Z., H. Zhang, H. Yuan, S. Wang, Y. Lin, Q. Zeng, G. Xu, Z. Liu, G. Solanki and K. Patel (2015). "Pressure induced metallization with absence of structural transition in layered molybdenum diselenide." Nature communications **6**: 7312.
- Zheng, C., Z.-Q. Xu, Q. Zhang, M. T. Edmonds, K. Watanabe, T. Taniguchi, Q. Bao and M. S. Fuhrer (2015). "Profound effect of substrate hydroxylation and hydration on electronic and optical properties of monolayer MoS₂." Nano letters **15**(5): 3096-3102.
- Zhu, B., X. Chen and X. Cui (2015). "Exciton binding energy of monolayer WS₂." Scientific reports **5**: 9218.
- Zhu, C., G. Wang, B. Liu, X. Marie, X. Qiao, X. Zhang, X. Wu, H. Fan, P. Tan and T. Amand (2013). "Strain tuning of optical emission energy and polarization in monolayer and bilayer MoS₂." Physical Review B **88**(12): 121301.
- Zhu, H., Y. Wang, J. Xiao, M. Liu, S. Xiong, Z. J. Wong, Z. Ye, Y. Ye, X. Yin and X. Zhang (2015). "Observation of piezoelectricity in free-standing monolayer MoS₂." Nature nanotechnology **10**(2): 151.